Coulomb Drag, Mesoscopic Physics, and Electron-Electron Interaction.

Submitted by Adam S. Price to the University of Exeter as a thesis for the degree of Doctor of Philosophy in Physics
October, 2008

I certify that all material in this thesis which is not my own work has been identified and that no material has previously been submitted and approved for the award of a degree by this or any other University.

A. S. Price
October, 2008

Abstract

The first part of this thesis deals with the study of mesoscopic fluctuations of the Coulomb drag resistance in double-layer GaAs/AlGaAs heterostructures, both in weak magnetic fields and strong magnetic fields. In the second part, measurements are made in a monolayer graphene structure, specifically of the quantum lifetime, and the mesoscopic resistance fluctuations at quantising magnetic fields.

In weak fields, we perform the first measurements of the fluctuations of the drag as a function of changing concentration and magnetic field. The amplitude of the fluctuations was seen to exceed the size of the average drag at low temperatures, resulting in random but reproducible changes in the sign of the drag with varying concentration and magnetic field. The variance and correlation magnetic field were studied as a function of temperature. Comparison was made to existing theories for drag fluctuations in the diffusive regime of the drag (where the electron mean free path is much smaller than the separation between layers). We observe a large enhancement of the magnitude of the fluctuations of four orders of magnitude compared to the theoretical expectation, as well as a different temperature dependence. Our results prompted further theoretical studies, extending the understanding of drag fluctuations into the ballistic regime, where the local properties of the layers become important. We compare our results to this theory and find good agreement.

We extend these measurements to the regime of strong magnetic fields where transport involves composite-fermion quasiparticles. We study the temperature dependence of the amplitude and correlation magnetic field of the fluctuations, and analyse our results using existing theoretical models for drag fluctuations in the diffusive regime of drag.

Much controversy exists over the dominant scattering mechanisms in graphene. We use measurements of the concentration and temperature dependence of the quantum lifetime and transport time in graphene to identify the dominant electron scattering mechanisms. We then perform measurements of resistance fluctuations in the integer quantum Hall effect regime of magnetic fields, and show our results to be well described by existing models developed for conventional 2D systems. Using these models we make estimates for the properties of the disorder in graphene.

Acknowledgements

My thanks must first of all go to my supervisor, Alex Savchenko. His interest and enthusiasm for the work described in this thesis has been a continual and important source of motivation throughout my project.

I would also like to thank Dave Horsell, who has been the post-doc in our research group for the entirety of my PhD study. He has always been willing to discuss any topic in physics, and his expertise has often been of great value. Thanks must also go to Sasha Mayorov, with whom I have had many useful discussions. My next thanks go to two former members of our group – Evgeniy Galaktionov and Andrei Kretinin, both of whom spared much time in helping me learn the experimental techniques that I relied on throughout the course of my project. Thanks also to Roman Gorbachev, Fedor Tikhonenko, both of whom were always willing to provide an extra hand when needed. Additionally, thanks to our two new students Alexei and Aleksey, who spent some of their first days in our lab with some data analysis whilst I was busy with putting the finishing touches on this thesis.

Last, but by no means least, I must thank Paul Wilkins, our lab technician, whom helped with countless mechanical difficulties as well as helped me move house on a number of occasions. Also, Dave Manning and Adam Woodgate, both of whom played the critical role of providing cryogens for our experiments, as well as maintaining much of the cryogenic equipment.

And of course, I appreciate the emotional support from my mother, Mary, brother and sister, Ben and Nichola, and friends during the last four years of study.

Contents

List of Figures

List of Tables

Symbols and Abbreviations Used

ACF : autocorrelation function

CF : composite fermion

D : diffusion coefficient

DOS : density of states

e-e : electron-electron

E_{Th} : Thoules energy

g : dimensionless conductance, $\sigma/(e^2/h)$

$\varrho(E)$: The density of states

g_s : The spin degeneracy, taking values of 1 or 2

g_v : The valley degeneracy, taking values of 1 or 2

l : elastic mean free path

L : distance between voltage probes; equivalently, the sample size

LL : Landau level

L_φ : coherence length

L_T : thermal length

μ : mobility

n : carrier concentration

ν : Landau-level filling factor

PSD : power spectral density

ρ_D : drag resistivity

SdH : Shubnikov-de Haas

T : temperature

τ : momentum relaxation time.

τ_q : quantum lifetime.

τ_φ : coherence time

UCF : universal conductance fluctuations

ω_c : cyclotron frequency

W : sample width

List of publications

Publications

- A. S. Price, A. K. Savchenko, B. N. Narozhny, G. Allison, D. A. Ritchie, Giant Fluctuations of Coulomb Drag in a Bilayer System, *Science* **316**, 99-102 (2007).

- A. S. Price, A. K. Savchenko, G. Allison, B. N. Narozhny, Giant Fluctuations of Coulomb Drag, *Physica E: Low-dimensional Systems and Nanostructures* **40**, 961-966 (2008).

Conference presentations

- A. S. Price, A. K. Savchenko, B. N. Narozhny, G. Allison, D. A. Ritchie, Giant Fluctuations of Coulomb Drag in a Bilayer System, *Condensed Matter and Material Physics (CMMP 2007)* (Poster presentation).

- A. S. Price, A. K. Savchenko, G. Allison, B. N. Narozhny, Giant Fluctuations of Coulomb Drag, *International Conference on Electronic Properties of Two-dimensional Systems (EP2DS 17)* July, 2008 (Invited talk).

Introduction

As a result of improvements in the fabrication techniques, it has become possible to make bilayer semiconductor heterostructures in which parallel conducting layers are separated by just a few hundred Angstroms. This has made it possible to perform measurements of the so-called Coulomb drag resistance. This resistance relates a current in one layer to an induced voltage in the other layer, despite the absence of electrical connection between the two layers. This effect originates from the inter-layer Coulomb interaction between electrons, and it has become an important tool for direct studies of the electron-electron interaction. In this thesis we extend the measurement of Coulomb drag into the mesoscopic regime, to study an interesting interplay between disorder and electron-electron e-e interaction.

Electron-electron interaction is an area of great interest in contemporary condensed matter physics, and plays an important role in many phenomena. These include the metal-to-insulator transition in 2D systems and the fractional quantum Hall effect, where interactions between electrons in the presence of strong magnetic fields cause the strongly interacting electron liquid to "condense" into a gas of weakly interacting composite-fermion quasiparticles.

Another consequence of the improvements in semiconductor fabrication is the decreasing size of devices. At low temperatures, electrons can travel diffusively through a sample whilst maintaining a coherent phase. Under these conditions, quantum interference occurs between different electron trajectories, resulting in a variety of effects, such as weak localisation, universal conductance fluctuations, and the Aharonov-Bohm oscillations. Such quantum effects are of importance both to our understanding of fundamental physics, and possible utilisation in devices. The measurement of mesoscopic effects reveals information about e-e interaction, which is the dominant dephasing mechanism at low temperatures where electron-phonon scattering is less significant.

An important tool in investigating the transport properties of materials is the use of magnetic fields. In the presence of strong magnetic fields the properties of samples is drastically altered, resulting in fascinating physics, such as the integer and fraction quantum Hall effects. The composite fermions in the fractional quantum Hall effect display many of the same properties as electrons in weak magnetic fields, including

Coulomb drag and mesoscopic conductance fluctuations. In this thesis we perform the first study of the mesoscopic Coulomb drag between composite fermions.

Finally, a new material has become the centre of much attention in the condensed matter physics community. Recently, graphene structures have successfully been fabricated: these atomic monolayers of graphite display many unique properties caused by the fact that electrons behave as massless particles with a linear dispersion relation without an energy band-gap. There is great interest not only in the fundamental physics of graphene, but also its promise for future device application. An important step in achieving workable graphene devices will be understanding what the dominant sources of electron scattering are in graphene structures. We perform measurements of the quantum lifetime in graphene to help elucidate the electron scattering mechanisms. These results are supplemented by investigations of the mesoscopic fluctuations of the resistance at high magnetic fields, which are compared with those for conventional 2D systems.

The First Chapter of this thesis describes some of the basic physics of electron conduction that will be referred to throughout the chapters in this thesis. This is followed by a review of the existing theoretical and supporting experimental work that has been done on Coulomb drag, with particular emphasis on those areas relevant to the work in this project. Some experimental details are then given, describing the measurement techniques and equipment used in this project, as well as details of the double-layer samples used in Coulomb-drag measurements. The first chapter is concluded with a discussion of our drag measurements, and how spurious signals are identified. Some basic measurements of the drag are performed to reproduce the experimental work reported previously by other groups.

The Second Chapter describes the measurement of mesoscopic fluctuations of the Coulomb drag resistance in weak magnetic fields. The background physics describing coherent transport and universal conductance fluctuations is given, along with the theoretical predictions for universal conductance fluctuations of the drag. Our measurements of the drag resistance fluctuations are then discussed, and the results are compared with new theoretical work performed in response to our observations.

The Third Chapter reports the behaviour of drag resistance fluctuations between composite fermions. A brief review of the fractional quantum Hall effect and composite fermion physics is given, as well as a review of theoretical and experimental

work done to date on Coulomb drag in composite fermion systems. We then report our observations of the composite fermion drag resistance fluctuations, and their behaviour with changing temperature. Comparison of experimental results to existing theoretical models is then made.

The Fourth Chapter deals with our measurements performed in a graphene monolayer system. The unusual physics of graphene monolayers is reviewed, which is then followed by a description of theoretical models developed for conventional 2D systems that deal with mesoscopic fluctuations in the presence of quantising magnetic fields. We then report our findings for the concentration and temperature dependence of the quantum lifetime τ_q, and draw conclusion from these results upon the dominant scattering mechanisms in graphene. We then present our observation of resistance fluctuations in different regions of a Landau level, and interpret our findings in terms of the theoretical models for conventional 2D systems.

This thesis is then concluded with a summary of our findings, as well as suggestions for extensions to the work performed in this project.

Chapter 1

Coulomb Drag

In this chapter some of the important background physics dealt with in later chapters is described. This includes the different scattering times used in describing electron transport: the momentum relaxation time and quantum lifetime. Then the effect of magnetic field on electron conduction is discussed, such as the Shubnikov-de Haas and quantum Hall effects.

Then, an outline of the Coulomb drag resistance in semiconductors is given, including the relevant theoretical and experimental background of the field. This is followed by a description of the double-layer samples used in measuring the drag resistance, and the measurement techniques and apparatus used. Finally, basic measurements of the drag resistance are discussed, reproducing the key observations of other groups that confirm many of the predictions made by existing theoretical models.

1.1 Scattering times

In describing the transport of free electrons in metals the concept of a momentum relaxation time τ_p is used. This is the average time during which an electron can travel without being scattered on a large $\theta \sim 90^\circ$ angle: such large-angle scattering events contribute strongly to the momentum relaxation rate. Thus, τ_p is related to the probability of scattering $P(\theta)$, weighted by the scattering angle θ [1]:

$$\tau_p = \int P(\theta)(1 - \cos\theta) d\Omega., \tag{1.1}$$

where $d\Omega = \sin\theta d\theta d\phi$ is the solid angle.

The time between scattering events, regardless of scattering angle, is represented by the quantum lifetime τ_q, which is defined as

$$\tau_q = \int P(\theta) d\Omega. \tag{1.2}$$

For the case of short-range scatterers these two scattering times are equal as any scattering is essentially large-angle scattering. However, in the case of long-range scatterers where the disorder potential varies slowly on the scale of the electron wavelength, τ_p can be much larger than τ_q. This is due to electrons undergoing many small-angle scattering events before the electron significantly changes its momentum. Thus, measurements of the ratio of τ_p/τ_q are a useful method for elucidating the extent to which scattering is short- or long-range.

1.2 Shubnikov-de Haas effect

In the presence of a sufficiently strong magnetic field perpendicular to the 2DEG the density of states develops discrete behaviour, resulting in oscillations of the resistivity as a function of either magnetic field or chemical potential. This results from the free electrons experiencing a Lorentz force in magnetic field that causes a circular trajectory of the electrons between scattering events. When $\omega_c\tau = eB\tau_q/m^* > 1$ the electrons complete full orbits resulting in the formation of Landau levels and a density of electron states (DOS) composed of a series of delta-functions. This 0D-DOS is broadened in the presence of disorder, as illustrated in Fig. 1.1.

Electron transport in B-fields was studied theoretically by Isihara *et al.* [2]. The longitudinal and Hall resistivities are

$$\begin{aligned} \rho_{xx} &= \tfrac{1}{\sigma_0}\left(1 + 2\tfrac{\Delta\varrho}{\varrho_0}\right), \quad \text{and} \\ \rho_{xy} &= \tfrac{\omega_c\tau_0}{\sigma_0}\left(1 - \tfrac{1}{(\omega_c\tau_0)^2}\tfrac{\Delta\varrho}{\varrho_0}\right), \end{aligned} \tag{1.3}$$

where $\sigma_0 = e^2 n_0 \tau_0/m^*$ is the zero-field conductivity with n_0 and τ_0 the zero-field concentration and momentum relaxation time, $\Delta\varrho$ is the oscillating part of the density of states, which is small compared to the zero-field density of states ϱ_0 and is controlled by τ_q.

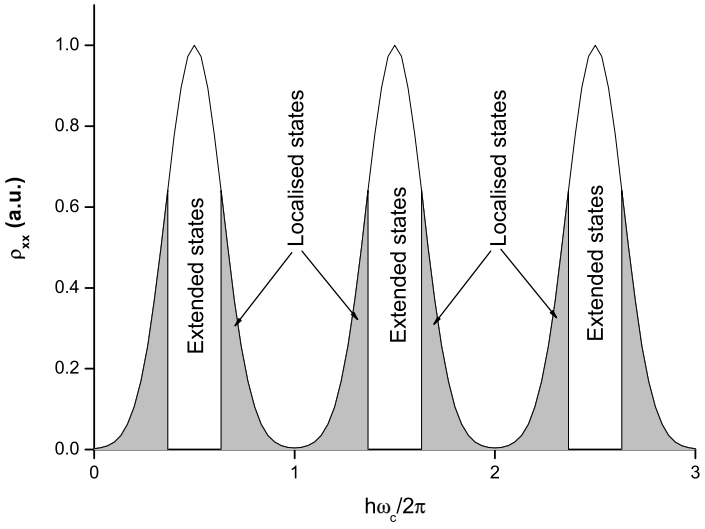

Figure 1.1: The 0D DOS of a 2DEG system in the presence of a strong B-field where the LLs have been broadened by scattering. Near the centre of LLs the states are extended, whilst near the tails of the LLs the states are localised.

In [2] a short-range scattering potential was assumed, whereas it was pointed out by Coleridge *et al.* [3] that using a more realistic long-range scattering potential introduces an important modification in that two different scattering times must be considered. These are the large-angle scattering time τ_p and the quantum lifetime τ_q.

Isihara showed the oscillating part of the density of states to go as

$$\frac{\Delta\varrho}{\varrho_0} = 2\sum_{s=1}^{\infty} \exp(-\pi s/\omega_c\tau_q)\cos\left(\frac{2\pi s E_F}{\hbar\omega_c} - s\pi\right), \tag{1.4}$$

where the sum over s is a sum over the different harmonics. The above expression is correct for zero temperature, but for finite temperatures an extra factor $D(sX)$ must be included [2], where

$$D(sX) = \frac{sX}{\sinh(sX)}, \tag{1.5}$$

where $X = 2\pi^2 k_B T/\hbar\omega_c$. Note that in the low-temperature limit of $k_B T \ll \hbar\omega_c$ the temperature factor can be neglected as $D(sX) \approx 1$.

Substituting equations 1.4 and 1.5 into equation 1.3 we find

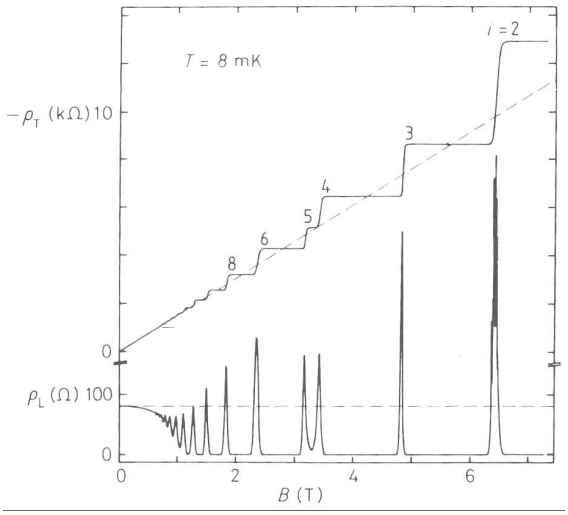

Figure 1.2: Measurements performed by von Klitzing of ρ_{xx} and ρ_{xy} as a function of B for a $GaAs - Al_{0.3}Ga_{0.7}As$ heterojunction with concentration $n = 3.7 \times 10^{11}\text{cm}^{-2}$ demonstrating the key features of the IQHE [5].

$$\frac{\Delta\rho_{xx}}{\rho_0} = 4\exp\left(-\frac{\pi}{\omega_c\tau_q}\right)\frac{2\pi^2 k_B T/\hbar\omega_c}{\sinh(2\pi^2 k_B T/\hbar\omega_c)}\cos\left(\frac{2\pi E_F}{\hbar\omega_c} - \pi\right). \tag{1.6}$$

1.2.1 The Integer Quantum Hall Effect

The integer quantum Hall effect (IQHE) was first observed by von Klitzing *et al* in 1980 [4]. The IQHE is seen at low temperatures ($k_B T < \hbar\omega_c$) in high-mobility samples in the presence of magnetic fields perpendicular to the plane of the 2DEG ($\omega_c\tau_q > 1$, where τ_q is the quantum lifetime). Under these conditions plateaux are seen in the Hall resistivity ρ_{xy} that coincide with zeros in the longitudinal resistivity ρ_{xx}, as demonstrated in Fig. 1.2. The centres of the plateaux in ρ_{xy} and zeros in ρ_{xx} occur at integer values of ν (ν is the number of occupied LLs with one spin), and the plateaux in ρ_{xy} take quantised values of $h/\nu e^2$, with $\nu = 1,2,3\ldots$.

As the magnetic field is increased the broadening of the Landau levels by disorder becomes less than the energy separation between LLs. Below this transition the oscillations due to the formation of LLs are seen as a small correction to ρ_{xx} and are described by the SdH effect. The transition occurs when $\hbar/\tau_q$, the broadening of the LL energies due to disorder, becomes less than the energy separation between LLs, $\hbar\omega_c$.

The degeneracy of each Landau level is $N = eB/h$, and is the same for each LL. The energy of the i^{th} LL is $E_i = \hbar\omega_c(i + 1/2)$, with $i = 0,1,2\ldots$. Thus, the filling factor ν, is given by

$$\nu = \frac{n}{N} = \frac{nh}{eB}. \tag{1.7}$$

1.3 Coulomb Drag

When two parallel conducting layers are in sufficiently close proximity, the transport properties of each layer are modified due to electron-electron (e-e) interactions. This interaction between electrons is an inter-layer effect, with electrons in the top layer influencing the motion of electrons in the bottom layer.

One of the effects of this inter-layer coupling is the occurrence of a "drag" current or voltage. This is the effect whereby a driving current in one layer, the "active" layer, results in a current being created in the other, "passive", layer: the drag current being in the same direction as the driving current. The momentum transfer occurs in scattering events between fluctuations in the electron density of each layer: perfectly uniform electron distributions would result in no drag current. Thus, the drag current is a probe of intra-layer density excitations and inter-layer electron-electron interactions.

Interactions between electrons are an area of great interest both theoretically and experimentally. Electron-electron interactions are responsible for a variety of fascinating effects and exotic states of matter. Examples include the fractional Quantum Hall effect, the Mott transition, high-temperature superconductivity, Wigner crystallisation, and Coulomb gaps in disordered systems. Recently, interest was revived by the observation of a 2D metallic state in a high-mobility low-density 2D system [6]. These systems are characterised by large Coulomb interaction energy compared with the Fermi energy of carriers.

However, direct measurement of e-e scattering is difficult in single layer structures, and is usually measured indirectly. Examples include measuring the electron coherence time, τ_ϕ, via measurement of weak localisation effects in the diffusive regime [7], interference effects on μm length scales in the ballistic regime [8], and by comparison of the thermal and electrical conductivities in metals [9]. Frictional drag experiments provide a method where e-e interactions can be measured directly, and so present a valuable tool in investigating Coulomb interaction effects in transport. The idea of measuring Coulomb drag in double layer systems was first put forward and developed by Pogrebinski [10] and Price [11]. The system they proposed consisted of two parallel conducting semiconductor layers, separated by a thin electrically insulating layer. If the separation between layers was of the order of the

electron-electron separation, then the Coulomb interaction between electrons would result in momentum transfer between the layers. This meant that when a current was driven in the active layer, then momentum would be transferred into the passive layer. This resulted in either a drag current, in a closed circuit configuration (i.e., where current is allowed to flow in the passive layer), or a drag voltage in the case of an open circuit in the passive layer. The measured drag voltage, V_D, can be related to the driving current in the active layer, I_A, in the following way:

$$V_D = -\rho_D I_A \frac{L}{W}, \tag{1.8}$$

where L and W are the sample length and width, respectively, and ρ_D is the drag resistivity. The negative sign is due to the fact that the 'dragged' current is in the same direction as the driving current and the induced drag voltage opposes the drag current. Similar to the single layer expressions which relate the resistivity to the microscopic properties of the system, the interlayer momentum relaxation rate, τ_D, can be defined [12] as

$$\rho_D = \frac{m}{n_1 e^2 \tau_D}. \tag{1.9}$$

Here n_1 is the electron concentration in the active layer, and m^* is the electron effective mass. It was some years before these predictions could be tested, as the required fabrication technology was not in place. The first observation of the drag effect was reported in 1989 by Solomon *et al.* [13], who measured electron coupling between 2D and 3D layers. There was some uncertainty in the results, however, due to an unanticipated thermoelectric effect. This resulted in a change in sign of the transconductance, due to an energy transfer between layers via the Peltier effect.

Further supporting evidence of the observation of the Coulomb drag effect came with measurements on coupled 2D layers. Gramila *et al.* reported measurements of drag between electrons between two 2D layers for the first time in 1991 [14], whilst Sivan *et al.* investigated the coupling between electrons and holes [15].

Gramila *et al.* found that the magnitude, sign, temperature and barrier thickness dependence of the observed drag to be in reasonable agreement with Coulomb drag theory [14]. Using Boltzmann transport theory, they calculated the temperature dependence of τ_D to be

$$\tau_D^{-1} = \frac{\zeta(3)\pi(k_B T)^2}{16\hbar E_F (q_{TF} d)^2 (k_F d)^2}, \tag{1.10}$$

where d is the centre-to-centre distance between 2DEGs, $\zeta(3) = 1.202\ldots$ is the Riemann zeta function, T is the temperature, E_F the Fermi energy, q_{TF} is the Thomas-Fermi screening wave vector (0.2 nm^{-1} in GaAs), and k_F the Fermi wave vector. This can be rearranged [16] in terms of the carrier concentration:

$$\tau_D^{-1} = \frac{\zeta(3) m \pi^2}{4h^3 q_{TF}^2} \frac{1}{d^4} \frac{1}{n_2^{3/2} n_1^{1/2}} (k_B T)^2, \tag{1.11}$$

where n_2 and n_1 are the carrier concentration of the active and passive layers, respectively. Thus combining 1.9 and 1.11, and assuming matched carrier densities in the two layers ($n_1 = n_2$) we arrive at the following expression for the drag resistivity:

$$\rho_D = \frac{\zeta(3) m^2 \pi^2}{4h^3 e^2 q_{TF}^2} \frac{1}{d^4} \frac{1}{n^3} (k_B T)^2. \tag{1.12}$$

Juaho and Smith [12] later derived this result using a more physically transparent method (the actual expression given in [14] is half this value, which was later corrected in [12]). Starting with a linearised Boltzmann equation, the interlayer scattering rate is found by performing the integration

$$\tau_D^{-1} = \frac{\hbar^2}{2\pi^2 n_1 m k_B T} \int dq \int d\omega q^3 |e\phi(q)|^2 [\mathrm{Im}\chi(q,\omega)]^2 \frac{1}{\sinh^2(\hbar\omega / k_B T)}. \tag{1.13}$$

This equation effectively sums the product of three physical terms over all the values of energy and momentum transfer possible. The first factor in the integrand is the Fourier component of the screened Coulomb interaction between the layers:

$$e\phi(q) = \frac{2\pi e^2}{\kappa} \frac{q}{2q_{TF}^2 \sinh qd + (2qq_{TF} + q^2)\exp(qd)}. \tag{1.14}$$

Here κ is the dielectric constant. The exponential term limits the integral to low wave vectors, $q < 1/d$.

The drag also depends on the ability of the layers to emit and absorb fluctuations in the electron distribution. The electron susceptibility, also called the electron response function χ, relates the induced charge distribution to an external electric

field, and so the imaginary component which appears in Eq. 1.13 describes the tendency for fluctuations to form in the layers. This factor appears squared, as it is included for each layer (assumed in this case to be identical). The requirement that these fluctuations are long-lived places an upper cut-off frequency on the integral. Note that this dependence of drag on a non-uniform electron distribution finds an analogy in mechanical friction occurring between rough, uneven surfaces.

The last $\sinh^2(\hbar\omega/k_BT)$ factor describes the available phase space for electrons to be scattered into, which in turn is dependent on the broadening of the Fermi distribution function in each layer. This phase space restriction results in a T^2 dependence of the Coulomb drag, as each Fermi distribution is broadened by the thermal energy, k_BT.

1.3.1 Phonon Drag

Whilst for small layer separations the agreement with Coulomb drag theory was fairly good [14], at larger separations there was a clear deviation from a constant temperature dependence of the scaled drag resistivity, ρ_D/T^2, which occurred around a temperature of 2 K. This deviation from the expected temperature dependence spurred further theoretical work on possible explanations. The form of the temperature dependence is similar to that of the acoustic-phonon-limited scattering rate, τ_ϕ^{-1} , in single layer structures, and it was suggested that the observed deviation was due to a contribution to drag effect that was mediated by phonons [16].

In order to observe phonon drag effects, the layer spacing must sufficiently large that [17]

$$d \geq \sqrt{\frac{k_BT_{BG}}{E_Fq_{TF}k_FC_{DP}}\left(\frac{v_F}{c_l}\right)^{1/4}}. \tag{1.15}$$

Here $T_{BG} = 2\hbar c_l k_F/k_B$ is the Bloch-Gruneisen temperature, c_l is the speed of the longitudinal phonons in GaAs and C_{DP} is the deformation-potential coupling constant. For GaAs, this gives a value of d of a few tens of nanometers, for typical experimental concentrations [17].

Also, at large interlayer separations, the calculated Coulomb drag was too small to account for that observed: the measured drag had some long-range component. It was suggested by Tso *et al.* [18] that virtual phonons were also involved. Fur-

thermore, this virtual phonon contribution to drag was predicted to have a weak dependence on interlayer separation.

Experiments by Gramila *et al.* [16] and Rubel *et al.* [19] supported this. Gramila *et al.* made measurements on samples with separations of 175, 225, 500 and 5000 Å. By subtracting the calculated Coulomb contribution, the phonon contribution to drag could be compared for different separations, as shown in Fig. 1.3. Once the Coulomb part is removed, a long range contribution remains, which is very weakly dependent upon interlayer separation, in contrast to the strong d^{-4} dependence of Coulomb drag.

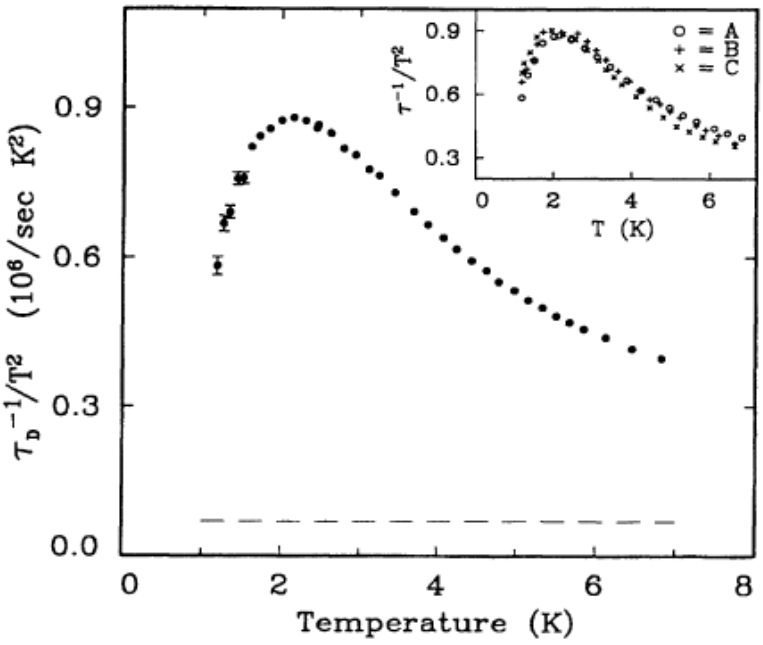

Figure 1.3: The temperature dependence of the scaled frictional drag scattering rate τ_D^{-1}/T^2 for a sample with a 500 $\mathring{A}$ thick barrier. The dashed line is the expected drag scattering rate, calculated using Eq. 1.11. Inset: the same dependence plotted for several samples with different barrier thickness (500, 225, 175) after the calculated Coulomb drag using Eq. 1.11 has been subtracted. Taken from [16].

Furthermore, the expected phonon drag due to real phonons was too small to account for the observed magnitude of the drag by a factor of 27 [16]. This was taken as supporting evidence for a virtual phonon mediated drag mechanism. The drag measured samples with a very large barrier ($d = 5000\,\text{Å}$) was about an order of magnitude smaller than that in their 500 Å sample, despite the real-phonon mean free path being much larger than the layer separation, of the order of 1 mm. This also indicates a significant role of virtual phonons, which, being virtual particles,

have a shorter lifetime, and thus shorter mean free path than real phonons.

In [19] a maximum in the drag resistance was observed when the electron densities in the two layers were equal. This supported the theoretical predictions that, due to phase space considerations, phonon mediated drag was enhanced for matched layer densities [17, 18]. It was shown that phonon emission and absorption was strongest for back-scattered electrons, where the mediating phonon has a wave vector $q = 2k_F$. To satisfy conservation of momentum, this occurs most frequently when k_F is the same in both layers, and thus both layers have equal carrier concentrations.

The temperature dependence of phonon mediated drag is due to the phase space restrictions on phonon momentum. At low temperatures thermal excitations are only sufficiently energetic to excite phonons with momentum $q < 2k_F$. As the temperature increases, higher momentum phonons are excited, and so more of the electron phase space is available for scattering, leading to a strong T dependence at higher temperatures. This continues up to a temperature where phonons with $q \sim 2k_F$ are excited. Past this point, phonons with $q > 2k_F$ can not participate in scattering, as electron momentum can not be conserved within the available phase space. This leads to a weaker T dependence of phonon drag at high T. In combination with this is the fact that the available phase space for large angle scattering, corresponding to $q = 2k_F$, diverges as $T \to 0$ [20]. This allows $2k_F$ phonons to dominate scattering, even at temperatures below those required for significant excitation of such phonons.

1.3.2 Plasmon enhancement of the drag

In [21] it was shown that at moderately high temperatures ($T \geq 0.2T_F$, where $T_F = E_F/k_B$ is the Fermi temperature) an enhancement of the drag resistance occurs due to the presence of coupled plasmon modes in double-layer systems. This plasmon enhancement of the drag is significant for temperatures above $0.2T_F$, resulting in a peak at $T \approx 0.5T_F$. This predicted enhancement has been experimentally confirmed in [22], and their observations are illustrated in Fig. 1.4.

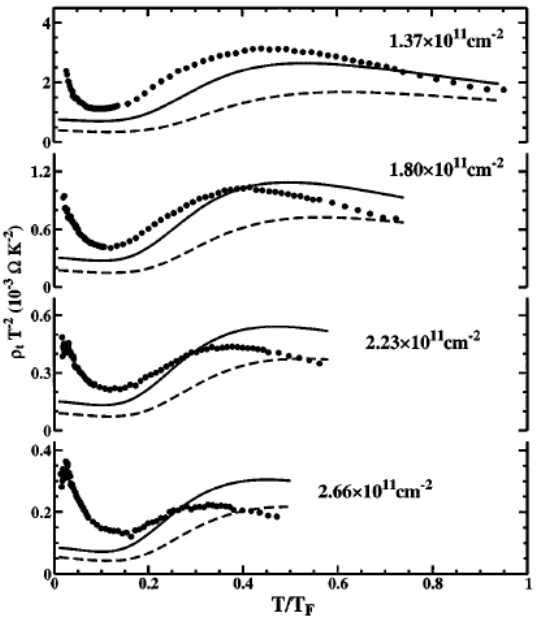

Figure 1.4: The scaled drag resistivity $\rho_t T^{-2}$ as a function of the reduced temperature T/T_F for several different matched carrier densities: $n = 1.37$, 1.80, 2.23, and 2.66 $\times 10^{11}\,\mathrm{cm}^{-2}$. The dashed (solid) lines are the random phase approximation (Hubbard) calculations. Taken from [22].

1.3.3 Drag In Disordered Systems

Drag in disordered systems was first studied by Zheng and MacDonald [23]. They derived an expression for the interlayer scattering rate, τ_D^{-1}, in a diffusive system:

$$\tau_D^{-1} = -\frac{\pi(k_B T)^2}{12\hbar E_F (q_{TF} d)^2 (k_F l)^2} \ln\left(\frac{T}{T_\tau}\right). \tag{1.16}$$

Here l is the mean free path and $T_\tau = \hbar/k_B\tau$. This expression applies to a system where $l \ll d$, and $T \ll T_F$, and $k_F d \gg 1$. The weaker dependence on layer spacing d is a result of the imaginary component of the electron response function $\mathrm{Im}\chi$ being different in ballistic and diffusive systems. Ballistic and diffusive refer to the size of the electron mean free path to the inter-layer distance: the ballistic regime of drag refers to systems where $l \gg d$, whilst in the diffusive regime $l \ll d$. Disorder in a system is seen to enhance the drag, due to the enhancement of $\mathrm{Im}\chi$, which determines the size of density fluctuations in the layers.

This enhanced drag, with an altered temperature and layer separation dependence, is only observable in low-mobility samples, or at very low temperatures. Figure 1.5 shows how the relative correction to the interlayer scattering rate τ_B/τ_Δ increases with decreasing mobility. The notation used here is from [23] where τ_B is the ballistic Coulomb drag, and τ_Δ is the correction to this interlayer scattering due to disorder. In the high-mobility samples used so far to investigate drag, such disorder effects would not be observable at experimentally attainable temperatures [23].

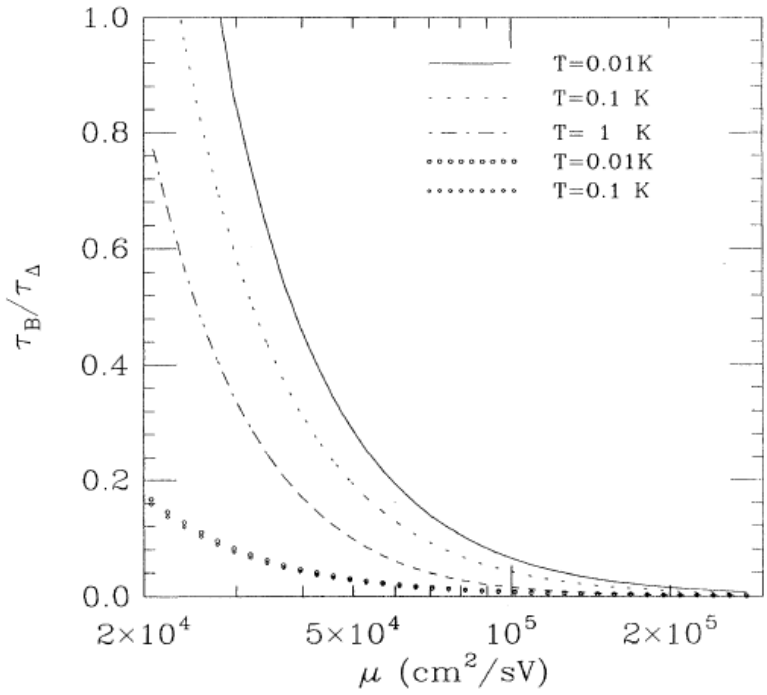

Figure 1.5: Relative correction to the interlayer scattering rate τ_B/τ_Δ as a function of sample mobility for several different temperatures. Taken from [23].

For the case $d \ll l$, Eq. 1.16 describes the contribution to the frictional drag scattering rate of momentum transfers with wave vector $q < l^{-1}$. In the range $l^{-1} < q < d^{-1}$, the contribution is described by Eq. 1.11. However, even in this ballistic regime of the drag, when $d \ll l$, disorder can still dominate the drag at sufficiently low temperatures. The crossover temperature [23] where the effect of disorder on drag can be observed is

$$T_c \sim T_\tau \exp[-3(l/d)^2/4\zeta(3)]. \tag{1.17}$$

1.4 Drag at low electron densities

Interesting work has been done on the behaviour of the drag resistivity when the electron concentrations becomes sufficiently low so that the system undergoes a metal to insulator transition (MIT). Shimsoni [24] considers the behaviour of the drag resistivity in the Anderson insulating state, whilst Apalkov and Raikh [20] analyse the behaviour of the drag at the MIT. Such regimes are beyond the scope of this project, although some recent low-density measurements do have relevance

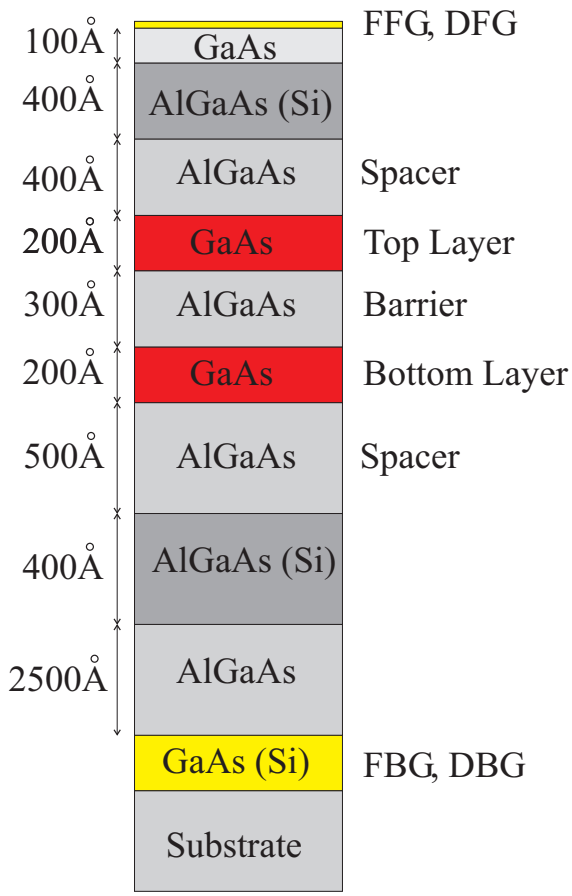

Figure 1.6: Schematic of wafer used in double-layer samples. The 2DEG are formed in the two 200 Å thick GaAs layers. FFG, DFG, FBG, DBG are the full front and defining front gates, full back and defining back gates, respectively. All AlGaAs layers are actually $Al_{0.33}Ga_{0.67}As$. Adapted from [27].

to our measurements, where a stronger than $n^{-1.5}$ dependence of the drag was observed [25]. Other groups have observed a similar increased carrier concentration dependence of the drag resistivity in low density double-layer hole samples [26].

1.5 Samples and Techniques

Measurements of the drag resistivity in this project were made on high-mobility modulation doped GaAs-AlGaAs heterostructures. These heterostructures comprised of two conducting GaAs layers separated by a thin AlGaAs barrier layer, which were epitaxially grown using MBE techniques. A schematic of the wafer profile of the samples is shown in Fig. 1.6. The two 2DEGs are formed in the 200 Å thick GaAs layers. The GaAs layers are separated by a 300 Å thick layer of AlGaAs, such that the interlayer separation is 500 Å. The electron concentration of the upper layer is controlled by a metallic gate deposited on the top of the wafer, whilst the concentration of the lower layer is controlled by a back gate formed by a Si-doped (the doping concentration is $10^{18}\,\mathrm{cm}^{-3}$) GaAs layer. The two conducting layers must be electrically isolated from each other, i.e. the two layers are "defined", and this is

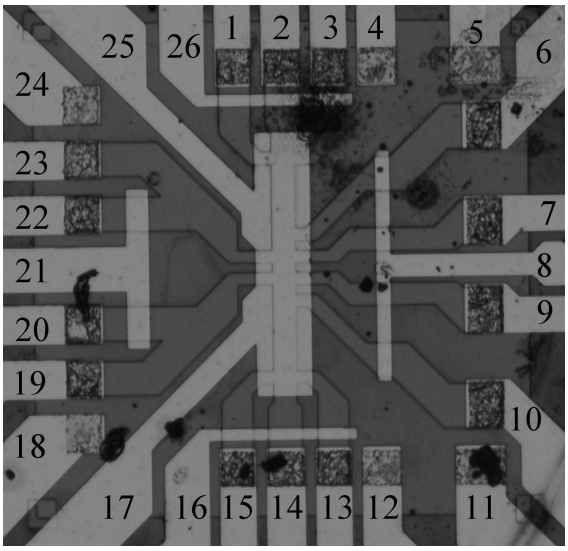

Figure 1.7: Optical image of sample NA06. Contacts 8, 16, 21 and 26 are front defining gates; 4, 11, 12, 18 and 24 are back defining gates; 25/17 is the full front gate, 5 is the full back gate, whilst the other contacts are ohmic contacts to the Hall bar. Whether a contact is connected to the upper or lower layer is dependent upon which of the defining gates is charged.

done using defining gates. The full back gate (for controlling the concentration in the lower layer) and the defining back gates (for breaking certain connections from the top of the structure to the lower layer, which is necessary to define the sample) are patterned in the doped GaAs layer. This is done in situ, during the MBE growth process of the wafer, using focused ion beam lithography [28].

Two identical double-layer samples are used for measuring the drag resistance in this project, which will be referred to as samples NA04 and NA06. All measurements of double-layer samples presented in this project are for sample NA06, unless otherwise stated. The plan view of one of the samples used, sample NA04, is shown in Fig. 1.7. The labelling of the contacts is explained in the figure annotation. The resistance measurements described throughout this project refer to the resistance measured in the region of the sample between contacts 16 and 18. The length of the sample between these contacts is 60 μm and the width of the Hall bar is 60 μm, for both samples.

The procedure by which the two layers are defined is shown in Fig. 1.8. Experimentally, the correct operation of the defining gates can be determined by measuring the two-terminal conductance between contacts in different layers (different layers once the sample is defined: initially, all contacts are connected to the layers in parallel). Figure 1.9 shows how the conductance between the contacts drops to zero as the sample is defined by applying voltages to the defining gates. The black curve shows how the conductance drops due to the contacts to the upper layer being depleted on one side of the Hall bar, and corresponds to the transition from diagram

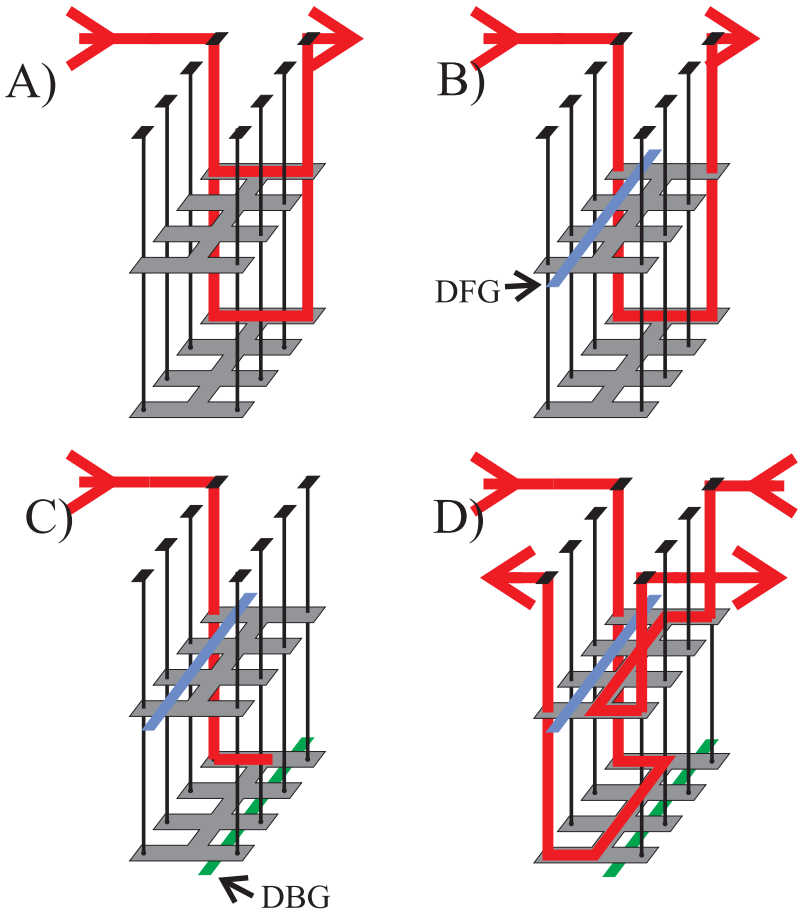

Figure 1.8: Illustration of the selective depletion technique used to define the layers, such that there are two independently contacted 2DEG layers. In **A**, all defining gate voltages are zero and all connecting arms to the Hall bar are conducting: current flows through both layers. In **B**, a voltage is applied to the defining front gate such that the 2DEG in arms of the top layer becomes depleted: current can now only pass through the bottom layer. In **C**, voltages are applied to both the defining front and defining back gates, and the sample is now defined. In **D**, currents are put through both the top and bottom layers, demonstrating that the two layers are contacted independently. Taken from [27].

B in Fig. 1.8 to diagram **C** in Fig. 1.8. Note that the conductance does not drop by half, as might be expected when the current can no longer flow through one of the layers. This is due to the fact that the upper layer does still carry some current at this stage: the sample is not yet fully defined. The red curve in Fig. 1.9 corresponds to the transition from diagram **B** in Fig. 1.8 to diagram **C** in Fig. 1.8. During this procedure the defining gate voltages are increased to a level such that the measured conductance is less than 10 nS, corresponding to a resistance between the layers of at least 100 MΩ.

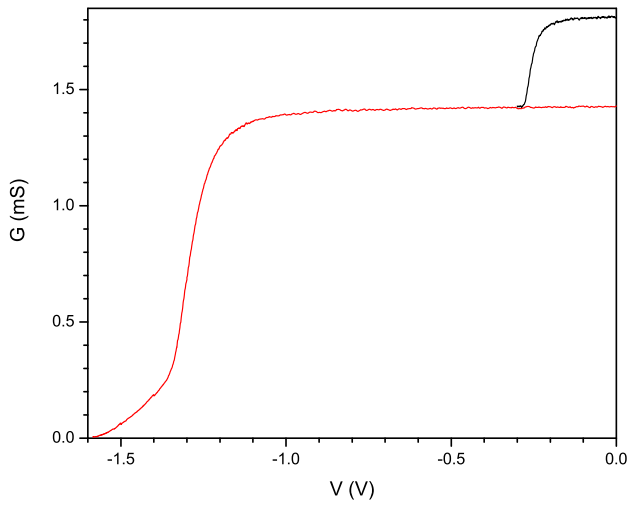

Figure 1.9: The conductance measured between contacts in the upper and lower layers as the sample is defined. The black curve is the conductance as a function of the front defining gate voltage whilst the back defining gate voltage is zero. The red curve is the conductance as a function of the back defining gate voltage whilst the front defining gate voltage is at 0.3 V. The actual defining-gate voltages required to deplete the arms to the Hall bar vary between cool-downs. Typical values are 0.3 V for the front defining gates, and 1.2 V for the back defining gates.

1.6 Equipment used

1.6.1 Cryogenic apparatus

The measurements performed in this project require very low temperatures ($T = 30\,\mathrm{mK} - 10\,\mathrm{K}$) and high magnetic fields (B = 0 - 15 T). To achieve this range of temperature and magnetic field we use two pieces of cryogenic equipment: an Oxford Instruments Heliox VL ^{3}He sorption cryostat and a Kelvinox 300 ^{3}He/^{4}He dilution refrigerator.

The Heliox VL ^{3}He system is capable of producing temperatures between 240 mK and 30 K, and magnetic fields between 0 and 2 T. The Kelvinox 300 ^{3}He/^{4}He dilution refrigerator allows for accurate temperature control between 30 mK and 800 mK, as well as limited temperature control between 800 mK and 5.5 K. The system incorporates a superconducting solenoid capable of producing magnetic fields of ± 17 T.

1.6.2 Magnetic field coils and power supplies

In measurements of mesoscopic conductance fluctuations (discussed in chapters 2, 3, and 4) the minimum possible step size in magnetic field is important. This is determined by the power supply used to generate current in the superconducting

solenoids of the cryogenic systems. The power supply used in our measurements is an Oxford Instruments IPS120-10, which has a current resolution of 0.1 mA and a minimum sweep rate of 0.001 Amps per minute. These limitations correspond to different resolutions in magnetic field for the Heliox VL and Kelvinox 300 systems, due to the difference in their coils. In the Heliox VL, the coil produces a magnetic field of 43.8 mT per Amp, and so has a resolution in magnetic field of $\Delta B = 4.4\,\mu$T and a minimum sweep rate of $\dot{B} = 2.6\,$mT/hr. The coil of the Kelvinox 300 produces a magnetic field of 148 mT per Amp, resulting in a resolution of $\Delta B = 14\,\mu$T and a minimum sweep rate of $\dot{B} = 8.6\,$mT/hr.

1.6.3 Voltage measurement, and noise reduction

AC voltage measurements were made at low frequencies, typically $f = 12.35$ Hz, using Perkin-Elmer Instruments lock-ins, models 7225 and 7265.

Standard noise reduction techniques were used: the sample and cryogenic system were enclosed in a screen room that filters out ambient electromagnetic radiation in the GHz range of frequencies. Connection to the sample were made via a filter panel in the screen room that incorporated low-pass filters of various cut-off frequencies. DC signals were passed through filters with cut-off frequencies of $f_c = 65$ Hz, whilst AC signals were passed through filters with $f_c = 33$ kHz (this frequency is much higher than the measurement frequency of 12.35 Hz). The measurement frequency of 12.35 Hz was chosen so as to avoid interference from the 50 Hz frequency of the electrical mains. Instruments were connected to the mains via an isolation transformer so as to reduce noise originating from the mains ground. The measurement circuit is grounded via a single connection to the well-earthed screen room.

The minimum level of the noise in our voltage measurements is generally limited by the voltage preamps used for measuring small signals. The voltage preamps used are NF Electronic Instruments model LI-75A low noise preamplifiers, which produce a voltage noise of 1.2 nV/$\sqrt{\text{Hz}}$ at the voltage input. In order to calculate the voltage noise in the measurement, the equivalent noise bandwidth (ENBW) of the lock-in is required, which depends upon the size of the time constant used. In measurements of small voltage signals, a typical value for the time constant used is 10 s, which corresponds to a ENBW of 0.01 Hz. Thus, the voltage noise in our measurements

is typically ~ 0.1 nV, placing a limit on the minimum measurable voltage signal of ~ 0.5 nV.

1.7 Conductance and resistance measurements

In studying the transport properties of the samples, the conductance and the resistance are two quantities measured. In order to measure either the conductance or resistance the current passing through the sample must be known, as well as the voltage drop along the sample associated with that current. In practice, either the current is held constant and the voltage drop is measured, which we refer to as a resistance measurement, or the the voltage across the sample is held constant and the resulting current measured, which we refer to as a conductance measurement.

In order to create a constant current a large "ballast" resistor is placed in series with a voltage source (such that the sample resistance is always smaller than the ballast resistance).

A constant voltage measurement is possible through the use of a potential divider, like that shown in Fig. 1.10. In order for the voltage drop across the sample to be constant, the resistance R_2 of the potential divider and internal impedance of the current pre-amp must both be much smaller than the sample resistance R.

1.7.1 Two-terminal conductance measurements

The circuit schematic for a two-terminal conductance measurement is shown in Fig. 1.10. A constant voltage of V_c is applied to the source contact of the sample, and the current I_m leaving the drain contact is measured using a current pre-amp. The conductance is then found from the ratio of the current to the voltage: $G_m = I_m/V_c$. The disadvantage of this two-terminal approach to measuring the conductance is that the contact resistances r are also included in the measurement. These contact resistances can be much larger than the measured sample resistance, and these contact resistances can have their own temperature and magnetic field dependences. For these reasons, it is always preferable to make four-terminal measurements of the resistance.

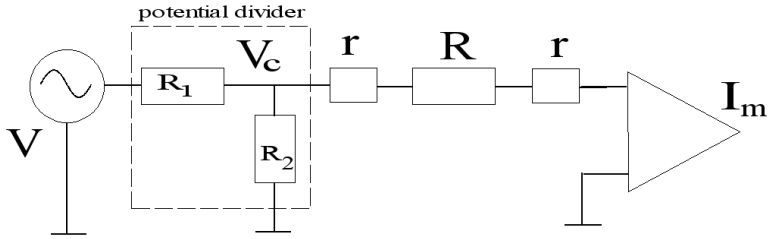

Figure 1.10: Two terminal conductance measurement. A constant voltage V_c is set using a potential divider formed by resistances R_1 and R_2. The sample has a resistance R and contact resistances r. The current through the sample, I_m, is measured using a current pre-amp.

1.7.2 Four-terminal resistance measurements

The circuit schematic for a four-terminal resistance measurement is shown in Fig. 1.11. A constant current I is passed from the source contact to the drain contact, which is connected to ground. The voltage drop across the sample is measured through a separate pair of contacts using a voltage pre-amp. In this method there is no voltage drop across the contact resistances associated with the voltage probes, as the voltage probes are connected in series with a voltage pre-amp that has very large input impedance and hence allows very little current flow. Thus, the voltage measured by the voltage pre-amp in this four-terminal circuit is independent of the contact resistances. Provided that there are sufficient contacts to the sample, four-terminal resistance measurements are always used in preference to two-terminal measurements throughout this project.

1.8 Synchronous Offset Measurement

The length of the samples used in this project are of the order of $L \sim 100\,\mu$m, which is typical of samples previously used in Coulomb drag measurements [29]. However, whilst this large size is advantageous for measuring the small voltages associated with the drag effect, it is disadvantageous when attempting to measure mesoscopic effects such as universal conductance fluctuations (discussed in Section 2.1.1), as these fluctuations decrease with increasing sample size and are normally measured on size scales of a few microns. Thus, when measuring mesoscopic fluctuations in the single-layer resistance in our structures, we need to be able to resolve fluctuations that are

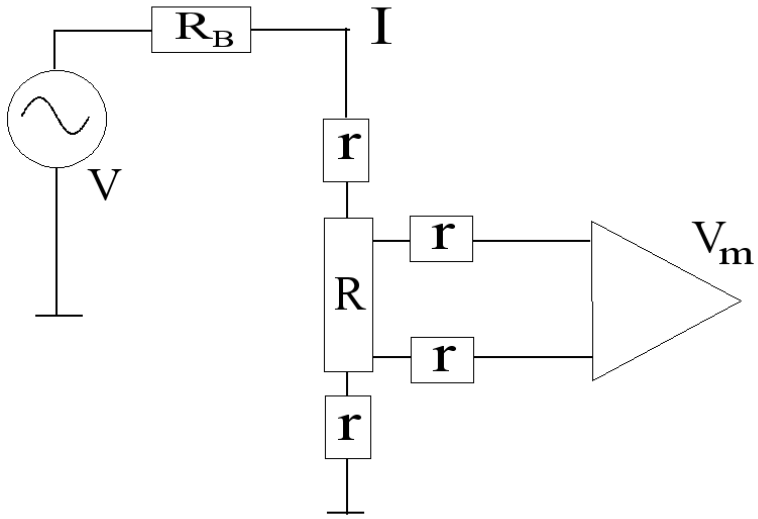

Figure 1.11: Four terminal resistance measurement. A constant current I is set using a large ballast resistance $R_B \gg R, r$. The sample has a resistance R between the probes and contact resistances r. The voltage drop V_m is measured across the sample using a voltage pre-amp.

typically three orders of magnitude smaller than the background resistance. In order to resolve such small corrections to a large signal, a useful measurement technique exists called the synchronous offset technique that allows a large background to be removed from a voltage signal whilst still allowing a lock-in technique to be used.

This is a facility available on Model 7265 Perkin-Elmer lock-ins, where an external voltage source, set to the correct frequency and phase, can be connected to the "B" input of the 7265 lock-in, and the measured voltage signal from the sample connected to input "A". The 7265 lock-in then measures the voltage difference $V_A - V_B$. The advantage of this method is that the sensitivity of the lock-in can now be set such that the lock-in's full scale is of the same size as the fluctuations being measured.

1.9 Characterisation of sample

In characterising our double-layer samples the four-terminal resistance as a function of gate voltage is measured. The transport properties of the 2DEG can then be derived from these measurements provided that the concentration dependence upon gate voltage is known. The concentration as a function of gate voltage is measured

using the Hall effect: $n = 1/R_H$, where R_H is the Hall coefficient. Using the Hall measurements, the concentration dependence of the resistivity of the upper layer of sample NA04 is plotted in Fig. 1.12. The mobility of the upper and lower layers are essentially the same in both samples NA04 and NA06. Using these measurements the transport properties are found, and are tabulated in Table 1.1.

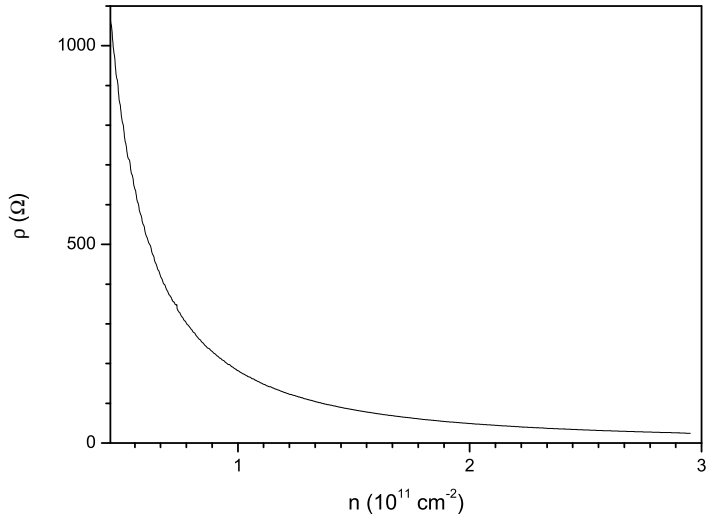

Figure 1.12: The resistivity as a function of concentration for the upper layer in sample NA04; $T = 4.2$ K.

V_G (V)	$n\,(10^{11}\mathrm{cm}^{-2})$	$\rho\,(\Omega)$	τ_p (ps)	$\mu\,\mathrm{cm}^2/\mathrm{Vs}$	$D\,\mathrm{cm}^2/\mathrm{s}$
0	2.95	24.6	33.4	87.6	9120
-0.05	2.46	33.9	29.1	76.2	6610
-0.10	1.96	50.7	24.3	63.8	4420
-0.15	1.47	86.8	19.0	49.8	2580
-0.20	0.97	192	12.9	33.9	1160
-0.25	0.47	968	5.34	14.0	231

Table 1.1: Transport properties of double-layer samples.

1.10 Characterisation and Observation of Coulomb Drag

The first stage in measurements of the drag resistance is to establish that the voltage measured is indeed due to the Coulomb drag between the layers, and not some spurious voltage, such as one arising from a current tunnelling directly between the

layers. Whilst the first check that this is the case is to measure the two-terminal conductance between the layers, as is done when defining the sample as discussed previously, there is an additional check that exploits the Coulomb drag mechanism. This second test is to see whether the voltage measured in the passive layer changes when the grounding point of the passive layer is changed [14].

Once spurious signals are ruled out, the next step is to reproduce the observations of Coulomb drag of other groups. These are namely: the T^2 temperature dependence of the drag resistance; the concentration dependence of $\rho_D \propto n^{-3}$; and also the observation of a phonon-mediated contribution to the drag for high concentrations where the Coulomb drag is expected to be smaller.

1.10.1 Detecting and reducing spurious signals

A schematic of the measurement circuit used to measure the drag resistance is given in Fig. 1.13. A constant current is passed through the active layer and a voltage is measured in the passive layer. The points in the passive layer labelled **A** and **B** refer to contacts where the passive layer can be grounded.

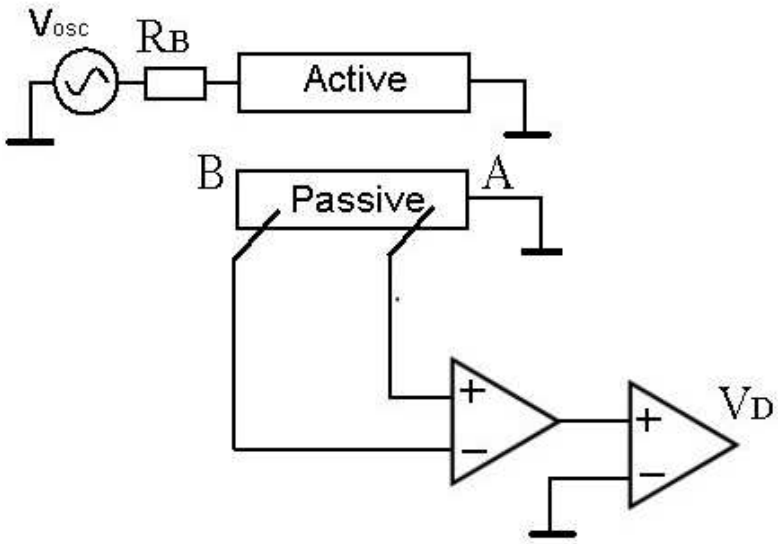

Figure 1.13: Drag voltage measurement circuit. The passive layer can be grounded at point **A** or **B**. Ideally, the voltage V_D measured in the passive layer is the drag voltage. However, in the case of current flowing between the layers due to tunnelling or capacitive coupling, there can be additional contributions to this voltage.

The voltage V_D measured in the passive layer will be a combination of the drag voltage, the voltage drop due to any direct tunnelling current, V_{tun}, and the voltage

drop due to current flow via capacitive coupling between the layers, V_{cap}: $V_D = I_A R_D + V_{tun} + V_{cap}$. The sign of the voltage drop due to the drag is determined only by the direction of current flow in the active layer, and is not affected by whether **A** or **B** is grounded in the passive layer. However, the voltage drop due to the tunnelling and capacitive currents will change sign when the grounding point is changed, as these currents flow to the point of lowest potential in the passive layer. Thus, the voltage across the passive layer when point A is grounded is $V_D^A = I_A R_D - V_{tun} - V_{cap}$, whilst the voltage in the passive layer for point B grounded is $V_D^B = I_A R_D + V_{tun} + V_{cap}$. By taking the average of these two measurements we retrieve the drag voltage, $V_D = (V_D^B + V_D^A)/2$. Note, however, that this assumes that the voltage drop due to a tunnelling current is the same for either grounding configuration of the passive layer, which will only be the case if tunnelling occurs uniformly between the layers. Tunnelling between the layers may occur at some "hot spot" between the layers, and taking the average of V_D^A and V_D^B will not correctly give the drag voltage. For this reason, if there is any difference in the voltage measured across the passive layer upon changing the grounding position between A and B, then the sample is not used for measurements.

If the voltage is dominated by the Coulomb drag voltage, then the voltage measured in the passive layer is not significantly different when measured with either point **A** or point **B** grounded. This is the case in our samples when the layers are well defined, as demonstrated in Fig. 1.14. The inset of Fig. 1.14 shows what would be seen if there were a large leakage current. In order to minimise the capacitive coupling between the layers, a low frequency of 12.35 Hz is chosen for the driving current .

1.10.2 Carrier density dependence of the drag resistance

In order to measure the carrier density dependence of the drag resistance, the drag voltage is measured in the passive layer whilst the concentration in the passive layer is varied. This is done for several fixed carrier concentrations in the active layer. Two such dependences are shown in Fig. 1.15, one for an active-layer concentration of $n_1 = 2.75 \times 10^{11}\,\mathrm{cm}^{-2}$ (black line) and $n_1 = 1 \times 10^{11}\,\mathrm{cm}^{-2}$ (red line). The results are plotted on a logarithmic scale so as to make the power-law dependence

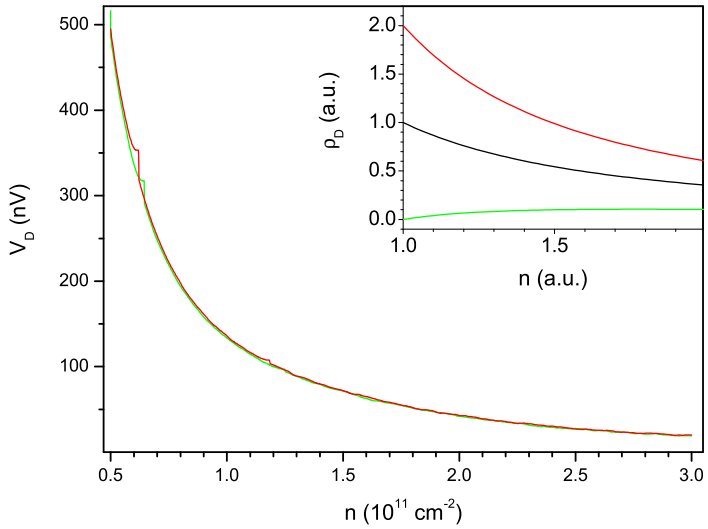

Figure 1.14: The voltage measured across the passive for different grounding points of the passive layer in sample NA04. The green and red curves are for points A and B grounded, respectively; $T = 4.2$ K. Inset: schematic representation of V_A and V_B measurements if there is a large leakage current from the active layer into the passive layer. The black curve is the average of the two measurements, $(V_A + V_B)/2$ and corresponds to the drag signal.

on concentration clear. From Eq. 1.12 we expected the graphs in Fig. 1.15 to have a gradient of $-3/2$. However, similar to the observations of other groups [25, 26] we observe a stronger dependence: the dashed lines in Fig. 1.15 are best fits using a $-3/2$ power, whilst the dotted lines are best fits using a -2 power. When there is a high electron concentration in the active-layer (black curve) there is a clear deviation from this $\rho_D \propto n_2^{-2}$ dependence at high concentrations in the passive layer. This indicates a significant contribution from phonon-mediated drag, which we observed for high ($n > 1.5 \times 10^{11}$ cm^{-2}) matched layer densities (discussed in the next section).

1.10.3 Evidence of phonon mediated contribution to the drag resistance

As was discussed in section 1.3.1, phonon-mediated drag can make a significant contribution to the measured drag resistance in samples where the Coulomb drag is small, such as in samples where the interlayer spacing is large. The observation of phonon-mediated drag in [16] was made in samples with similarly sized barriers ($d \approx$

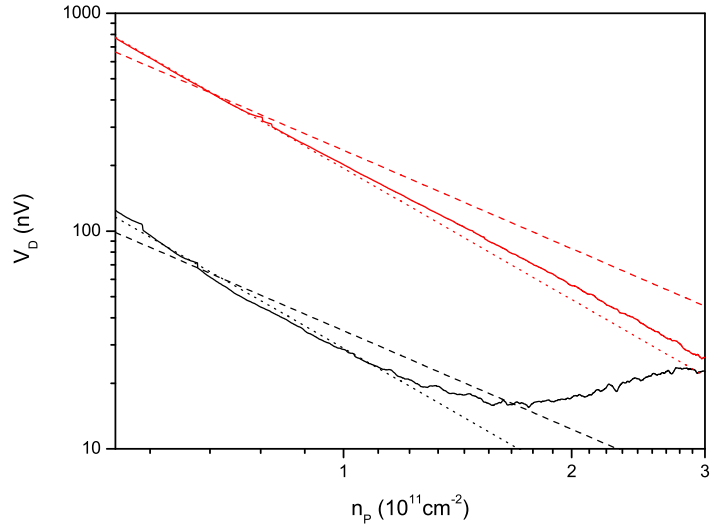

Figure 1.15: The drag resistance as a function of passive-layer carrier density for two different active-layer carrier densities, $n_1 = 2.75 \times 10^{11}\,\mathrm{cm}^{-2}$ (black) and $n_1 = 1 \times 10^{11}\,\mathrm{cm}^{-2}$ (red) in sample NA04. The dashed lines are best fits using $n_2^{-3/2}$ and the dotted lines are best fits n_2^{-2}; $T = 4.2$ K.

$200\mathring{A} \rightarrow 5000\mathring{A}$) and carrier concentration $1.5 \times 10^{11}\,\mathrm{cm}^{-2}$. Thus, it is expected that for high concentrations in our samples there can be an observable contribution from phonon-mediated drag in the measured drag resistance. Figure 1.16 shows the drag voltage as a function of the passive-layer concentration for several different active-layer concentrations. There are clear peaks in the drag voltage, and these peaks occur when the passive-layer concentration matches the active-layer concentration (these points are high-lighted in Fig. 1.16). Furthermore, this peak in the drag is only visible for the highest values of concentration, and is not seen for concentrations below $n \approx 1.5 \times 10^{11}\,\mathrm{cm}^{-2}$.

1.10.4 Temperature dependence of the drag resistance

The temperature dependence of the drag resistance is shown in Fig. 1.17 for matched layer densities of $n = 1 \times 10^{11}\,\mathrm{cm}^{-2}$. As expected, the drag resistance increases with increasing temperature: the solid line is the calculated drag resistance using Eq. 1.12, multiplied by a factor of 4. This disparity between the measured drag resistance and that predicted by theory is typical of that observed by other groups [14, 15, 30]. The drag resistance is well described by the T^2 dependence at temperatures below

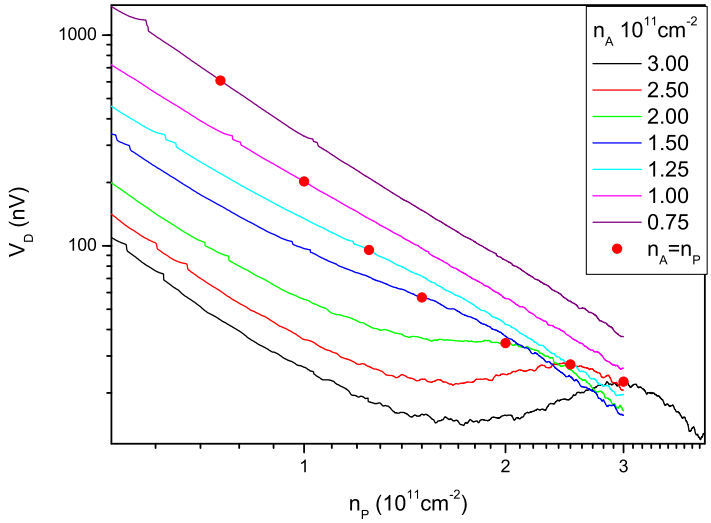

Figure 1.16: Drag voltage as a function of passive-layer concentration for different fixed active-layer concentrations. Red circles denote points where the active- and passive-layer concentrations are matched in sample NA04. Note that a peak occurs in the drag resistance when the layer concentrations are matched, indicating a phonon-mediated drag contribution; $T = 4.2$ K.

7 K, whilst at higher temperatures the strength of the temperature dependence of the drag seems to decrease. We can not account for the deviation from a T^2 dependence at higher temperatures. Other groups have reported deviations from a T^2 dependence due to contributions to the drag from virtual phonons [16, 19] and plasmons [22]. However, as seen in Fig. 1.16, the contribution to the drag resistance from phonons is not significant for low concentrations in our samples, whilst the temperature dependence in Fig. 1.17 is seen for all concentrations from $n = 0.5 \times 10^{11}\,\mathrm{cm}^{-2}$ to $n = 2.75 \times 10^{11}\,\mathrm{cm}^{-2}$. The enhancement of the drag due to plasmons only becomes significant for temperatures above $0.2T_F$. For our concentration range, $0.2T_F = 5$ K to 25 K, such that plasmons could only contribute significantly for the lowest concentrations used, and would result in an increase in the drag resistance, in contrast to the deviation seen in Fig. 1.17.

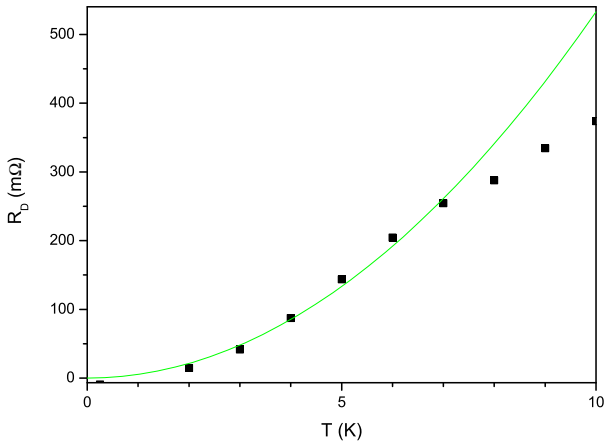

Figure 1.17: The drag resistance as a function of temperature for matched carrier densities in the two layers, $n = 1 \times 10^{11}\,\mathrm{cm}^{-2}$. The solid line is the calculated Coulomb drag using Eq. 1.12, with a prefactor of 4 included (this factor has been seen by other groups, as discussed in main text).

Chapter 2

Mesoscopic Fluctuations in Coulomb Drag

2.1 Mesoscopic Physics

The term mesoscopic refers to size scales that are of the order of the coherence length L_φ of charge carriers - the distance that carriers travel diffusively before losing their phase memory. In this regime of transport, the wave properties of electrons are observable, manifested in several different phenomena such as weak localisation and universal conductance fluctuations (UCF). Weak localisation refers to the divergence of the resistivity of mesoscopic systems as the temperature is decreased, whilst UCF are reproducible fluctuations of the resistivity that occur as the magnetic field, carrier concentration or impurity configuration is varied. Studies of these phenomena continue to provide a useful means of determining L_φ, which itself can reveal information about the strength of different inelastic scattering mechanisms within the system.

In the diffusive regime of transport where the sample size is much greater than the average distance between elastic scatterers, $L \gg l$, the coherence length is dependent upon the diffusion coefficient D and the coherence time τ_φ: $L_\varphi = \sqrt{D\tau_\varphi}$. The coherence time is limited by the rate at which electrons are scattered inelastically, such as in electron-electron (e-e) and electron-phonon scattering events. At low temperatures, where the density of phonons is small, the dominant inelastic scattering mechanism is e-e interactions.

In e-e interactions electrons are considered as quasi-particle excitations of the Fermi-liquid sea of electrons with respect to the Fermi energy. In this picture the typical energy of electrons is k_BT, due to the electron's distribution in energy states around the Fermi energy. The behaviour of e-e interaction is affected by the presence of disorder and can be separated into two distinct regimes - the "diffusive" or "ballistic" regimes, defined by the parameter $k_BT\tau/\hbar$, where τ is the momentum relaxation time. Given that e-e interaction occurs on an energy scale of k_BT, the typical time between e-e scattering events is $\tau_{ee} \sim \hbar/k_BT$. If this time is greater than the momentum relaxtion time τ, i.e. $k_BT\tau/\hbar < 1$, then electrons move diffusively experiencing multiple elastic scattering events before scattering inelastically via an e-e scattering event: this is the so-called diffusive regime of e-e interactions. In the opposite limit of $k_BT\tau/\hbar > 1$ electrons are in the ballistic regime of e-e interactions. The parameter $k_BT\tau/\hbar$ that determines the diffusive/ballistic nature of e-e interaction is often referred to as just $T\tau$, i.e., expressed in units where $k_B = \hbar = 1$.

As e-e interactions are the dominant dephasing mechanism at low temperatures, τ_φ has different T-dependences under different conditions of $T\tau$ [31]:

$$\tau_\varphi^{-1} = \begin{cases} k_BT \ln g/(\hbar g) & T\tau < 1 \\ \pi(k_BT)^2 \ln(2E_F/k_BT)/(4\hbar E_F) & T\tau > 1, \end{cases} \tag{2.1}$$

where $g = G/(e^2/h)$ is the dimensionless conductance.

In the above discussion, fluctuations of the sample conductance are assumed to be of the same size, $\Delta G = e^2/h$, regardless of whether it is the gate voltage, magnetic field, or disorder configuration that is changed. This assumption is the ergodic hypothesis: that for a metal equivalent fluctuations are caused by changing impurity configuration, or by changing magnetic field or Fermi energy in a given sample [32].

2.1.1 Universal Conductance Fluctuations

Universal conductance fluctuations (for reviews see [32, 33]) are random, aperiodic fluctuations of the conductance as a function of magnetic field, chemical potential, and impurity configuration. Unlike noise, which is random fluctuations of the conductance as a function of time, UCF are reproducible upon repeating the same sweep

of B-field or gate voltage. This phenomenon is a result of interference of the various paths that electrons can take when traversing a sample and was treated theoretically by Altshuler, Lee, and Stone (ALS) [34,35]. Figure 2.1 gives a simplified illustration of current flow in a two-terminal sample. Two possible trajectories that electrons can follow in traversing from one contact to the other are shown. The conductance of the sample is related to the probability of an electron travelling from the left-hand contact to the right-hand contact per unit time. This probability of transmission in a time t is found from summing over all possible paths of connecting the two contacts:

$$P(r, r', t) = \left| \sum_i A_i \right|^2 = \sum_i |A_i|^2 + \sum_{i \neq j} A_i A_j^*, \tag{2.2}$$

where A_i is the probability amplitude of the i^{th} path connecting points r and r' within a time t. The summation is broken down into two terms on the right-hand side: the first term corresponds to the classical picture of electron diffusion between the contacts, whilst the second term considers quantum interference between the different paths. The phase relationship between A_i and A_j in this summation is random due to its dependence upon the random distribution of impurities, and so when summed over a very large number of paths it would be expected to cancel out. However, it has been shown [32] that in small 1D and 2D systems, comparable in size with L_φ, this term can not be neglected, even as $L/l \to \infty$. The effect of this term is to introduce a quantum mechanical term to the conductance that is sensitive to the interference between the different electron paths through a given impurity configuration. The phase difference between these paths, and thus the resulting interference, can be changed by changing the magnetic field, which induces a phase change in the electron wavefunction of $(e\hbar) \int_P \mathbf{A} \cdot \mathrm{d}\mathbf{r}$ (P is the electron path and $\mathbf{A}$ is the vector potential), or by changing the gate voltage, which changes the effective impurity configuration and thus the paths of the wavefunctions themselves.

As the magnetic field or gate-voltage is changed these terms will both fluctuate, resulting in fluctuations in G. As the size of the sample increases, the fluctuations due to the first term will self-average to zero (self-averaging is defined as the relative size of fluctuations going to zero as the size tends to infinity, $\Delta G/G|_{L\to\infty}$). However, in 2D systems the fluctuations due to the interference term have been shown not to

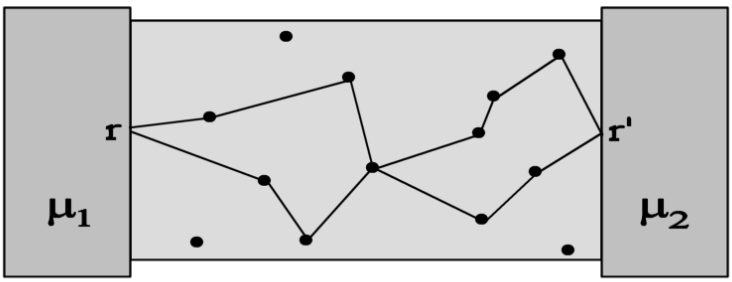

Figure 2.1: Two different trajectories that an electron can follow when passing through a disordered two-terminal sample.

self-average [32]. Indeed, it was shown that in 2D the absolute size of fluctuations is independent of sample size and geometry, having a universal value, provided the size of the sample is small enough and the temperature is low enough:

$$\Delta G \sim \left(\frac{e^2}{h}\right)^2 . \tag{2.3}$$

This expression is derived under the condition that the sample is diffusive, $l \ll L$; a good metal, $g \gg 1$; and at low temperatures such that $L_T, L_\varphi > L$ (these length scales will be discussed in the next section).

2.1.2 UCF at finite temperatures

Whilst at zero temperature the UCF are independent of sample size, as the temperature increases it becomes possible for decoherence of the electron trajectories to occur before the electron is able to traverse the sample, $L_\varphi < L$. In this case, the behaviour of the sample over a coherent area L_φ^2 is the same as in the zero temperature case, but outside this area the phase coherence is lost. Thus, a sample larger in size than L_φ behaves as a classical network of resistors each L_φ^2 in size and having different conductances that display a variance of $\Delta G = e^4/h^2$ as shown in Fig. 2.2. Now the variance of the entire square sample as a function of magnetic field or gate

voltage will display a variance that is a classical average of the network of resistors:

$$\Delta G \sim \left(\frac{e^2}{h}\right)^2 \left(\frac{L_\varphi}{L}\right)^2 . \tag{2.4}$$

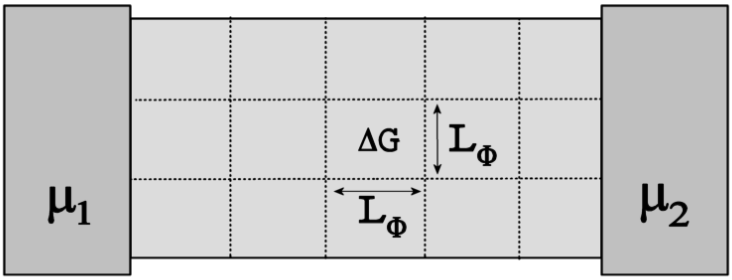

Figure 2.2: Two terminal sample that has been divided into coherent regions of L_φ^2, the conductance of which display a variance of ΔG.

In 2D systems it is often the case that the UCF are further averaged due to the thermal smearing of the Fermi-Dirac distribution. The thermal smearing is $k_B T$, corresponding to a decoherence time of $\hbar/k_B T$. In this time an electron travels $L_T = \hbar D/k_B T$, where L_T is called the thermal length. Thus, UCF are averaged by two different factors: L_φ/L and L_T/L_φ, resulting in the variance of the conductance fluctuations of

$$\langle \Delta\sigma^2 \rangle = \left(\frac{e^2}{h}\right)^2 \left(\frac{L_T}{L}\right)^2 , \tag{2.5}$$

if the condition that $L_T < L_\varphi$ is satisfied.

2.2 Autocorrelation functions

In order to characterise mesoscopic conductance fluctuations it is necessary to find the variance and correlation parameters of the fluctuations. The correlation parameter of a set of fluctuations is the typical size of the fluctuation in the quantity being

varied, i.e., a characteristic quasiperiod of the fluctuations. Both the variance and the correlation range can be extracted from a set of fluctuations by calculating the autocorrelation function (ACF) of the fluctuations.

The autocorrelation function, $F(\Delta x)$, of a quantity $f(x)$ is defined as:

$$F(\Delta x) = \lim_{X\to\infty} \frac{1}{X} \int_{-X/2}^{X/2} f(x) f(x + \Delta x) \mathrm{d}x, \tag{2.6}$$

where X is the interval over which $f(x)$ is measured. Obviously, it is not possible in an experimental setting to measure conductance fluctuations over an infinite range of gate voltage or magnetic field. However, this does not introduce a significant error provided that a sufficiently large number of fluctuations, of about 10 - 100, are covered over the interval X.

The correlation magnetic field B_c can be understood physically as the change in magnetic field necessary to increase the flux passing through a coherent area by one flux quantum:

$$B_c = \frac{h}{eL_\varphi^2}. \tag{2.7}$$

The correlation gate-voltage V_{gc} is that necessary to change the Fermi energy of the system by more than $E_c = \hbar/\tau_\phi$ [32]. This can be rewritten as the correlation concentration:

$$n_c = \frac{k_F l}{L_\varphi^2}, \tag{2.8}$$

where concentration n_c is related to V_{gc} by the capacitance $C_g$between the gate and the 2DEG, $en_c = C_g V_{gc}$.

2.3 Fluctuations in diffusive drag (existing theory)

Given that mesoscopic fluctuations are averaged out in large samples where $L \gg L_\varphi$, and that the drag resistance is itself a small quantity for typical sample parameters, it would seem unlikely that measuring mesoscopic fluctuations of the drag resistance would be possible under realistic conditions. However, when the mesoscopic

behaviour of drag was first discussed by Narozhny and Aleiner [36], they found that, contrary to this simple consideration, mesoscopic fluctuations of the drag resistance could actually exceed the size of the average drag resistance. Furthermore, this means that mesoscopic fluctuations could lead to changes in the sign of the drag resistance upon changing either the carrier concentration or by applying a magnetic field.

The quantity studied theoretically in [36] is the drag conductance, σ_D, whilst in the experimental setting the measured quantity is the drag resistivity ρ_D. The drag conductivity and drag resistivity can easily be converted using the following tensor relations:

$$\begin{pmatrix} V_1 \\ V_2 \end{pmatrix} = \begin{pmatrix} \rho_1 & \rho_D \\ \rho_D & \rho_2 \end{pmatrix} \begin{pmatrix} I_1 \\ I_2 \end{pmatrix}. \tag{2.9}$$

Here $V_{1,2}$ and $I_{1,2}$ are the voltages and currents in the active (1) and passive (2) layers, respectively. Under ideal experimental conditions where there is no current flow in the passive layer, such that $I_2 = 0$, we retrieve the usual expressions for the voltages in the active and passive layers: $V_1 = \rho_1 I_1$ and $V_2 \equiv V_D = \rho_D I_1$, respectively. Thus, the drag conductivity is found simply from the inverse of this resistivity tensor:

$$\sigma_D = \frac{\rho_D}{\rho_1\rho_2 - \rho_D^2} \approx \frac{\rho_D}{\rho_1\rho_2}. \tag{2.10}$$

Here we have taken the simplifying limit of $\rho_D \ll \rho_{1,2}$, which is the usual case in Coulomb drag experiments to date.

In [36] the drag is described as being dependent on three factors: the available phase space for e-e scattering, the interaction matrix elements that describe interactions between electrons in the two layers, and the degree of electron-hole asymmetry. This latter factor refers to the fact that electrons and holes (remembering that this is in the context of e-e interaction an so electron/hole refers to excitations of the Fermi sea within k_BT above/below the Fermi energy) both carry momentum in active and passive layers. If there is no asymmetry in the properties of electrons and holes, then there will be no Coulomb drag.

The fact that UCF in the drag can exceed the average drag comes from the

different energy scales involved in the average electron-hole asymmetry and the fluctuations in the electron-hole asymmetry. The electron-hole asymmetry can be related to the derivative of the DOS $\varrho(E)$ and/or diffusion constant, D, with respect to the chemical potential μ: $\partial(\varrho(E)D)\partial(\mu)$ [36]. The average asymmetry goes as g/E_F, whilst the characteristic energy of the asymmetry of the mesoscopic fluctuations is the so-called Thouless energy $E_{Th} = \hbar D/L^2$, which appears in the denominator instead of the Fermi energy. E_{Th} is much smaller than E_F, resulting in the fluctuations of the Coulomb drag being able to exceed the average drag [36].

Given the large size of the drag fluctuations at low T and the fact that the average drag decreases with decreasing T, it is clear that at some critical temperature T_* there will be a crossover from the average Coulomb drag dominating the measured drag conductance to a low T-regime where the mesoscopic drag is dominant [36]. This behaviour is sketched in Fig. 2.3.

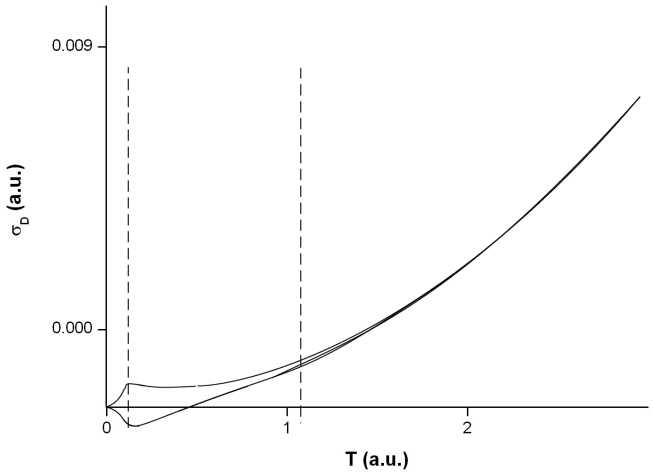

Figure 2.3: Sketch of the expected T-dependence of the measured drag conductivity in the three different regimes described in [36]: $T > T_*$, $E_{Th}(L)/k_B < T < T_*$, and $T < E_{Th}(L)/k_B$ (dashed lines indicate approximate transition temperatures). T_* is the crossover temperature at which the size of mesoscopic drag resistance fluctuations is equal to the size of the average drag resistance.

At low T where $L_T > L$ the fluctuations in the single-layer conductance take the universal value of e^2/h. The drag conductance will additionally be affected by the phase space available for e-e scattering, the interaction matrix elements, and the e-h asymmetry. The asymmetry in each layer is temperature-independent and depends on the energy E_{Th}, whilst the elements of the interaction matrix are also

T-independent, and go as $\sim 1/g$. The only temperature dependence comes from the phase space factor, which goes as T^2. Thus, in this low-T regime the drag conductance fluctuations are expected to go as [36]

$$\Delta\sigma_D \sim \frac{e^2}{h}\frac{T^2}{(E_{Th}g)^2}. \tag{2.11}$$

The intermediate temperature regime in which $L_\varphi < L$ requires not only the usual spatial averaging equivalent to dividing the sample into L_φ/L fluctuating resistances, but also requires changing the values of the drag conductance fluctuations within a coherent area L_φ^2 calculated in Eq. 2.11. Two things change that affect the size of such fluctuations: the fluctuations of the density of states in each layer are suppressed by a factor L_T/L, and the matrix elements become energy dependent such that the phase space factor is reduced from T^2 to T/τ_φ. This results in the following dependence of the drag conductance [36]:

$$\langle\sigma_D^2\rangle = \gamma\frac{e^4}{\hbar^2}\frac{E_{Th}(L)\tau_\varphi \ln\kappa d}{\hbar g^4(\kappa d)^3}, \tag{2.12}$$

where the coefficient $\gamma = 0.0049$. Note that this is actually the average of the squared conductance, rather than the variance, i.e., the average drag conductance is also included in this expression. However, the experiments in this chapter will only use Eq. 2.12 when the average drag conductance is negligible in comparison to the mesoscopic drag fluctuation amplitude.

2.4 Drag fluctuations in the ballistic regime

Prior to the experimental work done by the author, the behaviour of the mesoscopic drag fluctuations in the ballistic regime, $l \gg d$, had not been addressed. For diffusive samples it had been shown theoretically [36] that at a critical temperature T_* the mesoscopic fluctuations of the Coulomb drag became the dominant contribution to the measured drag conductance. Furthermore, using sample properties typical of those available experimentally, Narozhny and Aleiner [36] estimated the size of T_* for a realistic system and found a value of $T_* = 0.2\,\mathrm{K}$, which is well within the experimentally accessible range of temperatures. However, there are two points of caution with this rough estimate. Firstly, all existing experimental systems to

date have been in the ballistic regime of drag, $l \gg d$, where d is the inter-layer separation, and so the predictions of [36] can not describe well the different physics in these samples. Secondly, T_* is related to the relative size of the drag fluctuations; if we instead calculate the absolute size of these fluctuations then for typical samples ($L = 60\,\mu$m, $L_\varphi = 1\,\mu$m, $g = 50$, $d = 500\,$Å, and $D = 44\,\mathrm{cm^2 s^{-1}}$) we arrive at an average fluctuations amplitude of the drag resistivity of $\mathrm{rms}\rho_D \sim 1\,\mu\Omega$. Given the restrictions on maximum size of driving currents that can be used in such low-temperature measurements, this corresponds to a voltage signal of $\sim 10\,$fV, which is beyond that experimentally possible to detect.

As will be discussed in the remainder of this chapter, fluctuations of the drag resistance are in fact much larger than this diffusive estimate would suggest, resulting in measurable resistivities of $\sim 50\,\mathrm{m}\Omega$. This result is surprising: given the usual increase in size of the Coulomb drag effect with decreasing concentration, one might naively expect the fluctuations of the drag to be similarly larger in the diffusive regime of drag. The results of investigations described in this chapter prompted further theoretical work by Narozhny on drag resistance fluctuations in the ballistic regime of drag (for a detailed description see [37] and accompanying supplementary online material).

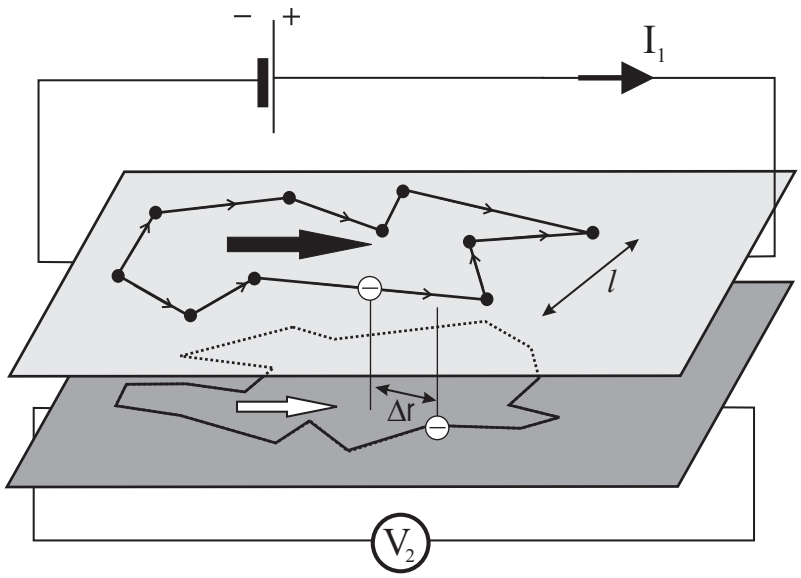

Figure 2.4: Physical model of drag resistance fluctuations in the ballistic regime of drag. Δr is the distance an electron travels within a layer between e-e scattering events with electrons in the other layer.

The physical picture of Coulomb drag fluctuations in the ballistic regime is il-

lustrated in Fig. 2.4. The electrons in each layer interfere with each other in the same manner described for UCF (Section 2.1.1), but also interact with electrons in the other layer whilst travelling over a typical distance Δr. The distance travelled by electrons between interlayer *e*-*e* scattering events is restricted by the wave-vector dependence of the screened interlayer interaction. As discussed in section 1.3, interlayer momentum transfer is exponentially cut-off for wave-vectors larger than the reciprocal interlayer separation distance d^{-1}. By the uncertainty relation, $\Delta q \delta r \sim 1$, the region over which an electron travels within a layer whilst transferring a momentum Δq to the other layer, is $\Delta r \sim d$. Thus, in the ballistic regime of drag where $d \ll l$ electrons explore a region Δr that is smaller than the elastic mean free path l. This means that in contrast to the diffusive case, it is the fluctuations of the *local* properties of the layers that contribute to the electron-hole asymmetry, and these are larger than those of the average properties as rare impurity configurations become important.

Taking this into account, and again considering the factors of phase space, interaction matrix elements, and *e*-*h* asymmetry, the variance of drag conductance fluctuations can be derived as

$$\langle \Delta\sigma_D^2 \rangle = N \frac{e^4}{g^2\hbar^2(\kappa d)^4} \frac{(k_B T)^2}{E_{Th}^2(L_\varphi)} \frac{l^4 L_\varphi^2}{d^4 L^2}, \tag{2.13}$$

where N is a numerical coefficient and $E_{Th}(L_\varphi) = \hbar D/L_\varphi^2$ is the Thouless energy on the scale of L_φ. The influence of the local properties of the sample results in several factors changing in this expression compared to Eq. 2.12. The phase-space factor is now T/E_{Th} due to the energy independence of the interaction matrix elements. The fluctuations of the local DOS go as $\delta\varrho(E)^2 \sim (\varrho(E)^2/g) \ln[\max L_\varphi, L_T/l]$ [38], resulting in an extra factor of g^2. Lastly, there is now a factor of $(l/d)^4$, which is similar to that seen in the average ballistic drag compared with the average diffusive drag, $\sigma_D(l \gg d)/\sigma_D(l \ll d)$ [39].

The temperature dependence of Eq. 2.13 is controlled by $T^2\tau_\varphi^3$, and so will depend upon the parameter $T\tau$, which affects the temperature dependence of τ_ϕ (Section 2.1). In the diffusive regime of *e*-*e* interaction, $T\tau < 1$, $\tau_\varphi \propto T^{-1}$, whereas at high temperatures, $T\tau > 1$, $\tau_\varphi \propto T^{-2}$. As a result,

$$\langle \Delta\sigma_D^2 \rangle \propto \begin{cases} T^{-1} & T\tau < 1 \\ \tau_\varphi \propto T^{-4} & T\tau > 1. \end{cases} \tag{2.14}$$

2.5 Measurement of L_φ in single-layer

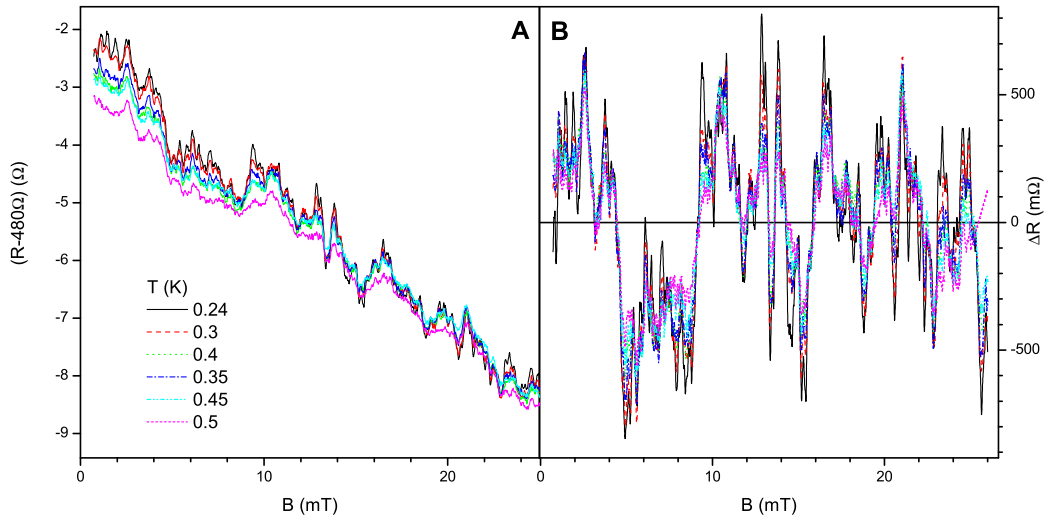

Figure 2.5: **A**: Single-layer resistance as a function of magnetic field for different temperatures; temperatures as described in legend. A resistance of 480 Ω has been subtracted at the point of measurement, as described in text. **B**: Single-layer resistance, after having background magnetoresistance removed, as a function of magnetic field for different temperatures. The concentration is held constant, $n_1 = 5.8 \times 10^{10}\,\mathrm{cm}^{-2}$; $I = 10$ nA.

Before attempting to measure conductance fluctuations in Coulomb drag it is sensible to measure the statistical properties of the single-layer conductance fluctuations. Although the single-layer resistance fluctuations are larger in absolute size than those expected in the drag resistance, they are much smaller than the average background resistance. To improve the resolution of the measurement of the small resistance fluctuations the synchronous offset technique is used, as described in Section 1.8. Panel **A** of Fig. 2.5 shows the single-layer resistance as a function of magnetic field for different temperatures below 1 K. Clear reproducible fluctuations are seen that decrease with increasing temperature and are of 1 Ω in size. Note, however, that the background resistance is about 480 Ω and so is more than 100 times larger than these fluctuations; furthermore, it is both B- and T-dependent.

Panel **B** shows the fluctuations of the resistance after a polynomial fit of the data in panel **A** has been subtracted from the measured resistance.

After the removal of the average background resistance the ACF of the mesoscopic conductance fluctuations can be calculated, and from this the variance and coherence length found. Figure 2.6 shows the temperature dependence of the amplitude of the single-layer conductance fluctuations. The solid line is a theoretical fit of the data using Eq. 2.5 including a prefactor of two. The factor of two discrepancy is typical of the quality of agreement found in other experiments [7], and is dependent upon the exact geometry of the sample. The inset to Fig. 2.6 shows the coherence time τ_φ found from the correlation magnetic field of the conductance fluctuations. The solid lines are the theoretical fits found using the diffusive (black line) and ballistic (red line) expressions, Eq. 2.1.

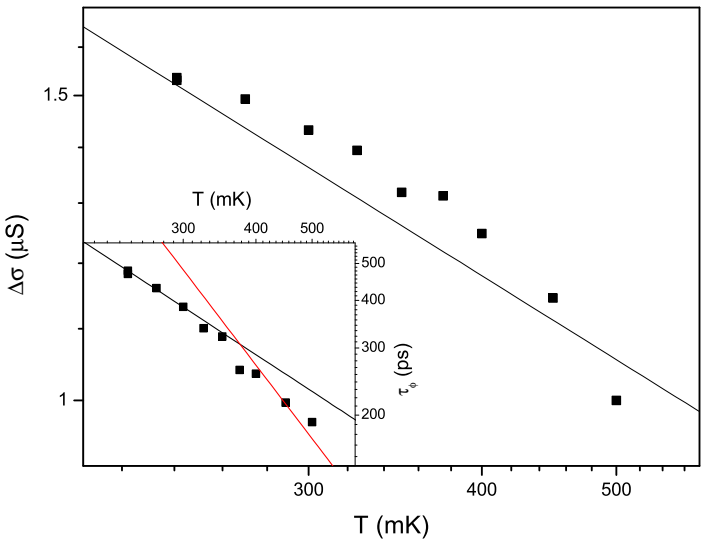

Figure 2.6: Amplitude of the single-layer resistance as a function of temperatures. The solid line is a calculation of the variance expected using Eq. 2.5, multiplied by a factor of 4 for ease of comparison to measured data. Inset: τ_φ as a function of temperature for the single-layer UCF. The black and red lines are fits using the diffuse and ballistic expressions for τ_φ described in Eq. 2.1, respectively. The concentration is held constant, $n_1 = 6.1 \times 10^{10}\,\mathrm{cm}^{-2}$; $I = 10$ nA.

2.6 Macroscopic to mesoscopic transition

In order to see the expected fluctuations in the drag resistance, the drag voltage was measured at $B = 0$ whilst the passive-layer concentration was varied. The active-layer concentration was held constant, $n_1 = 1.1 \times 10^{11}\text{cm}^{-2}$. This was done for a range of temperatures, the results of which are shown in Fig. 2.7. At higher temperatures the expected smooth concentration dependence is seen. However, as the temperature is lowered below 1 K fluctuations begin to appear in the drag resistance. These fluctuations are reproducible in n_2 for different temperatures, and are seen to increase in size as the temperature decreases. Furthermore, as was predicted in [36], the fluctuations exceed the average drag, resulting in an alternating negative and positive sign of the drag as the concentration is changed.

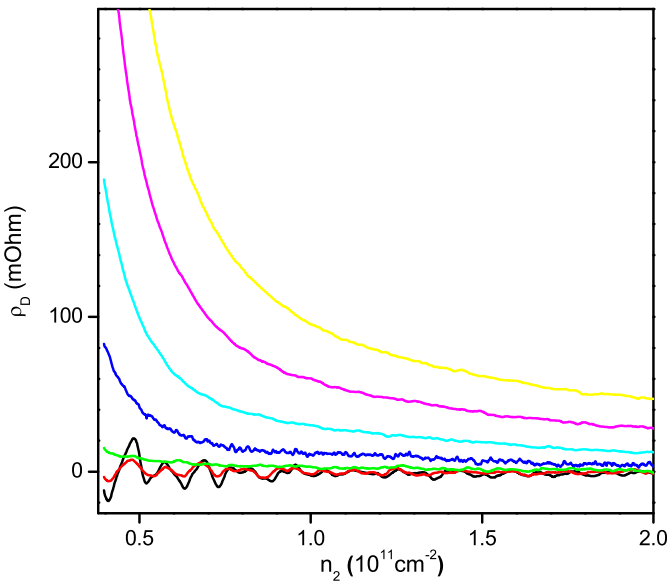

Figure 2.7: Drag resistivity as a function of passive-layer carrier concentration for different temperatures: $T = 5$, 4, 3, 2, 1, 0.4, and 0.24 K, from top to bottom. Active-layer concentration is held constant, $n_1 = 1.1 \times 10^{11}\,\text{cm}^{-2}$; $I = 675$ nA.

The fluctuations in the drag resistance are shown in detail in Fig. 2.8. A cross section of the results will show the temperature dependence of the drag resistance at different concentrations, and this is shown in the inset of Fig. 2.8. The red circles correspond to the peak in ρ_D marked by the red dashed line in the main panel, whilst the black squares correspond to the T-dependence of the ρ_D minima marked by the

black dashed line. The behaviour of the drag resistance with decreasing temperature (inset of Fig. 2.8) agrees with the predictions of [36] that were illustrated in Fig. 2.3.

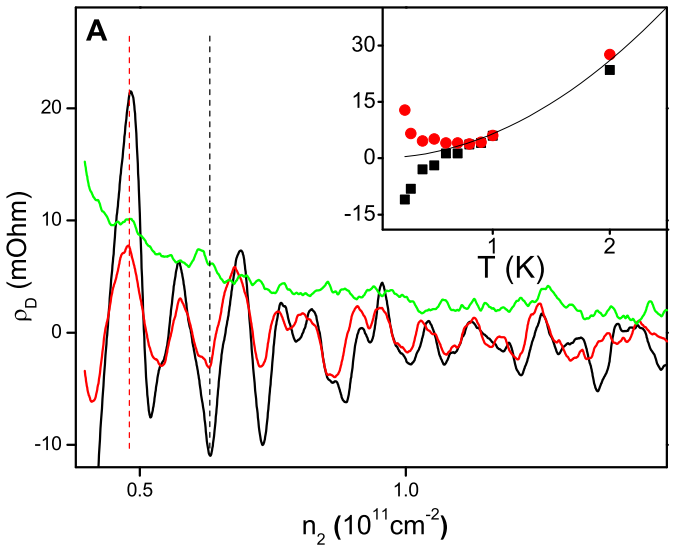

Figure 2.8: Drag resistance measured at low temperatures as a function of passive-layer concentration; $T = 1$, 0.4, and 0.24 K, from top to bottom. Inset: ρ_D as a function of T for two values of n_2 denoted by the dotted lines in main panel; solid line is the expected T^2 dependence of the average drag.

2.7 Fluctuations in drag resistance as a function of gate voltage and magnetic field

These fluctuations are also seen as the magnetic field is varied, as shown in Fig. 2.9. Given the strong dependence of the amplitude of the drag fluctuations on the conductance of each of the single layers, it is more convenient to measure the fluctuations of the drag resistance by varying the magnetic field whilst holding the concentration of each layer constant. (This is due to the weak B-field dependence of the single-layer conductance at low B-fields.) When analysing the fluctuations, L_φ is extracted from measurements by averaging the results over the range of B. Therefore, it is important that the variance and correlation length of the fluctuations are not themselves varying as a function of magnetic field being varied. For similar

conditions of the single-layer concentrations and conductances the variance of the drag resistance is the same when either the magnetic field or concentration is varied, i.e., the fluctuations are ergodic.

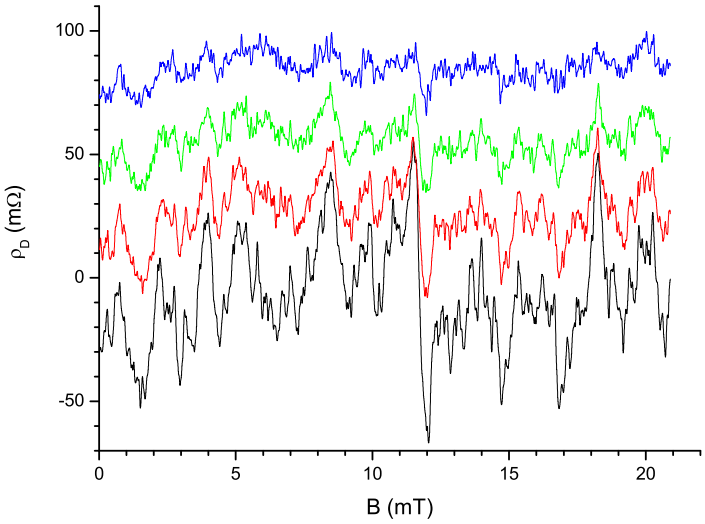

Figure 2.9: Drag resistivity as a function of magnetic field for different temperatures; $T = 0.24$, 0.3, 0.35, 0.4 K. The graphs at higher T are offset by 25 mΩ for clarity. The single-layer concentrations are held constant, $n_1 = 1.1 \times 10^{11}\,\mathrm{cm}^{-2}$, $I = 700$ nA.

At sufficiently large B-fields, $\omega_c\tau > 1$, the DOS begins to collapse in Landau levels, which is seen in the drag resistivity as Shubnikov de Haas oscillations. This introduces a complicated B-field dependent background that must be removed from the measured drag resistance in order to analyse the mesoscopic fluctuations. Furthermore, the statistical properties of the mesoscopic conductance fluctuations in each layer become B-field dependent at such large magnetic fields [40]. Figure 2.10 shows that SdH oscillations are clearly evident for $B > 90$ mT. These fluctuations were measured when the concentration and mobility are $n_{1,2} = 6 \times 10^{10}$ and $\mu = 208000\mathrm{cm}^{-2}/\mathrm{Vs}$; thus, this magnetic field corresponds to $\omega_c\tau = 1.9$. So as to avoid any influence of SdH oscillations in our measurements of the conductance fluctuations, the used interval of magnetic fields is restricted to $B < 30$ mT.

At sufficiently low temperatures the average drag resistance is much smaller than the amplitude of the fluctuations, although it was seen that on some cooldowns a large (of the same size as the fluctuations) B-dependent background drag resistance was present, the origin of which could not be identified. This background varied

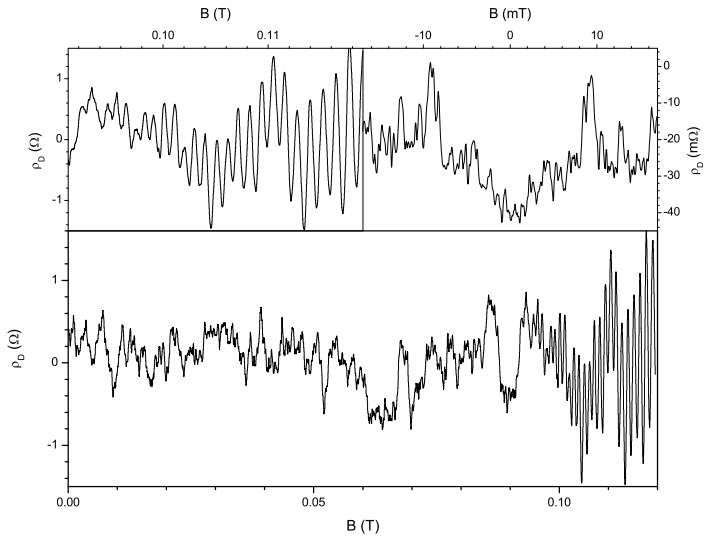

Figure 2.10: Drag resistivity as a function of magnetic field demonstrating onset of Shubnikov-de Haas oscillations in the drag resistance. The single-layer concentrations are held constant, $n_{1,2} = 6 \times 10^{10}\,\mathrm{cm}^{-2}$. The top left inset is a zoomed in view of the region in which SdH oscillations are present. The top right inset shows the symmetry of drag resistivity fluctuations with changing the direction of magnetic field.

slowly in B, sometimes having a nonmonotonic form. Furthermore, this background decreased in size with increasing temperature. Whilst the majority of measurements did not contain this unusual background, it is still necessary to remove the non-zero average background so as to isolate the fluctuations in ρ_D from which the variance and correlation period can be found.

After removal of the average background magnetoresistance, the ACF $F(\Delta B)$ of the fluctuations is calculated. One such ACF is shown in Fig. 2.11 for a set of drag conductance fluctuations measured at $T = 50$ mK.

2.8 Temperature dependence of variance and L_φ

The temperature dependence of the drag conductance fluctuations is shown in Fig. 2.12, along with the low and high temperature fits of Eq. 2.13 (solid and dashed lines, respectively). The two different temperature dependences are well developed, with a transition at $T \approx 200\,\mathrm{mK}$. These fits were calculated using the values of τ_φ shown in the inset of Fig. 2.12, which were found from the correlation field B_C

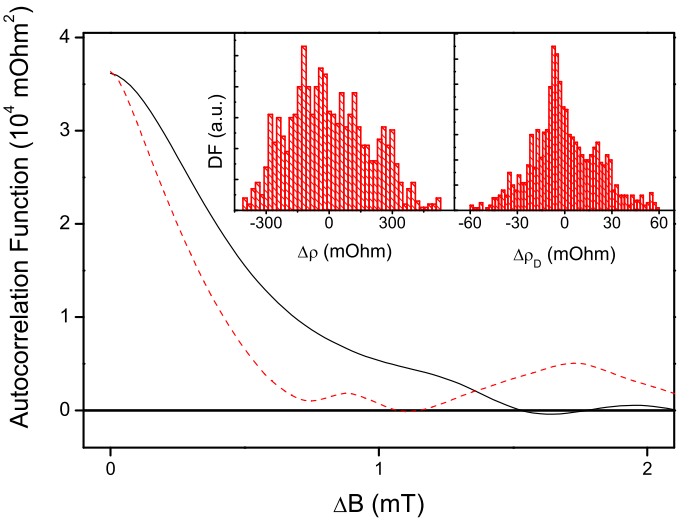

Figure 2.11: The ACF calculated for a set of drag conductance fluctuations (black line) and single-layer conductance fluctuations (red line). The single-layer concentrations are held constant, $n_{1,2} = 6 \times 10^{10}\,\mathrm{cm}^{-2}$. The left and right insets show histograms of the distribution of the single-layer and drag resistance fluctuations, respectively.

of the single-layer conductance fluctuations described in Section 2.5. The solid and dashed lines in the inset are plots of the calculated τ_φ using Eq. 2.1. The transition from diffusive to ballistic regimes with changing $T\tau$, although less apparent in $\tau_\varphi(T)$, occurs at $T \approx 400\,\mathrm{mK}$ (corresponding to $T\tau = 0.4$) in reasonable agreement with that seen in the drag variance, where the transition occurs at $T\tau = 0.2$. The numerical coefficient N in Eq. 2.13 is found to be 10^{-4} in the whole range of T. There is no current theoretical prediction for the value of this numerical coefficient.

2.9 Conclusion and further work

We have observed for the first time reproducible fluctuations of the Coulomb drag resistance. These fluctuations are shown to result from coherent transport of the electrons similar to that predicted recently [36]. These fluctuations are seen both as a function of carrier concentration and magnetic field. Furthermore, we observed the extraordinary effect where the mesoscopic fluctuations of the drag resistance exceed the average drag such that the sign of the drag resistance changed randomly with varying n and B.

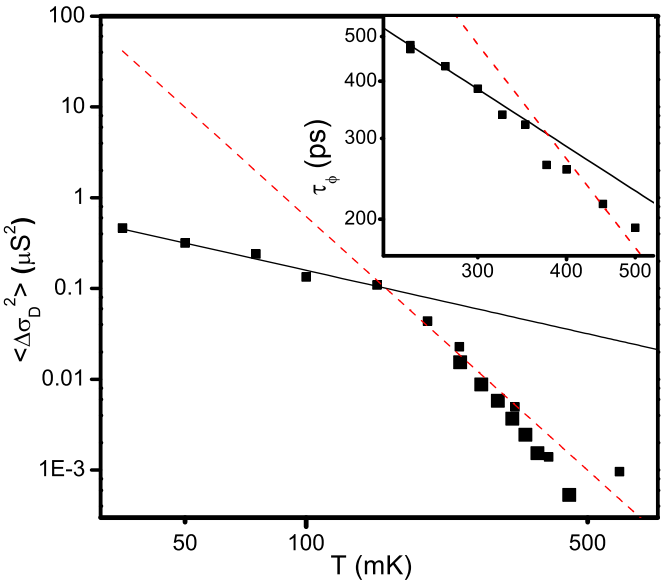

Figure 2.12: The variance of the drag conductance fluctuations (black squares) plotted as a function of T. The solid lines are plots of Eq. 2.13 using the diffusive (solid line) and ballistic (dashed) values for $\tau_\varphi(T)$. The values of $\tau_\varphi(T)$ are found from the single-layer conductance fluctuations and are shown in the inset. The single-layer concentrations are held constant, $n_{1,2} = 6 \times 10^{10}\,\mathrm{cm}^{-2}$.

In contrast to previous theoretical work done on the behaviour of the mesoscopic drag fluctuations, we observed a large enhancement of the amplitude of fluctuations by four orders of magnitude. This prompted further theoretical work by Narozhny, resulting in a ballistic theory for the drag resistance fluctuations that accounts for the large magnitude of the fluctuations by considering the important role of *local* properties of the layers. Furthermore, we observe the predicted change in T dependence of the amplitude of drag fluctuations when the character of e-e interaction crosses over from the diffusive to ballistic with increasing temperature.

In the future it would be interesting to measure mesoscopic drag in different systems, such as between 1D wires, which was considered theoretically by Mortensen *et al.* [41]. They predict that the fluctuations of the drag resistance in 1D wires can exceed the average drag resistance similar to the 2D case. However, in contrast to 2D systems, whether this results in an alternating sign of the drag depends upon the degree to which disorder in the two wires is correlated: uncorrelated disorder results in drag fluctuations with a symmetric distribution function and magnitude comparable to the mean drag allowing for fluctuations in the sign of the measured

drag resistance, whilst fully correlated disorder results in fluctuations with a highly skewed distribution function such that the fluctuations will not result in a change in the sign of the drag resistance, despite being comparable in size to the average drag [42].

Chapter 3

Fluctuations in Drag between Composite Fermions

3.1 Composite Fermions - review

In the previous chapter we discussed how the drag conductance fluctuations presented an interesting way of probing the interplay between e-e interaction and quantum interference in electronic transport. As was discussed in Section 1.3 the drag is strongly affected by the presence of magnetic fields, and so it is interesting to investigate these drag fluctuations in large magnetic fields. A particularly interesting case is when the lowest Landau level is half filled, $\nu = 1/2$. In this situation the behaviour of the strongly correlated 2DEG can be described by picturing a gas of weakly interacting composite fermion (CF) quasi-particles.

In this chapter this composite fermion model is briefly described. We show that the CFs experience only a weak effective B-field near $\nu = 1/2$, and so we may expect to observe UCF fluctuations of these quasi-particles, similar to those seen in Chapter 2. The theoretical studies of such fluctuations are covered and the main predictions given. The existing experimental evidence for these fluctuations is reviewed.

Much work has also been done theoretically and experimentally on the behaviour of the Coulomb drag near $\nu = 1/2$. Whilst the majority of this has related to the average drag resistance, the topic of mesoscopic fluctuations of the Coulomb drag between CFs has been investigated theoretically by Narozhny and Aleiner [43]. To date, such mesoscopic fluctuations of the Coulomb drag have yet to be observed

experimentally.

3.1.1 Edge States

When the Fermi energy E_F is far from the centre of a LL then there are no free extended states available for transport and so the conductivity would be expected to fall to zero. However, the sample is still able to carry a current. To explain this apparent contradiction we must refer to the existence of the so-called edge states. At the edges of the sample the energy of the Landau levels increases due to the confining potential, as shown in the left panel of Fig. 3.1. Thus, there are extended states within k_BT of the Fermi energy at the edges of the sample available for transport. These edge states through which current flows when E_F is between LLs are shown in the right panel of Fig. 3.1. Due to the spatial separation of the forwards and backwards propagating edge states, which are on opposite edges of the sample, backscattering between them is strongly suppressed. This is the explanation for the remarkably flat plateaux in ρ_{xy} and the absence of dissipation along the sample associated with current flow ($\rho_{xx} = 0$).

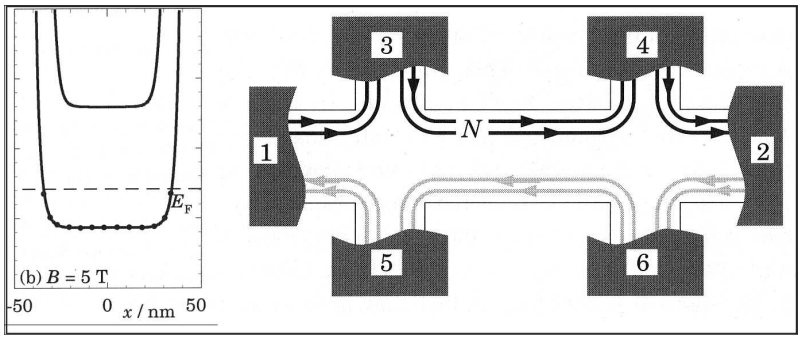

Figure 3.1: Left: the energy of Landau levels as a function of position along the width of a Hall bar. The dots represent occupied states and the dashed line is the Fermi level. Right: the arrangement of edge states in a Hall bar when the Fermi level is between Landau levels. The N denotes the presence of N edge states, two of which are depicted. The direction of the electron's drift velocity is shown by the arrows.

These edge states can be treated as 1D propagating modes with conductance e^2/h, and, as there is a suppression of scattering in these modes, each has a transmission probability of 1. A negative voltage of V_1 is applied to contact 1 in Fig. 3.1 relative to contact 2, causing a current of $(e^2/h)V_1$ to be injected into each of the N occupied edge states. N here is equal to the filling factor – the number of

LLs that are below the Fermi energy. As they are voltage probes, contacts 3 and 4 draw no net current, and so there is no voltage drop in the edge states across the top edge of the sample. Thus, the voltage drop V_{34} is zero, corresponding to the zero longitudinal resistivity observed in the IQHE. The edge states along the bottom edge are also equipotentials and are at the same potential as contact 2, such that the Hall voltage V_H measured between contacts 3 and 5 is V_1. The transverse resistivity is then $\rho_{xy} = V_H/I = h/Ne^2$. Thus we retrieve the observed quantised values observed experimentally in ρ_{xy}.

3.1.2 FQHE

In 1982 Tsui *et al.* observed new features in ρ_{xx} and ρ_{xy} at a high magnetic field corresponding to a filling factor of 1/3 [44] that resembled the IQHE: a plateau in ρ_{xy} with a value of $3h/e^2$ and a minimum in ρ_{xx}. Since then, as higher mobility samples have become available more features have been observed at fractional filling factors, as shown Fig. 3.2.

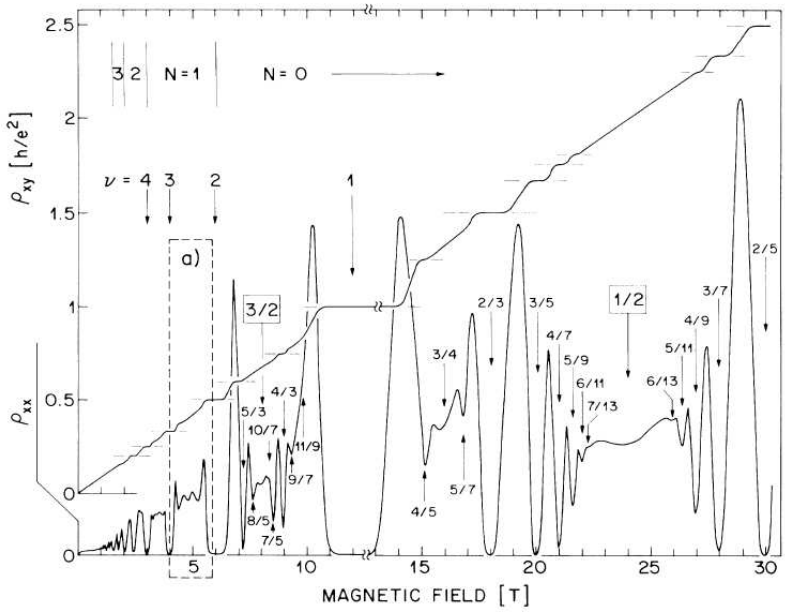

Figure 3.2: The longitudinal and Hall resistivities as a function of magnetic field for a high mobility sample at low temperatures that clearly shows the FQHE. Figure taken from [45]; $\mu = 1.3 \times 10^6\,\mathrm{cm^2V^{-1}s^{-1}}$, $n = 3.0 \times 10^{11}\,\mathrm{cm^{-2}}$, and $T = 150\,\mathrm{mK}$.

Unlike the IQHE, which arises due to energy gaps in the single-particle DOS, the FQHE is observed when the Fermi level is within a LL where there would not be any energy gap between extended states according to a single-particle physics

model, suggestive of new energy gaps arising due to many-body physics. Laughlin proposed an explanation for the observation in 1983 that involved the strongly interacting electrons condensing into a novel quantum fluid, the excitations of which are fractionally charged quasi-particles. Laughlin's proposed wavefunction to describe electrons in systems where $\nu = 1/q$ is

$$\psi_{1/q} = \prod_{i<j}^{n} (z_i - z_j)^q \exp\left(-\frac{1}{4}\sum_{k}^{n} |z_k|^2\right), \tag{3.1}$$

where q is an odd integer so as to ensure antisymmetry of the wavefunction. The $z_{i,j,k}$ represent the co-ordinates of n electrons in a complex $(x - iy)$ plane, and normalisation factors and the magnetic length have been set to unity. Each electron is coupled with q magnetic fluxes, or equivalently q vortices. Each of these vortices correspond to a zero in the wavefunction, and thus a region of depleted charge. By coupling to these regions of depleted charge the electrons reduce the Coulomb interaction energy. Increasing the magnetic field acts to induce extra, unbound vortices, which act as quasi-particle holes with fractional charge e/q. The creation of these quasi-particle excitations of the system requires a large energy cost, thus accounting for the energy gap observed in the FQHE.

Other FQHE states than the $\nu = 1/q$ fractions can be explained within the same theoretical model: $\nu = 1 - 1/q$ states by electron-hole symmetry, and the higher order p/q states (p, q are integers, where q is odd) by the so-called hierarchal model whereby fractionally charged quasi-particles themselves undergo condensations into new FQHE states.

3.1.3 Composite Fermions

The concept of composite fermions was suggested by Jain in 1989 to explain the FQHE [46] (for reviews see [47] [48]). Jain proposed that the QHE states that occur at fractional filling factor can be understood as the usual IQHE occurring between new quasi-particles that consisted of electrons bound to an even number of magnetic flux quanta. This model involving composite fermion quasi-particles successfully predicts the observed fractional ν states as well as their observed energy gaps, whereas the previous fractionally-charged quasi-particle model had been unable to account for the observed size of energy gaps. Furthermore, the absence

of a QHE at $\nu = 1/2$ is also explained where the fractionally-charged quasi-particle model had previously failed.

In the composite fermion model the large e-e interaction energy causes the system to condense into a state of composite fermions. These composite fermions are weakly interacting, and feel a greatly reduced effective magnetic field:

$$B^* = B - B_{1/2} = B - 2n\phi_0, \tag{3.2}$$

where n is the electron concentration. These weakly interacting CF particles form a Fermi sea of particles with a well-defined Fermi surface. Furthermore, as B^* is increased CFs execute semiclassical cyclotron orbits such that the Shubnikov-de Haas [49] and IQHE effects can be seen. The IQHE is seen at integer values of the composite fermion filling factor ν^*, where ν^* is related to the electron filling factor ν by

$$\nu = \frac{\nu^*}{2\nu^* \pm 1}. \tag{3.3}$$

In analysing our results at $\nu = 1/2$ it is important to relate the properties of the CF system to those of the electron system. From [50] we find that the CF resistivity ρ_{cf} can be related to ρ_{xx}, the electronic resistivity by:

$$\rho_{cf} = \rho + \rho_{cs}, \tag{3.4}$$

where ρ_{cs} is the resistivity tensor given by

$$\rho_{cs} = \frac{4\pi\hbar}{e^2} \begin{pmatrix} 0 & -1 \\ 1 & 0 \end{pmatrix}. \tag{3.5}$$

Thus, at $\nu = 1/2$ we have

$$\rho_{xx}^{cf} = \rho_{xx}, \sigma_{xx}^{cf} = 1/\rho_{xx}. \tag{3.6}$$

Taking the density of composite fermions to be the same as the density of electrons (each electron has now attached to two flux quanta and become a composite fermion, but electron number is conserved), we may use these relations to derive all other relevant transport properties of a CF system (momentum relaxation time,

diffusion coefficient, mean free path, etc.).

With respect to the drag, in the limit of weak interlayer coupling, the electronic drag resistivity ρ_D^e is the same as the composite fermion drag resistivity ρ_D^{cf} [51]:

$$\rho_D^e = \rho_D^{cf}. \tag{3.7}$$

Furthermore, the inversion relationship between the drag resistivity and conductivity can also be simplified [43]:

$$\rho_D \approx \left(\frac{2h}{e^2}\right)^2 \sigma_D. \tag{3.8}$$

3.2 UCF at $\nu = 1/2$ - existing work

Given the existence of a Fermi sea of weakly interacting particles at $\nu = 1/2$ we may expect to observe mesoscopic fluctuations at low temperatures similar to those studied in electron systems in weak magnetic fields. The behaviour of such fluctuations was studied theoretically by Fal'ko in 1994 [52]. The effective magnetic field B^* experienced by CFs is affected both by the applied magnetic field B and the carrier concentration n (Eq. 3.2). In [52], this fact is used to model local fluctuations of the carrier concentration as a weak random magnetic field. The conclusions of this study were that the UCF would show the same properties as those seen in electron systems in weak B fields, at least in the variance of the fluctuations. The quasiperiod of the fluctuations, however, is modified in CF systems due to the dependence of the effective magnetic field on both the external magnetic field and the carrier concentration. Changing the external magnetic field changes the phase difference between neighbouring electron trajectories as it does in the weak B-field case, such that the correlation magnetic field is given by $B_c L_\phi^2 = \phi_0$ as explained in section Section 2.2. However, when the gate voltage is varied the interference pattern of electron trajectories is changed in two ways: firstly, by changing the effective disorder potential seen by the electrons (this is the same mechanism as in the weak B-field case), and secondly by changing the effective random magnetic field , $\Delta B^* = 2\phi_0 \Delta n$, as can be seen from Eq. 3.2. Physically, due to the flux-attachment of $2\phi_0$ to each electron, the flux passing through a coherent area $B^* L_\varphi^2$ can be changed by ϕ_0 by a adding

half an electron to that area, $n_c L_\varphi^2 = 1/2$. Thus, it is expected that the ratio of the correlation B-field and concentration gives a constant value of $B_c/n_c = 2\phi_0$. This is quite different to the behaviour in weak magnetic fields, where the correlation concentration is $n_c = k_F l/L_\phi^2$, resulting in a ratio of $B_c/n_c = \phi_0/k_F l$ [43].

Experimentally, conductance fluctuations in the region of $\nu = 1/2$ were first seen by Simmons *et al.* in 1991 [53], although these fluctuations were not studied in depth. The first detailed study of the universal conductance fluctuations at $\nu = 1/2$ was performed in [54, 55], and was interpreted explicitly in terms of the composite fermion model. They showed by measuring both magnetoresistance fluctuations and resistance fluctuations as a function of gate voltage, that there was a constant ratio of $B_c/n_c = 2\phi_0$ between the quasi-periods in magnetic field and gate voltage, in agreement with predictions made in [52]. An unusual feature in the temperature dependence of the variance of the fluctuations was also seen, as shown in Fig. 3.3. Instead of the expected $\Delta R \propto T^{-1/2}$ dependence, a very weak T-dependence was seen below 100 mK, with a transition to a strong T^{-1} dependence at higher temperatures. This "unusual behaviour" of the CF coherence length, has not been accounted for.

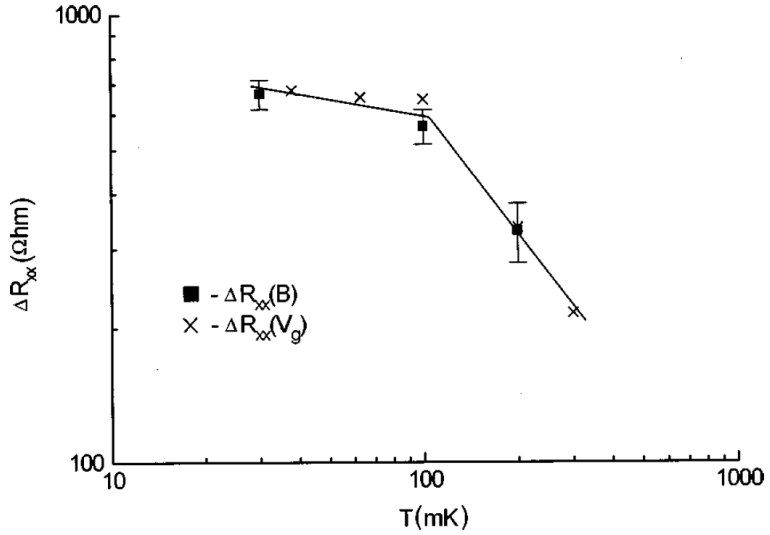

Figure 3.3: The temperature dependence of the rms amplitude of resistance fluctuations at $\nu = 1/2$. The squares are taken from magnetoresistance fluctuations, and the crosses from fluctuations as a function of gate voltage. Figure taken from [55].

3.3 Drag at $\nu = 1/2$ - existing work

In strong magnetic fields where Landau levels are formed the drag resistance has a 'twin-peak' structure in magnetic field for each LL [56]. This arises due to the competition between two factors: phase space available for scattering, and the effective strength of e-e interactions. Between Landau levels, when the Fermi energy is in localised states, there are no vacant extended states available for scattering, and so the drag is zero. As the Fermi energy moves towards the centre of a Landau level, extended states become available for scattering, the drag increases. However, at the centre of the Landau level the concentration of mobile electrons is very high resulting in strong screening of the e-e interaction, which acts to decrease the drag. The drag should go roughly as

$$\rho_D \propto g_1 g_2 |W_{12}|^2, \tag{3.9}$$

where $g_{1,2}$ are the DOS of each single-layer and W_{12} is the effective e-e interaction. An important consequence of this is a large enhancement of the drag resistivity relative to the weak magnetic field case. The DOS near the middle of a LL is approximately $g_0\sqrt{2\omega_c\tau/\pi}$, where g_0 is the 2D density of states in the absence of a magnetic field [56]. In high mobility samples this can be much greater than the DOS at $B = 0$, for instance in our samples this expression gives a value of $\sim 30 g_0$. This factor occurs to the second power in Eq. 3.9, corresponding to an enhancement of two to three orders of magnitude relative to the $B = 0$ case. These predicted features have been experimentally confirmed by Rubel *et al.* [57]; their results are shown in Fig. 3.4.

At $\nu = 1/2$ there is no such gap in the DOS as the system behaves as a sea of composite fermions in the presence of a weak effective magnetic field. The Coulomb drag at this point has been studied theoretically by several authors [51, 58, 59]. One of the predictions of these studies is that the magnitude of the drag resistance at $\nu = 1/2$ is still greatly enhanced relative to the weak B-field case, typically by three to four orders of magnitude, due to the slow diffusion of density fluctuations of CFs, compared with electrons in weak fields. Secondly, the low-temperature dependence of the CF drag is expected to go as $\rho_D \propto T^{4/3}$ [51]. It should be noted, however, that this latter prediction would result in the drag vanishing as the temperature

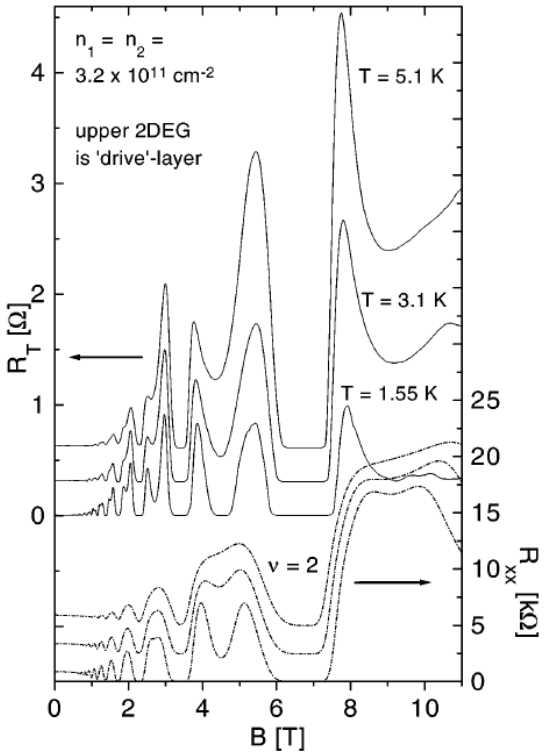

Figure 3.4: The drag resistance R_T as a function of magnetic field for three different T. The concentration of each layer is $n = 3.2 \times 10^{11}\,\mathrm{cm}^{-2}$ and the interlayer separation is $d = 30$ nm. For comparison the single-layer resistance R_{xx} is also seen, and it is clear that there is a twin-peaked structure in the drag resistance associated with each LL peak in R_{xx}. Figure taken from [57].

is decreased to zero, although later theoretical studies [60] and experiments [61] suggest that this may not be the case. From [51] the average drag resistivity at $\nu = 1/2$ is approximately

$$\rho_D = 0.825 \frac{h}{e^2} \left(\frac{T}{T_0} \right)^{4/3}, \tag{3.10}$$

where

$$T_0 = \frac{4\pi e^2 n d}{4\epsilon} (1 + \alpha). \tag{3.11}$$

Here α is the ratio of the Thomas-Fermi screening length to the interlayer separation and is given by $\alpha^{-1} \equiv (2\pi e^2 d/\epsilon)(\mathrm{d}n/\mathrm{d}\mu)$, where ϵ is the dielectric constant.

The first measurements of the drag resistance at $\nu = 1/2$ were performed by Lilly *et al.* [61]. The expected enhancement of the drag relative to that in weak magnetic fields was indeed seen, with $\rho_D(\nu = 1/2) \sim 10^3 \rho_D(B = 0)$, as shown in Fig. 3.5. Additionally, they observed the drag resistivity to vary with temperature as $\rho_D \propto T^{4/3}$ in agreement with [51]. However, at low temperatures the drag was seen to increase with decreasing temperatures. Furthermore, there was some quantitative disagreement in the magnitude of the drag measured in [61] with that

predicted in [51]: the observed magnitude being significantly larger.

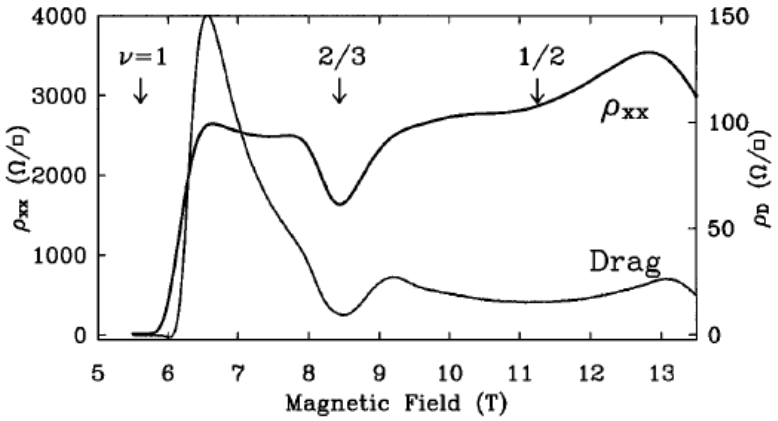

Figure 3.5: The drag resistivity ρ_D and single-layer resistivity ρ_{xx} as a function of magnetic field; $T = 0.6$ K. Figure taken from [61].

The question of whether mesoscopic fluctuations of the drag resistance could be observed in composite fermion systems was addressed by Narozhny *et al.* in 2001 [43]. They found that, similar to the drag fluctuations in weak fields, the mesoscopic fluctuations of the composite fermion drag resistivity exceeds the average drag resistivity at low temperatures, resulting in random changes of the sign of the drag resistivity with changing magnetic field and carrier density. The magnitude of the drag resistivity is also predicted to be enhanced by two to three orders of magnitude relative to the weak-field case, and is given by

$$\langle \rho_D^2 \rangle = 0.23 \frac{h^2}{e^4} \frac{1}{g_{cf}^4 (\kappa d)^2} \left(\frac{L_\phi^{cf}}{L} \right)^2 , \tag{3.12}$$

where $g_{cf} = \sigma_{cf}(h/e^2)$ is the dimensionless composite fermion conductance.

3.4 Average drag behaviour

Initially a concentration of $n_{1,2} = 5.7 \times 10^{10}\,\mathrm{cm}^{-2}$ in each layer was chosen so as to be consistent with the weak magnetic field measurements in Chapter 2. At high temperatures ($T = 5.6$ K) mesoscopic fluctuations are not seen in either the single-layer or drag resistivities, as shown in Fig. 3.6. Note that here ρ_D is plotted in Ohms, in contrast to Fig. 2.7 for the case of zero magnetic field where units are mOhms, reflecting the large enhancement of the drag resistivity at high magnetic fields – of about three orders of magnitude.

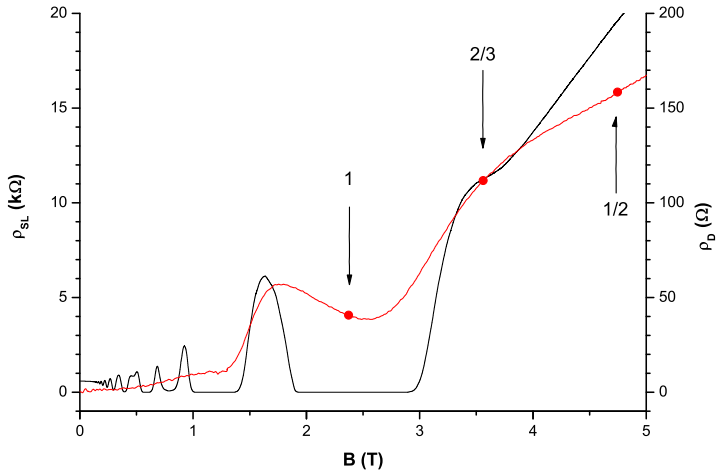

Figure 3.6: A comparison of the drag (red) and single-layer (black) resistivities as a function of magnetic field; $T = 5.6$ K, $n_{1,2} = 5.6 \times 10^{10}\,\mathrm{cm}^{-2}$. The labels show the values of the filling factor; $\nu = 1, 2/3, 1/2$ are shown.

Figure 3.7 shows how the drag resistance as a function of magnetic field goes from a smooth dependence at high temperatures to one where mesoscopic fluctuations dominate the resistivity such that there is a random sign change in the drag resistance, similar to that seen in weak B-fields, Section 2.6. This is in agreement with the prediction made in [43] that the drag resistivity fluctuations could exceed the average background drag resistivity at sufficiently low temperatures, resulting in alternating negative and positive drag. At the higher temperatures the magnitude and temperature dependence of the average drag resistivity in our experiment is in reasonable agreement with that theoretically derived in [51]. The inset of Fig. 3.7 shows the temperature dependence of the drag resistivity at a fixed filling factor near $\nu = 1/2$, the precise value corresponds to the dotted vertical line in the main figure.

The solid line in the inset is the expected drag resistance calculated using Eq. 3.10 with a value of $T_0 = 330\,\mathrm{K}$. The deviation from this fit at low temperatures is due to the drag resistance becoming dominated by the size of mesoscopic fluctuations, as can be seen by the emergence of a peak at the value of ν indicated by the dotted line in main figure as T decreases. The measurements performed were for fixed T and $B = 12\,\mathrm{T}$ whilst n was varied by the gate voltage of the active and passive layers simultaneously.

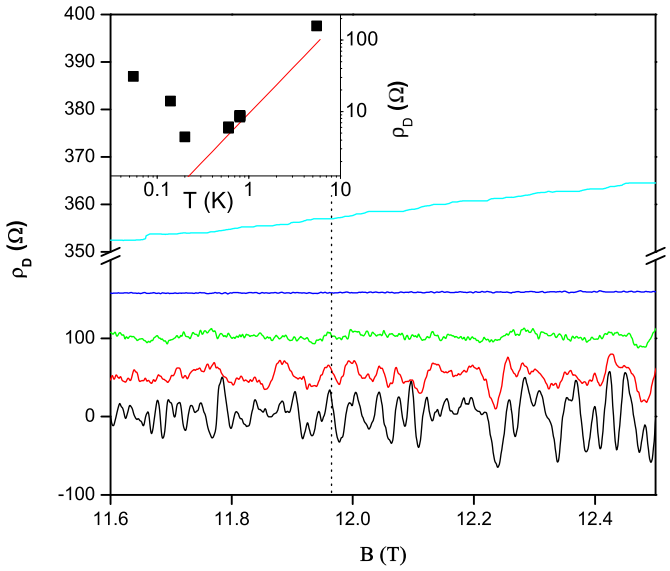

Figure 3.7: The drag resistance as a function of magnetic field, for different temperatures. $T = 0.05$, 0.14, 0.2, 0.8, 5.6 K from bottom to top; and $n_{1,2} = 1.45\times10^{11}\,\mathrm{cm}^{-2}$. The appearance of mesoscopic fluctuations is seen below 0.8 K, and dominate the drag resistance below 0.2 K. Plots are offset upwards by 50 Ohms from the lowest temperature. Inset: The drag resistivity as a function of temperature, taken at $\nu = 4.99$, as indicated by vertical dotted line in main figure. The solid line is a fit using Eq. 3.10.

After initial measurements of the fluctuating drag resistance at low temperatures a higher concentration of $n_{1,2} = 1.45 \times 10^{11}\,\mathrm{cm}^{-2}$ was chosen. The use of a higher concentration reduces the resistance of the system near $\nu = 1/2$, such that Joule heating effects on the 2DEG temperature were reduced for any given driving current. The longitudinal resistance at $\nu = 1/2$ using this concentration is 5.89 kΩ, and the other transport properties of the system are given in Table 3.4.

The enhancement of the drag in the presence of a magnetic field means that it is

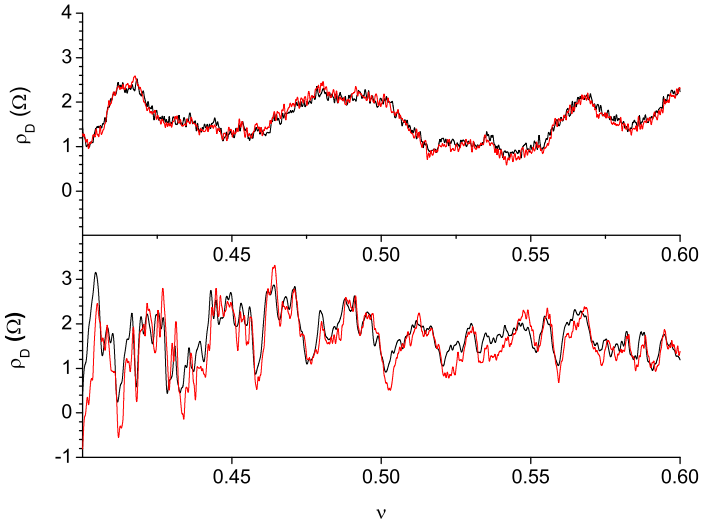

Figure 3.8: The drag resistance as a function of gate voltage for a fixed $B = 11.45\,\mathrm{T}$ and $T = 50\,\mathrm{mK}$. The top graph is for a fixed passive-layer gate voltage whilst the active-layer gate voltage is swept. The bottom graph is for fixed active-layer gate voltage whilst the passive-layer gate voltage is swept. Red and black lines are repeat measurements, demonstrating reproducibility of resistance fluctuations, which occur both as a function of active-layer and passive-layer concentration. The driving current is $I = 10\,\mathrm{nA}$.

possible to resolve the drag resistance fluctuations in the absence of Joule heating in the active-layer, which was not the case for weak B-fields. In the weak B-field case there was a large 'asymmetry' seen in the drag fluctuations as a function of active- and passive-layer gate voltages: clear fluctuations of the drag resistance were seen as the passive-layer gate voltage was swept, whilst fluctuations of the resistance as a function of the active-layer gate voltage could not be resolved above the noise. However, at $\nu = 1/2$ the drag resistance now clearly fluctuates as a function of

resistivity	ρ_{cf}	5.89 kΩ
concentration	n	$1.45 \times 10^{11}\mathrm{cm}^{-2}$
conductivity	σ_{cf}	170 μ S
dimensionless conductance	g_{cf}	4.4
mobility	μ_{cf}	$731\,\mathrm{cm}^2\mathrm{V}^{-1}\mathrm{s}^{-1}$
effective mass	m_{cf}	$4m_b$
momentum relaxation time	τ_{cf}	1.1 ps
mean free path	l_{cf}	46 nm
Diffusion coefficient	D_{cf}	$9.5\,\mathrm{cm}^2\mathrm{s}^{-1}$
'diffusivity'	l_{cf}/d	0.92

Table 3.1: Properties of composite fermions for our samples when $n_{1,2} = 1.45 \times 10^{11}\,\mathrm{cm}^{-2}$. The effective mass is taken from [50], where $m_b = 0.067m_e$ is the band mass in GaAs.

active-layer gate voltage, as shown in Fig. 3.8. There is still a difference in the amplitude of fluctuations of the drag resistivity for varying active-layer (top panel) and passive-layer (bottom panel), which is due to some heating of the active-layer occurring at the current of 10 nA used. (The fluctuations as a function of the active-layer gate voltage are smaller than the fluctuations as a function of passive-layer gate voltage.)

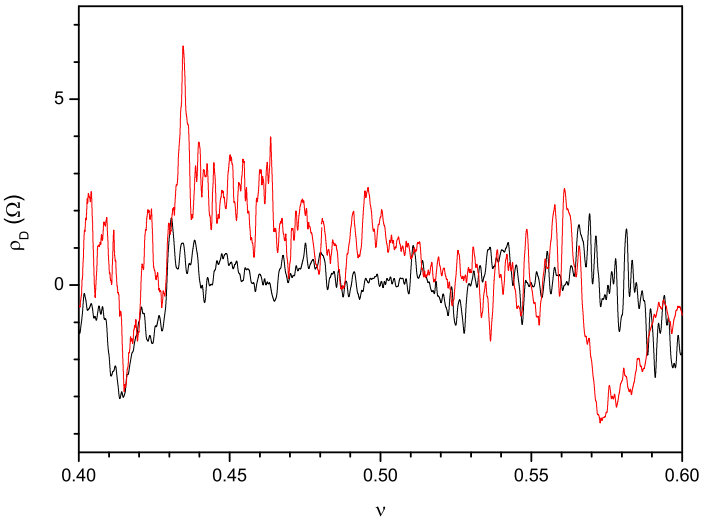

Figure 3.9: The drag resistivity as a function of filling factor for $T = 50\,\mathrm{mK}$ for varying carrier concentration and fixed magnetic field $B = 12\,\mathrm{T}$ (black) and varying B and fixed concentration $n = 1.45 \times 10^{11}\,\mathrm{cm}^{-2}$ (red). The driving current used is $I = 10\,\mathrm{nA}$.

Figure 3.9 compares the fluctuations in ρ_D for varying B-field and varying concentration. The resistivity has been plotted as a function of filling factor so that the measurements can be compared on the same graph. Indeed, due to the expected relationship between B_c and n_c for composite fermions, the typical period of the fluctuations in ρ_D as a function of ν should be the same for both graphs. Whilst the fluctuations in the two graphs are clearly different, such that the detailed structure of the drag resistance is not purely a function of filling factor, it does appear that the periods are roughly the same. The amplitudes of the two sets of fluctuations is also similar, suggesting that the fluctuations are also ergodic (Section 2.1). It is interesting to note that some of the large features in ρ_D are present in both graphs, suggesting that, rather than mesoscopic fluctuations, these features correspond to

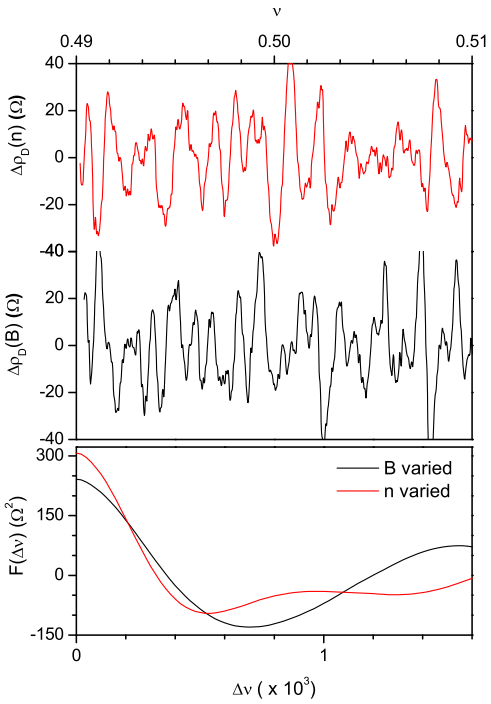

Figure 3.10: Top: The drag resistance fluctuations, after the average background has been subtracted, as a function of filling factor for $T = 50\,\mathrm{mK}$ for varying carrier concentration and fixed magnetic field $B = 12\,\mathrm{T}$ ($\Delta\rho_D(n)$, red) and varying B and fixed concentration $n = 1.45 \times 10^{11}\,\mathrm{cm}^{-2}$ ($\Delta\rho_D(B)$, black). Bottom: Comparison of ACF of the two sets of fluctuations in the top panel.

composite-fermion Landau-levels (in electronic terms, FQHE states). For this reason it is important to restrict the range of ν in measurements of the fluctuations to a narrow window in the vicinity of $\nu = 1/2$; typically, the fluctuations are measured between $0.48 < \nu < 0.52$ where there are no pronounced FQHE states observed.

In Fig. 3.10 the uppermost panel shows a zoomed in view of the fluctuations in ρ_D for changing external magnetic field (black line) and concentration (red line). The driving current used here is 0.1 nA such that the drag is nearly in the linear regime and there is no significant Joule heating (the subject of nonlinearity of the fluctuating part of the drag resistivity of composite fermions is discussed in detail later in this chapter). Here it is clear that the two periods are similar, and the therefore the ratio B_c/n_c is $2\phi_0$, in agreement with the predictions made in [52]. A comparison of the ACF of the two sets of fluctuations (bottom panel of Fig. 3.10) confirms that both the variance and quasiperiod of these fluctuations are approximately equal. It is interesting to note what the ratio B_c/n_c would be if CFs were not formed in our system. As discussed in Section 3.2, in the absence of flux attachment to electrons the correlation concentration is $n_c = k_F l/L_\phi^2$, resulting in a ratio of $B_c/n_c = \phi_0/k_F l$. For our system, where $k_F l_{cf} \approx 4.4$ (taking a concentration of $1.45 \times 10^{11}\mathrm{cm}^{-2}$ and a mean free path of composite fermions of $l_{cf} = 46$ nm), this would result in an observed ratio of 0.22 ϕ_0, in contrast to the observed ratio of $2\phi_0$.

The fluctuations of ρ_D are measured by varying the concentration of both layers simultaneously over the range of filling factor $0.49 < \nu < 0.51$ for a range of temperatures, and the variance and correlation concentration are found. The results are plotted in Fig. 3.11. The solid line is a fit using Eq. 3.12 where a prefactor of 900 has been introduced. Due to the strong dependence of the variance in Eq. 3.12 on g_{cf}, the temperature dependence of g_{cf} can be significant in describing the observed behaviour of the variance. The temperature dependence of the single-layer resistivity was not measured, although it is expected to be very weak at low temperatures where impurity scattering dominates the mobility, as has been observed in previous experiments [62].

In [62], below about 700 mK the mobility of composite fermions was dominated by impurity scattering, the mobility having a weak $T^{0.1}$ temperature dependence. The system used in that study was similar to ours, with approximately the same concentration, although the mobility was about 100 times greater. The temperature range over which the mobility is impurity-scattering dominated actually increases with decreasing mobility, so it is very likely that our system is in this temperature range. Assuming the same $T^{0.1}$ temperature dependence of impurity scattering in our system, we expect the dependence of the composite fermion dimensionless conductance to vary weakly with temperature as $g_{cf} \propto T^{0.1}$.

Clearly there is poor agreement in both the magnitude and T-dependence of the variance of Fig. 2.12 and that described by Eq. 3.12. Similar to the case of weak B-fields, this can be a result of the drag not being very far into the diffusive regime of drag (where $d \gg l_{cf}$) for which Eq. 3.12 was derived. Interestingly, the disagreement in both the magnitude and the strength of the T-dependence is less than was seen in the weak field case, which would be expected as a result of our CF system being closer to the diffusive regime of drag: for our system $d/l_{cf} = 1.1$ whereas for the weak field case $d/l \approx 0.02$.

The inset of Fig. 3.11 shows the temperature dependence of composite-fermion dephasing length L_{φ}^{cf} found from the correlation-concentration of the fluctuations. The solid line is a fit found by substituting g_{cf} into the diffusive expression for the dephasing length, Eq. 2.1 and introducing a prefactor of 1.1. This good agreement with the conventional expression for the dephasing length in the diffusive regime of e-e interaction is in contradiction with the prediction of [43] that there would

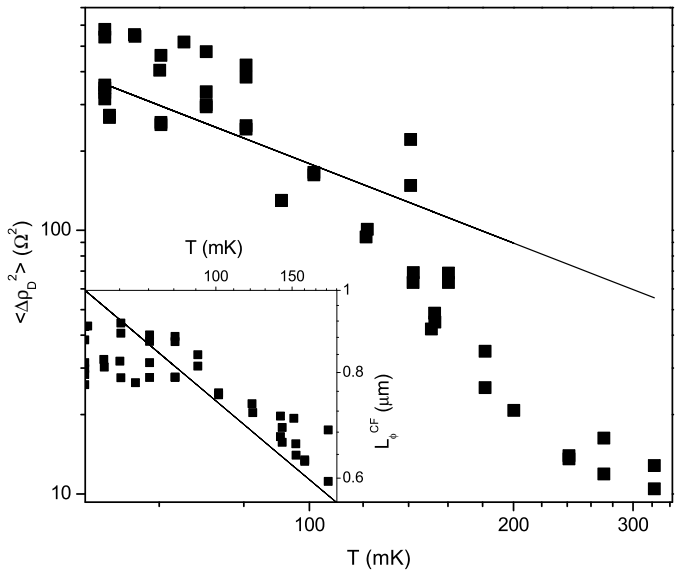

Figure 3.11: Main: The variance of drag resistivity fluctuations plotted against T; $n = 1.45 \times 10^{11}\,\mathrm{cm}^{-2}$. The solid line is a theoretical fit using Eq. 3.12 and introducing a prefactor of 900. Inset: T dependence of L_ϕ^{cf} measured directly from the correlation concentration of the drag resistivity fluctuations. Solid line is a theoretical fit using $L_\phi^{cf} = 1.1\sqrt{D\hbar g_{cf}/k_B T \ln g_{cf}}$ [31].

be a different dephasing mechanism at play. The likely reason for this is that this prediction was made for a system where $g_{cf} \gg 1$, whereas in our system $g_{cf} \sim 4$. There is some indication of a saturation in the T-dependence in both the variance and dephasing length in Fig. 2.12. This behaviour is similar to that observed in [54, 55] where single-layer CF resistance fluctuations were studied. In that study only the T-dependence of the variance was studied, but we show that in the drag the saturation occurs both in the variance and the quasiperiod of the fluctuations.

3.5 Non-linearity of Drag fluctuations

To ensure that the temperature of the 2DEG is in equilibrium with the thermometer small driving currents are used. To find the maximum safe driving current the drag resistance is measured using progressively smaller currents until there is no observed non-linearity of the measured resistance. However, as is shown in Fig. 3.12 the amplitude of the drag resistance fluctuations at $\nu = 1/2$ is strongly non-

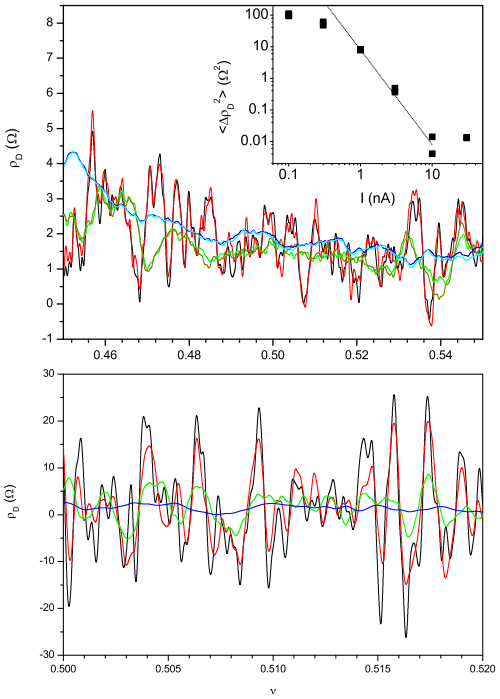

Figure 3.12: The drag resistance as a function of filling factor for $T = 50\,\mathrm{mK}$ (B varied, $T = 50$ mK and $n = 1.45 \times 10^{11}\,\mathrm{cm}^{-2}$ are held constant) for different driving currents. Top left: $I = 3$ nA (black and red), 10 nA (green and olive), and 30 nA (blue). Bottom left: 100 pA (black), 300 pA (red), 1 nA (green), and 3 nA (blue). Top right: The current dependence of the variance of the fluctuations.

linear even down to very small currents. In order to quantify the dependence of the non-linearity of the drag resistivity fluctuations, the variance is calculated and plotted as a function of driving current, as shown in the top right panel of Fig. 3.12. At the lowest currents used, $I = 100\,\mathrm{pA}$, there is some indication of a saturation in the current-dependence of the variance. Thus, this current was used to measure the fluctuations in ρ_D; lower currents were not viable due to the large time-constants required to resolve the small drag voltages above the background signal-noise.

On further investigation, however, it is found that the non-linearity of the drag resistance fluctuations is not a result of Joule heating. Figure 3.13 shows the single-layer resistance at 50 mK in the vicinity of $\nu = 1/2$ for different driving currents. Whilst there is clear heating of the system when $I = 1\,\mathrm{nA}$, below this current there is a return to the linear regime. This indicates that the non-linearity in the drag-resistance fluctuations has a less trivial origin than conventional Joule heating. Furthermore, the inset of Fig. 3.13 shows that the drag resistivity is in the linear regime in the vicinity of $\nu = 1/2$ for driving currents as high as 10 nA when $T = 800\,\mathrm{mK}$. It is interesting that at this high temperature the drag varies smoothly with filling factor, reflecting the negligible role of mesoscopic fluctuations; this is suggestive of the fact that it is only the fluctuations of the drag resistivity that are nonlinear, whilst the average drag resistivity is independent of driving current.

This non-linearity of the drag resistivity is similar to that observed in [61] where the drag resistivity was linear at high T, but became nonlinear at lower temperatures. In that study the drag resistivity was also reported to have returned to the linear regime at sufficiently low currents (< 0.5 nA for their system), in agreement with the behaviour in Fig. 3.12. Mesoscopic drag effects were not investigated in that study and the nonlinearity was interpreted as the behaviour of the average drag resistivity, though no explanation for this behaviour could be provided.

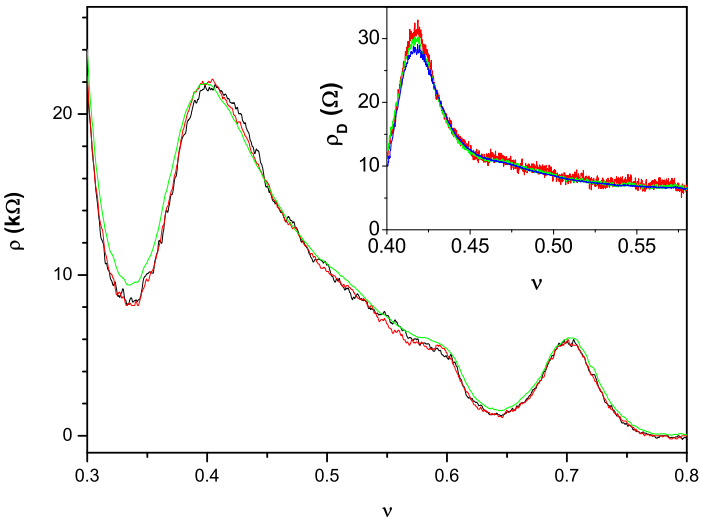

Figure 3.13: The single-layer resistivity as a function of filling factor (n varied, $B = 6$ T) for different currents $I =$ 0.1 nA (black), 0.3 nA (red), and 1 nA (green); $T = 50$ mK. Joule heating is absent below 0.3 nA. Inset: Drag resistivity versus filling factor (n swept, $B = 12$ T held constat) for different driving currents; $T =$ 800 mK.

3.6 Conclusion and Further Work

Fluctuations of the Coulomb drag resistance have been observed for the first time, and a detailed study made of their behaviour. The ratio of the correlation magnetic field to the correlation concentration was found to be $2\phi_0$ in agreement with theoretical predictions for a composite fermion system. The magnitude of the drag was seen to be enhanced by three orders of magnitude, for both the average drag resistance, as has been previously observed by other groups, and also for the fluctuations of the drag resistance, as had been predicted in recent theoretical studies. The dependence

of the amplitude of the fluctuations as a function of temperature has been measured and shown to vary as $\rho_D \propto T^{-3}$, which is a much stronger dependence than has previously been predicted. Furthermore, from the correlation length in both magnetic field and concentration, the dephasing length has been found as a function of temperature. The dependence has been shown to be well described by conventional diffusive theory for electron dephasing lengths, contrary to that predicted theoretically for a bilayer system, although this can be due to the dimensionless conductance of our system being small to the $g \gg 1$ domain discussed in theory.

There are many interesting extensions to the work performed in this chapter. For instance, the resistance fluctuations are expected to depend on the conductance of the CF system, and it would be interesting to observe whether the quasiperiod would also agree with conventional diffusive behaviour of dephasing, and how the magnitude of the fluctuations would be affected by the conductance of each layer. In previous experimental and theoretical studies of the average Coulomb drag between composite fermions it was found that the drag is sensitive to layer density imbalance, and it would be interesting to study whether this is also the case for the drag resistance fluctuations. Another interesting extension to this work would be to measure the fluctuations at regions of filling factor other than near $\nu = 1/2$.

Chapter 4

Transport properties of graphene in strong magnetic fields

4.1 Introduction

Graphene is the name given to the mono-layers of carbon atoms that when stacked constitute bulk graphite. The first example of a single-layer graphene sample was produced in 2004 [63] and since then much excitement has been generated by this novel material due to its unusual properties. These are its gapless linear dispersion relation that results in the charge carriers behaving as massless Dirac particles, and the chirality of these particles: there is an extra quantum number (pseudospin) for carriers in graphene due to the presence of two non-equivalent sub-lattices of carbon atoms that make up a graphene sheet.

In this chapter details are given describing the graphene sample used in our measurements, along with some description of the operation of this sample. Then the physics of electron transport in graphene is briefly described, such as the effects of the linear density of states, and the existence of an anomalous quantum Hall effect that occurs at half-integer values of filling the factor. Previous experimental observations of these effects are given.

Following this the behaviour of UCF in the QHE regime is given for conventional 2D systems, which is greatly modified depending on whether the Fermi level lies within the centre of a Landau level or within its tails.

The experimental section of this chapter first covers the characterisation of

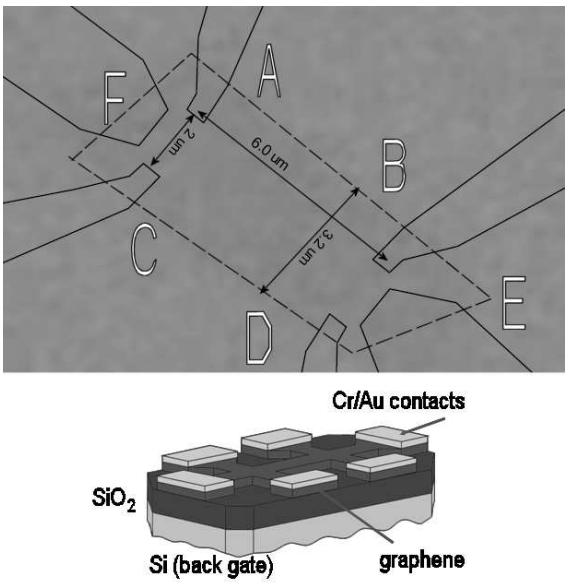

Figure 4.1: Upper figure: Optical image of graphene sample G13DC3 with contacts, labels, and dimensions overlaid. The dashed line indicates the boundary of the mono-layer graphene flake. Lower figure: profile diagram of the sample – graphene flake is deposited on top of an insulating layer of silicon dioxide that covers the n^+ silicon substrate. By applying a voltage between the silicon layer and graphene flake the silicon layer acts as a gate, allowing the carrier concentration in the graphene flake to be controlled.

our samples, including measurements of the resistivity as a function of carrier-concentration, and determination of the mobility from these results.

We then present measurements of the quantum lifetime τ_q as a function of carrier concentration and temperature, which to the best of our knowledge has not been investigated elsewhere.

The results of measurements of the conductance fluctuations around different regions of the integer-filling-factor LLs are then presented as a function of magnetic field and carrier concentration. From these measurements we find the coherence diffusion lengths and times, and describe their behaviour as a function of temperature. Comparison is made between our results of high B-field fluctuations in graphene and the theories that have been successfully applied for similar investigations in GaAs systems.

4.2 Sample description

The samples used are of a Hall-bar geometry, as shown in Fig. 4.1, and have six contacts, allowing for four-terminal resistance measurements and Hall-voltage measurements. It was found that contact F was non-conducting, so four-terminal resistance measurements were made using contact A as a source, contact E as a drain, and contacts C, D, and B as voltage probes for the longitudinal resistance

measurements ($\rho_{xx} \equiv \rho_{CD}$) and Hall resistance measurements ($\rho_{xy} \equiv \rho_{BD}$). At some point contact C ceased to conduct, and so the measurements of conductance fluctuations are performed using a different circuit: contacts A and D are used as the source and drain, respectively, whilst the longitudinal resistance is measured using contacts B and E as voltage probes. Thus, for characterisation measurements, including measurements of τ_q, the aspect ratio is $L/W = 6.5/3.2 = 2.0$, whilst for conductance measurements the aspect ratio is $0.9/3.2 \approx 0.3$.

The profile of the sample is shown in lower part of Fig. 4.1. The graphene flake in the upper part of the figure is deposited on a layer of insulating silicon dioxide that covers a substrate of n-doped silicon. The silicon layer is used as a back-gate by applying a DC voltage between it and the graphene flake, allowing for gate voltage control of the carrier concentration. The relationship between the applied gate voltage and the induced carrier density in the graphene sheet is determined by the capacitance per unit area between the gate and graphene, and so depends upon the SiO_2 thickness. The samples used in all measurements have a dielectric thickness of 300 nm, which results in a dependence of carrier density on gate voltage as follows:

$$n = 7.2 \times 10^{10}\,\mathrm{cm}^{-2}(V_G - V_{cn}), \tag{4.1}$$

where V_{cn} is the charge-neutrality point in gate voltage, i.e. the gate voltage at which there is a maximum in the longitudinal resistivity and the carrier density is zero.

4.3 Graphene physics

The main distinguishing feature of graphene is its linear dispersion relation and the absence of an energy band-gap (for a review, see [64]). The hexagonal arrangement of carbon atoms in a graphene sheet is treated theoretically as two triangular sub-lattices, which we can label as A and B, as shown in Fig. 4.2. The energy spectrum calculated for this system in the tight-binding model is shown in Fig. 4.3. The points where the energy bands in Fig. 4.3 cross are the so-called Dirac points. They correspond to the K and K' points in the Brillouin zone shown in Fig. 4.2.

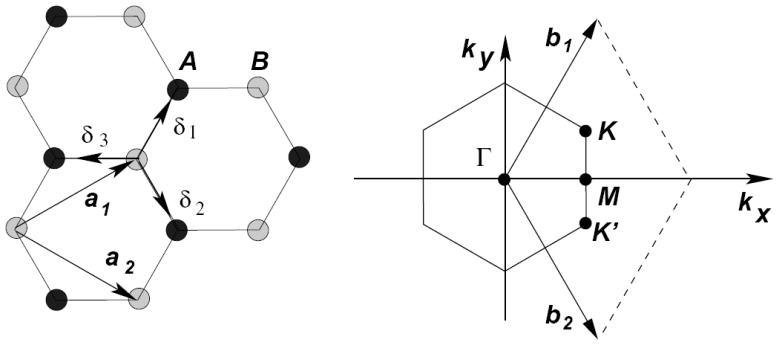

Figure 4.2: Left: the lattice structure of graphene, formed of two sub-lattices, A and B. The lattice unit vectors are a_1 and a_2, whilst δ_i are the nearest neighbour vectors. Right: the Brillouin zone, where K and K' denote the Dirac points, and b_1 and b_2 are the reciprocal lattice vectors. Figure taken from [64].

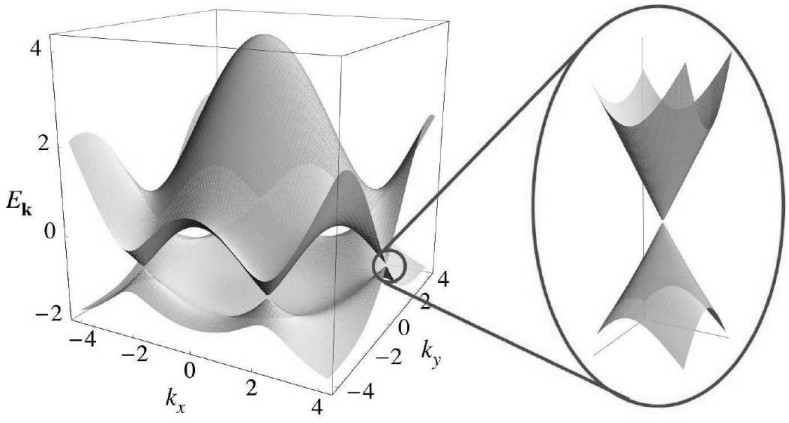

Figure 4.3: Energy spectrum with a zoomed-in view of energy bands around a Dirac point. The energies are plotted in units of 2.7 eV, the nearest-neighbour hopping energy. Figure taken from [64].

The energy near these Dirac points has been shown to increase linearly with wave-vector k [65]:

$$E = \hbar v_F k + \mathcal{O}((k/K)^2), \tag{4.2}$$

where $v_F \approx 10^6\,\mathrm{m/s}$ is the Fermi velocity and the $\mathcal{O}$ function refers to higher-order terms in k/K. Note that this expression is only valid for wave-vectors that are close to the Dirac point relative to the size of the Brillouin zone: $k \ll K$. The energy spectrum differs from that seen in more conventional semiconductor systems by the fact that the Fermi velocity is independent of carrier concentration. Furthermore,

applying the definition of the transport effective mass, $(m^*)^{-1} = (d^2E/dk^2)/\hbar^2$ to Eq. 4.2 gives the non-physical result of an infinite effective mass. The reason being that this definition is only applicable near extrema of the bands where $dE/dk = 0$. The correct statement is that the transport mass is zero, as the dispersion relation is similar to that of a photon. However, the concept of the cyclotron mass is still applicable for electrons in graphene, as it describes orbital motion around the Fermi circle, which has a conventional form. The cyclotron mass is defined as

$$m_c = \frac{\hbar^2}{2\pi}\left[\frac{\partial A(E)}{\partial E}\right]_{E=E_F} = \frac{E_F}{v_F^2}, \tag{4.3}$$

where $A(E) = \pi k(E)^2 = \pi(E/v_F)^2$ is the area in k-space enclosed by an electron orbit with energy E. The dependence of the cyclotron mass on Fermi energy means that it will vary as the square root of concentration: $m_c \propto \sqrt{n}$, as has been observed experimentally by several groups [63, 66].

The DOS in graphene is linear in energy [63]:

$$\varrho(E) = \frac{g_s g_v m_c}{2\pi\hbar^2} = \frac{g_s g_v}{2\pi\hbar^2}\frac{|E|}{v_F^2}, \tag{4.4}$$

where g_s, g_v are the spin and valley degeneracy, respectively. The valley degeneracy $g_v = 2$ occurs due to the two non-equivalent valleys in the Brillouin zone at K and K' in Fig. 4.2. Using this expression we can derive the relationship between carrier concentration and Fermi energy:

$$n(E_F) = \int_0^{E_F} \varrho(E)dE = \frac{g_s g_v E_F^2}{4\pi\hbar^2 v_F^2}. \tag{4.5}$$

The existence of a minimum non-zero value of the conductivity at the zero-energy point is an intriguing feature of graphene [63]. The so-called Dirac point is the energy where the conduction band meets the valence band and the carrier concentration is zero, as depicted in Fig. 4.4. Given the absence of free charge carriers it would be reasonable to expect that the low-temperature resistance would diverge. However, contrary to this expectation not only has no such divergence been observed, it appears that there is a minimum value that the conductivity takes at the Dirac point, close to $4e^2/h$ [63]. There is an ongoing debate on how universal the minimum conductivity value is. However, since this experiment it has been

suggested that at the Dirac point "puddles" of electrons and holes exist due to disorder that can play an important role [67].

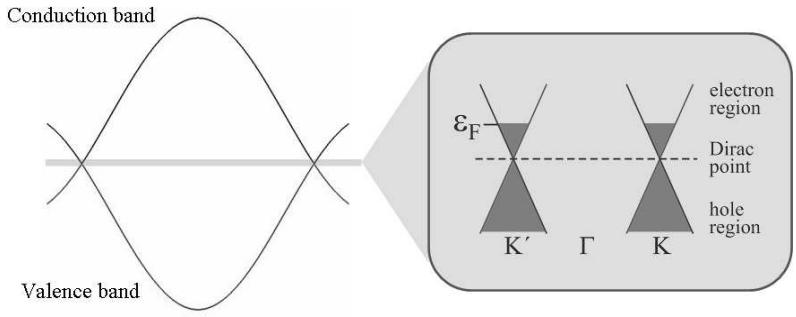

Figure 4.4: Energy bands in graphene – a cross-section of $E(k_x)$ in Fig. 4.3 near the K and K' crossing points. The shaded strip is zoomed-in to show that the dispersion relation is linear for energies near the Dirac point. Depending upon the position of the Fermi level relative to the Dirac point, charge-carriers excitations are electron-like or hole-like.

4.4 Anomalous Hall effect

The QHE effect in graphene is unusual in that the plateaux in ρ_{xy} and the minima in ρ_{xx} occur at half-integer values of the filling factor $\nu = nh/4eB$. The first observation of this effect is reproduced in Fig. 4.5. It is interesting to note that even the addition of a single layer of graphene will change the QHE, which will still different from the conventional QHE: the inset of Fig. 4.5 shows the Hall conductivity of a bi-layer graphene sample where the conventional quantised value of conductance occur at integer filling factor. For this reason the anomalous QHE is an important transport measurement for determining if a graphene sample is indeed a single mono-layer.

This effect was predicted theoretically [69,70], and can be explained qualitatively by referring to the expression for the energy spectrum of Dirac fermions in quantising magnetic fields [71]:

$$E_N = \sqrt{2e\hbar v_F^2 B(N + 1/2 \pm 1/2)}, \tag{4.6}$$

where $N = 0, 1, 2\ldots$ is the LL index and the $\pm 1/2$ is for different pseudospin projections. This expression predicts a LL to occur at zero energy, and to have half the degeneracy due to only one pseudospin $(-1/2)$ being allowed for this energy.

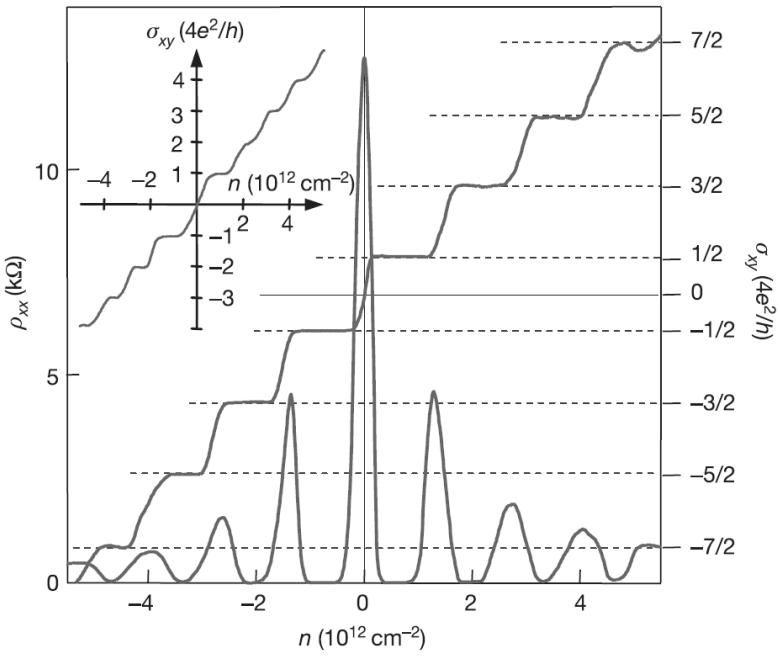

Figure 4.5: The Hall conductivity and longitudinal resistivity as a function of concentration in graphene for B =14 T and T = 4K. Inset: the Hall conductivity in bi-layer graphene, demonstrating the conventional quantisation, but with the first step occurring at $n = 0$ unlike in usual 2D systems. Figure taken from [68].

An alternative picture is that the lowest LL is occupied by both electron and holes due to the absence of a band gap. As a result, the first QH plateau occurs at half the usual $\nu = 1$ filling factor. Equation 4.6 also reveals quite a different energy spectrum of the Dirac fermions in quantising magnetic fields: the LLs are no longer spaced equally in energy as shown in Fig. 4.6.

4.5 The Shubnikov-de Haas effect in graphene

The behaviour of the SdH oscillations in graphene has been studied by Gusynin *et al.* [71] and has been shown that

$$\Delta\sigma_{xx} = \frac{4e^2|E_F|\Gamma(E_F^2+\Gamma^2)}{(\pi\hbar v_F^2 eB)^2+(2E_F\Gamma)^2}\sum_{k=1}^{\infty}\cos\left(\frac{\pi k(E_F^2-\Gamma^2)}{\hbar v_F^2 eB}\right)R_T(k,E_F)R_D(k,E_F), \tag{4.7}$$

where k is the harmonic number, and the "temperature amplitude" factor is

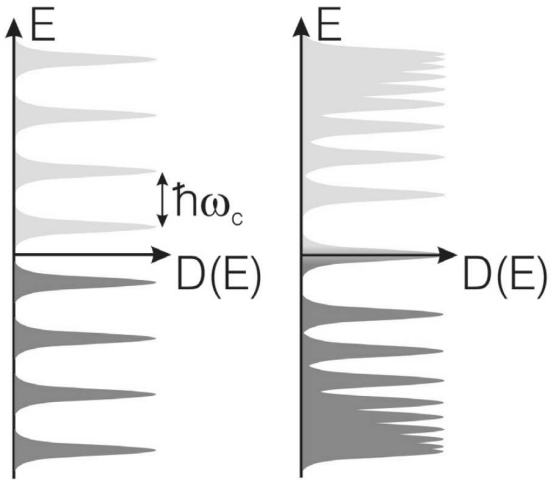

Figure 4.6: The Landau levels for normal electrons (left) and Dirac fermions (right). Figure taken from [72].

$$R_T(k, E_F) = \frac{t_k}{\sinh t_k}, t_k = \frac{2\pi^2 k k_B T E_F}{\hbar v_F^2 e B}, \tag{4.8}$$

while the Dingle factor is

$$R_D(k, E_F) = \exp\left(-\frac{2\pi k |E_F| \Gamma}{\hbar v_F^2 e B}\right). \tag{4.9}$$

Here $\Gamma = \hbar/2\tau_q$ is the energy half-width of the LLs. The behaviour of $\rho_{xx}(B)$ can then be found using the usual tensor inversion relationship between the resistivity and conductivity in magnetic fields. Immediately we see that there will still be oscillations in $\rho_{xx}(B)$, and that these oscillations will be periodic in $1/B$ in the same way as for conventional 2D systems. Note, however, the two interesting differences of the SdH effect in graphene compared to conventional structures: because of the energy-dependent cyclotron mass, the carrier concentration now enters into the temperature amplitude and Dingle factors, $R_T(k, E_F)$ and $R_D(k, E_F)$, and secondly that there is a phase shift of π in the oscillating cosine factor. Prior to [71], it had already been observed [66, 68] that the exponential envelope of the amplitude of SdH oscillations is well described by the conventional expression given in Eq. 1.3, provided that instead of the effective mass m^* the cyclotron mass is used, $m_c = E_F/v_F^2$, and a phase shift of π is included in the cosine factor (compare with Eq. 1.6). Taking these modifications into account we obtain for the oscillating part of the magnetoresistivity in graphene (neglecting the B-dependence of the first term when $\Gamma > \hbar\omega_c$):

$$\frac{\Delta\rho_{xx}}{\rho_0} \propto \exp\left(-\frac{\pi|E_F|}{eBv_F^2\tau_q}\right)\frac{2\pi^2 k_B T|E_F|/\hbar eBv_F^2}{\sinh(2\pi^2 k_B T|E_F|/\hbar eBv_F^2)}\cos\left(\frac{\pi E_F^2}{\hbar eBv_F^2}\right). \tag{4.10}$$

4.6 Conductance fluctuations in strong magnetic fields

In chapter 2 the existence of conductance fluctuations that resulted from quantum interference of electron wave-functions was discussed. However, the description there was limited to the case of weak fields, $\omega_c\tau \ll 1$. As the magnetic field is increased beyond this limit the behaviour of the conductance fluctuations is strongly modified, and much work has been done both in theory and experiments on this topic. In intermediate field strengths, and at the centre of LLs at any field, the weak-field UCF theory can be modified to describe the fluctuations. In strong fields fluctuations can occur on the "flanks" of LL resistance peaks, i.e., in regions of B where edge states play a dominant role in transport. The fluctuations in this case arise from tunnelling between edge states and the extended-states in the bulk and have a different nature compared with UCF.

4.6.1 The case of modified diffusion

The effect of a strong magnetic field on the conventional UCF theory was first studied by Xiong and Stone (XS) [40]. The effect of the magnetic field is to change the diffusion coefficient such that it becomes magnetic field dependent, $D(B)$. This field-dependent diffusion coefficient can be represented as

$$D(B) = \frac{l_0^2}{2\tau_0}, \tag{4.11}$$

where l_0 and τ_0 are some characteristic length and times. In the limit of weak fields these simply become the mean free path l and the elastic momentum scattering time τ [40]. In the case of strong fields they have the following dependencies: $l_0^2 = 2r_c^2$, where $r_c = v_F/\omega_c$ is the cyclotron radius, and $\tau_0^2 = \pi m^*\tau/2eB$ [73]. (In graphene these quantities can become $l_0 = l_B^2\sqrt{2\pi n}$ and $\tau_0^2 = \pi E_F\tau/2eBv_F^2$, using Eq. 4.3 for the cyclotron mass.) In the XS theory, the variance was found to be independent

of magnetic field, such that the weak-field universal value of $(e^2/h)^2$ was retained, whilst the correlation magnetic field becomes magnetic field dependent. The latter occurs due to the field dependence of the diffusion coefficient, as τ_ϕ is assumed field-independent. Depending upon the value of L_ϕ relative to the sample length and width they found [40]:

$$B_c = \begin{cases} B^{3/4}, & \text{for 1D case: } W < L_\phi < L, \\ B^{3/2}, & \text{for 2D case: } W, L < L_\phi. \end{cases} \tag{4.12}$$

The predicted B-field dependence has been observed in several experiments, for example [74–76]. However, the behaviour of the variance has variously been seen to increase, decrease, or remain constant with increasing B-field. Some attempt to explain the observed behaviour qualitatively was made in [76] by considering the effect of edge state transport on the variance.

The behaviour of the fluctuations produced by the edge states was considered theoretically by Maslov and Loss (ML) [77]. The system they studied is depicted in Fig. 4.7. In their model the motion of new quasiparticles is considered, which are the centres of the cyclotron orbits that the real electrons are executing. The ML theory considers the fact that as the Fermi level E_F moves away from the energy E_N of the centre of a Landau level the edge states begin to play an important role. The energy band over which extended states exist at the centre of the LL is $\hbar/\tau_0$. As long as the Fermi level lies inside this band, i.e., $|E_F - E_N| < \hbar/\tau_0$, then the electrons can either travel diffusively through the sample via the extended states in the bulk, or can collide with a sample edge and then travel along the boundary with very little scattering (scattering is suppressed in edge states, as discussed in Section 3.1.1). Increasing $|E_F - E_N|$ corresponds to diffusive motion through the bulk, with some chance of becoming "trapped" in an edge state, in which case the quasiparticle then slides along the edge of the sample. This sliding motion is included via a sliding diffusion coefficient:

$$D_s = \frac{\Delta l_s l_0}{\pi \tau_0}, \tag{4.13}$$

where a sliding mean free path has been defined as $l_s = \Delta l_s + l_0$. The effect of these sliding trajectories is to decrease the variance as the sliding quasiparticles leave the

sample faster than those travelling diffusively through the bulk.

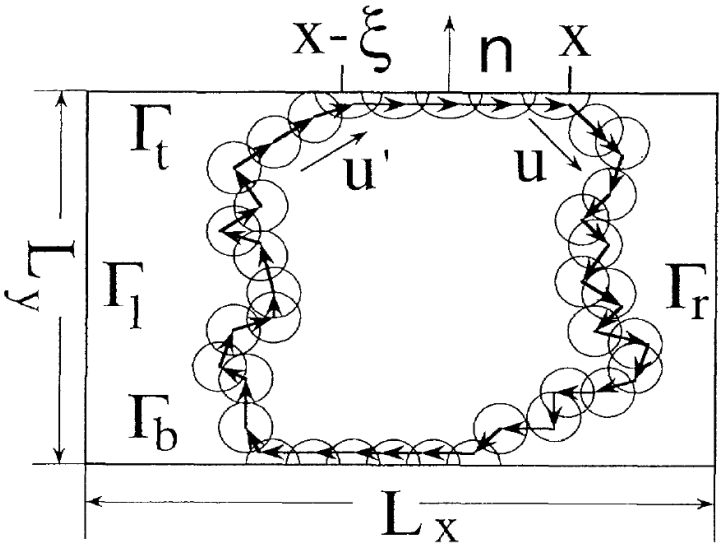

Figure 4.7: A disordered 2D conductor in a strong magnetic field, which was the model used in [77]. The circles represent the cyclotron orbits of real electrons, whilst the arrows represent the motion of the quasiparticles - the centres of the cyclotron-orbits.

As the Fermi level moves towards the flanks of the LL, Δl_s increases and so we would expect a monotonic decrease of the variance as we move away from the LL centre. However, in [77] the variance was not found to decrease monotonically with increasing $|E_F - E_N|$. At certain values of Δl_s it is possible for quasiparticles to become localised in a looped trajectory like the one shown in Fig. 4.7. These trajectories lead to resonances in the variance. Thus, the variance is expected to have a local minimum when E_F is in the centre of the LL, and then the variance increases to a maximum as E_F moves away from the centre, before decreasing and then finally vanishing as E_F leaves the energy band of extended states; this behaviour is shown in Fig. 4.8.

The final result obtained in [77] for the variance is

$$\langle \delta g^2 \rangle = \sum_q \frac{(4\alpha|\bar{q}|L_y/\tilde{\lambda})^2}{\sin^2 \alpha q L_y + \gamma^2} + \frac{(2L_{in}/L_x)^3}{\sqrt{1+\alpha^2}}. \tag{4.14}$$

Here $g = G/(e^2/h)$ is the dimensionless conductance, $\alpha = 2\Delta l_s/\pi l$, $\bar{q} = q - i/L^s_{in}$, L^s_{in} is the inelastic mean free path in the edge states, $q = 2\pi k/L_x$, $\gamma = \alpha L_y/L^s_{in} \ll 1$, and L_{in} is the inelastic mean free path.

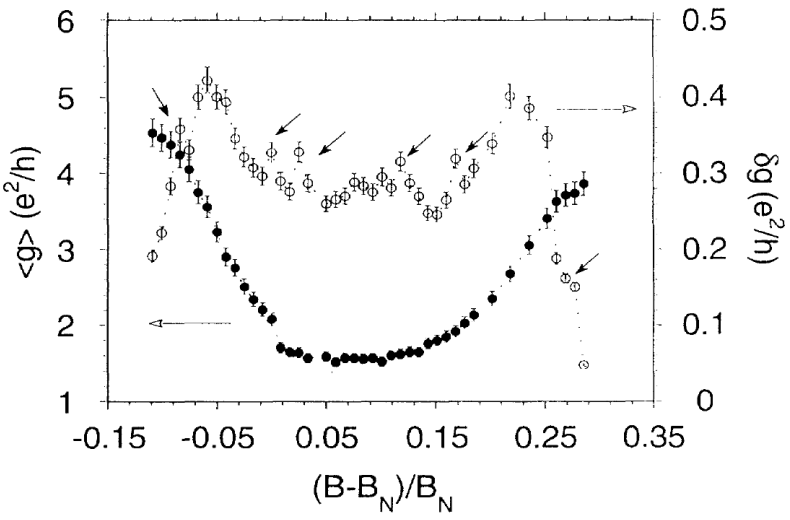

Figure 4.8: Numerical calculations of [77] for the average conductance (solid circles) and amplitude of conductance fluctuations (open circles) for the $\nu = 2.5$ Landau level. B_N is the magnetic field at $\nu = 2.5$.

With the exception of the resonances, this behaviour of the variance was also obtained (without reference to edge states) in [78], who found the variance to go as

$$\langle \delta g^2 \rangle \approx (1+\gamma^2)^{-1/2} \left(\frac{L_T}{L} \right)^3, \tag{4.15}$$

where $\gamma = \sigma_{xy}/\sigma_{xx}$. In addition to the results of [77], they also predict the correlation magnetic field behaviour to be directly related to the value of ρ_{xx}:

$$B_c = \frac{\phi_0}{(1+\gamma^2)L_T^2} \approx e\varrho(E_F)k_B T \rho_{xx}, \tag{4.16}$$

where $\phi_0 = h/e$ is the flux quantum and $\varrho(E_F)$ is the density of states in the Landau level. Both of the above expression are valid provided that $L_T > (1+\gamma^2)^{1/2}W$. Experimental observation of the predicted similarity in the shape of B_c and ρ_{xx} has been reported in [79] where they observed oscillations in B_c that were in-phase with the SdH oscillations of ρ_{xx}.

4.6.2 The case of tunnelling

Attempting to apply the modified UCF theory in strong B-fields is reasonable near the centre of peaks in ρ_{xx} where edge states make a small correction to the diffusive motion of electrons through the states in the bulk. However, when the Fermi level

is far into the tails of the resistivity peaks, transport is dominated by electrons in the edge states. In this regime fluctuations can occur by a process that is entirely different from the usual UCF interference mechanism.

In Section 3.1.1 it was noted that scattering is suppressed in the IQHE where transport was via edge states. However, scattering between edge states can occur, which results in fluctuations in the resistance. This scattering is either between edge states that propagate in the same direction (intra-edge scattering) and between counter-propagating edge states (inter-edge scattering).

Given the large spatial separation between counter-propagating edge states – they are located at opposite sides of the sample – it might be expected that such tunnelling events are rare and would not be resolved in experiment. However, inter-edge tunnelling can be mediated via localised states that exist in the bulk of the sample, which makes this process more probable. These localised states arise due to disorder causing spatial fluctuations in the Landau levels. If the Fermi level is in the tail of the LL, then potential 'hills' and 'valleys' can be occupied, as shown in Fig. 4.9. The island regions of Fig. 4.9 have localised edge states that travel around the perimeter of the island. The resulting closed orbits have discrete energies that depend on the magnetic field as the Bohr-Sommerfeld condition requires that an integer number of flux quanta penetrate the area of the localised edge state.

Depending upon the size of the sample and the characteristic shape of the disorder potential, there can be many localised states in the bulk that can participate in coupling between edge states on opposite sample boundaries. However, due to the exponential dependence of tunnelling on the spatial separation, the inter-edge tunnelling will generally be dominated by a single mediating localised state in the bulk working as a "bottle-neck".

Taking this into the account, and assuming a circular shape of the localised state, a typical localised edge state is shown in Fig. 4.10. The quasiperiod ∇B of fluctuations in R_{xx} can be calculated [53] using

$$\phi_0 = \Delta B \frac{d(B\pi r^2)}{dB} = \Delta B \left(\pi r^2 + 2\pi r B \left(\frac{\partial r}{\partial \nu} \right)_\mu \frac{d\nu}{dB} \right), \tag{4.17}$$

where r is the radius of the bound state that dominates the inter-edge tunnelling. The first term corresponds to the Aharonov-Bohm phase, whilst the second term

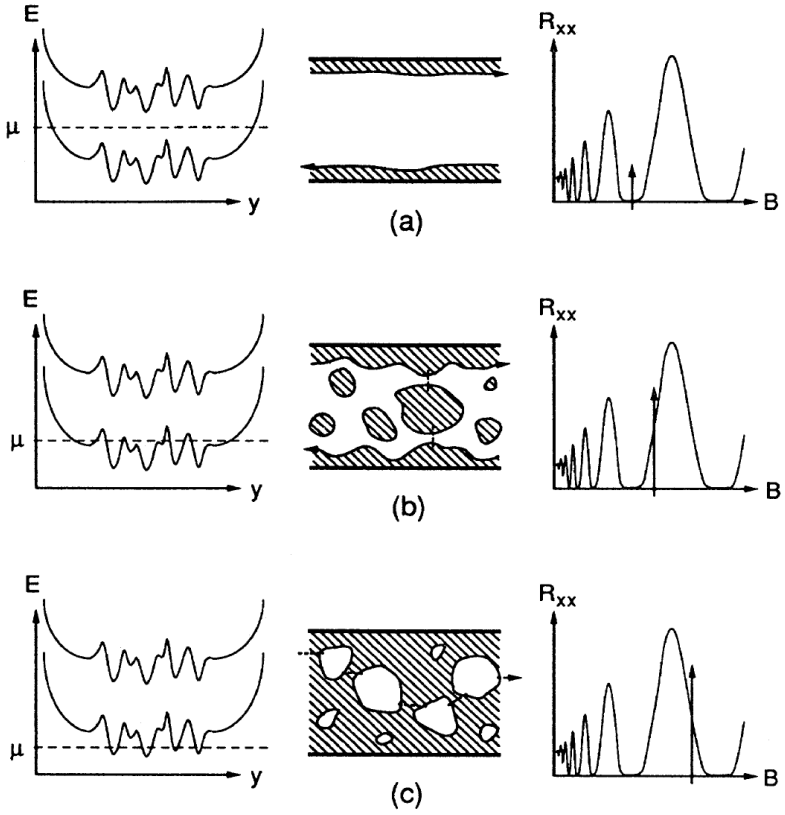

Figure 4.9: Illustration of edge state configurations as a function of Fermi energy μ. The left column of figures shows the relative energies of μ and two Landau levels; the centre column – the corresponding edge state configurations (where shaded regions represent energies above μ and dashed lines represent tunnelling paths); and the right column the corresponding values of B. In (a) μ lies well between two LLs, corresponding to well-separated edge states and B in an R_{xx} minimum. In (b) μ is lower in energy, corresponding to islands in the Fermi sea and B at the high-B side of an R_{xx} minimum. In (c) μ is lower yet in energy, corresponding to Fermi lakes on insulating land, and B at the low-B side of an R_{xx} minimum. Transport in (c) occurs by tunnelling along the length of the channel. Taken from [53].

corresponds to the change in energy of the Landau level. Assuming μ to be constant, $(\partial r/\partial\nu)_\mu = \hbar\omega_c/eE_r(\mu) = -\hbar B/m^*E_r(\mu)$, where E_r is the radial electric field of the bound state. The change in r with changing ν can be seen from Fig. 4.10 to be $dr = dE/\nabla U = (\hbar\omega_c d\nu)/eE_r$. From this we find for a 2D system with massive carriers the period in B-field to be

$$\Delta B = \frac{h}{e}\left(\pi r^2 + \frac{rh^2n}{m^*eE_r(\mu)}\right)^{-1}. \tag{4.18}$$

However, in graphene the result will be quite different due to the different energy spectrum of the Landau levels. Taking into account that in graphene $E_N =$

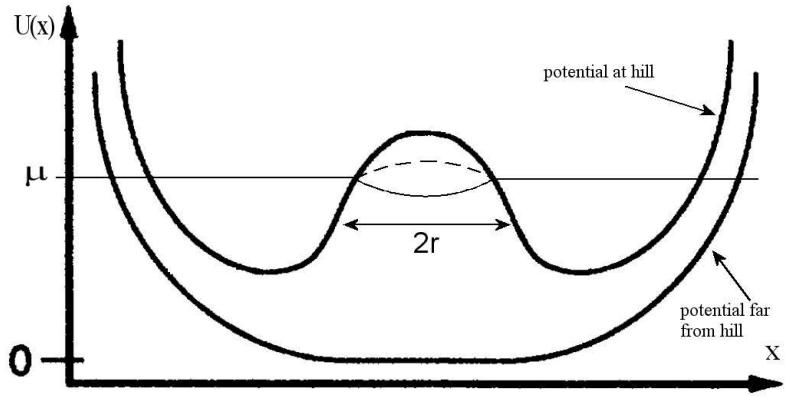

Figure 4.10: A simplified picture of a disorder-induced potential hill in a LL that lies below the Fermi level μ. This results in the existence of a localised edge state that allows tunnelling between edge states on opposite sides of the sample. Adapted from [53].

$\sqrt{2e\hbar v_F^2 B(N+1/2\pm 1/2)}$ and $\nu = nh/4eB$, we can anticipate that B still appears in the expression for ΔB in graphene.

Now, we find that

$$\frac{dr}{d\nu} = \frac{dr}{dE_N}\frac{dE_N}{d\nu} = \frac{v_F\sqrt{2e\hbar}}{eE_r}\left[\left(\frac{\partial\sqrt{B\nu}}{\partial B}\right)_\nu \frac{dB}{d\nu} + \left(\frac{\partial\sqrt{B\nu}}{\partial \nu}\right)_B\right], \tag{4.19}$$

where, as in [53], we relate the change in the radius with changing LL energy to the radial electric field of the disorder, $\frac{dr}{dE_N} = 1/e\nabla U = 1/eE_r$. Evaluating the above expression we find that

$$\frac{dr}{d\nu} = \frac{v_F\sqrt{2e\hbar}}{eE_r}\left[\sqrt{\frac{\nu}{B}}\frac{B}{\nu} + \sqrt{\frac{B}{\nu}}\right] = \frac{2v_F}{eE_r}\sqrt{\frac{2e\hbar B}{\nu}} = \frac{4v_F B}{E_r\sqrt{n\pi}}. \tag{4.20}$$

We can now substitute the above into Eq. 4.17 to find the period in magnetic field for graphene:

$$\Delta B = \frac{h}{e}\left(\pi r^2 + \frac{4\pi r E_F}{eE_r}\right)^{-1}, \tag{4.21}$$

where $E_F = \hbar k_F v_F = \hbar v_F\sqrt{n\pi}$ is the Fermi energy in graphene. Thus, in graphene the fluctuations in the tails of the resistance maxima due to tunnelling processes are still periodic in B, despite the energy spectrum of LLs in graphene being different from that in conventional 2D systems.

The expression for the period ΔB can be simplified in two limiting cases, depending upon whether the first term, related to the Aharonov-Bohm phase, or the second term, related to the change in the LL energy, dominates the behaviour of ΔB. In these cases we find the following simplified expressions:

$$\Delta B = \begin{cases} \frac{2\hbar}{er^2}, & \text{for } \frac{4E_F}{eE_r r} \ll 1, \\ \frac{\hbar}{2E_F}\frac{E_r}{r}, & \text{for } \frac{4E_F}{eE_r r} \gg 1. \end{cases} \tag{4.22}$$

It is also possible to measure fluctuations of the resistance at fixed magnetic field by varying the Fermi level (by changing the gate voltage). As the Fermi level moves through the flank of a LL, resonant tunnelling can occur in a similar manner to that discussed above for the case of a changing magnetic field. As was noted in [53], the disorder potential may vary with Fermi level, such that $E_r = E_r(E_F)$. For the purposes of making an estimate of the period in Fermi level between resonant tunnelling events, we assume here that the change E_r due to a small change in E_F can be neglected. Thus, starting from the quantisation condition of the bound states:

$$\phi_0 = \Delta E_F \frac{d(B\pi r^2)}{dE_F} = 2\pi r B \frac{dr}{dE_F}\Delta E_F = \frac{2\pi r B}{eE_r}\Delta E_F, \tag{4.23}$$

from which we find the period in Fermi energy to be

$$\Delta E_F = \frac{h}{e}\frac{eE_r}{2\pi r B} = \frac{\hbar E_r}{rB}. \tag{4.24}$$

Concerning the magnitude of the fluctuations in ρ_{xx}, Jain and Kivelson [80] studied the amplitude and field dependence of a system consisting of a single occupied edge state at each sample boundary and a single, circular localised state in the centre of the bulk through which inter-edge tunnelling could occur. They find for the amplitude of the resistance peak

$$R(\mu, T)_{xx} \sim \frac{1}{k_B T} \exp\left[\frac{|\mu - E_0|}{k_B T}\right], \tag{4.25}$$

where μ is the Fermi level and E_0 is the energy of the bound state. This expression is for the low-temperature limit, defined by $k_B T \ll \Gamma$, where $\Gamma \propto \exp(-2L_1^2/l_B^2)$ is the leak rate of the bound state in the bulk (L_1 is the distance between the bound

state and the nearest edge state, and $l_B = \sqrt{\hbar/eB}$ is the magnetic length).

It was noted in [80] that for higher temperatures the resonance peak in R_{xx} is broadened as the resonance can occur over an energy range of k_BT, but the magnitude of the peak decreases as at most a fraction of Γ/k_BT are in resonance. In fact, it is expected that only the states with $\Gamma \gg k_BT$ will be experimentally observable, as narrow peaks (small Γ) will be washed out even at the lowest experimentally available temperatures. For this reason the resonant peaks are expected to be absent at high fields (small l_B and thus narrow peaks) and in wide samples (large L_1 resulting in narrow peaks).

4.7 Basic characterisation

Characterisation of the graphene sample begins by measuring the gate voltage dependence of the resistivity, as shown in Fig. 4.11. By converting this to the conductivity as a function of concentration, plotted in the inset of Fig. 4.11, the mobility is found from the relation $\sigma = en\mu$. The mobility of holes and electrons away from the Dirac region is equal: $\mu_h = 20000\,\mathrm{cm}^{-2}/\mathrm{Vs}$ and $\mu_e = 20300\,\mathrm{cm}^{-2}/\mathrm{Vs}$, respectively.

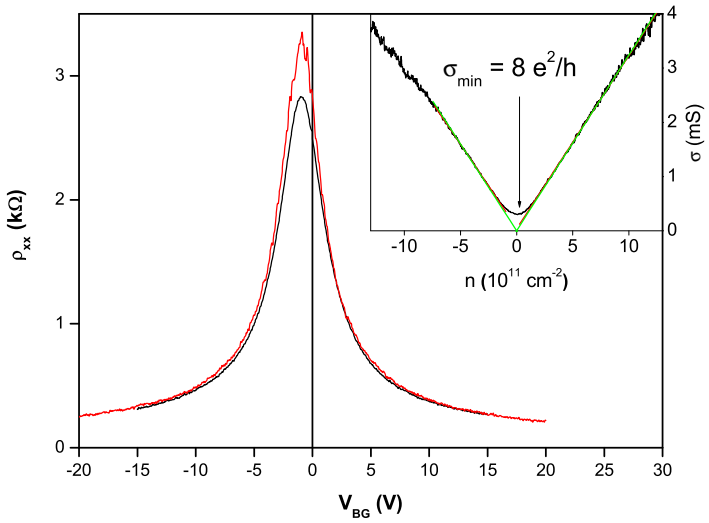

Figure 4.11: The resistivity as a function of back-gate voltage measured at 300 K (black line) and 5 K (red line). Inset: The conductivity as a function of concentration, measured at 5.6 K. Outside the vicinity of the Dirac point the conductivity varies linearly with concentration, reflecting a constant mobility. The mobilities of holes and electrons are nearly identical.

In the characterisation of the sample its magnetoresistance is next measured. The results are shown in Fig. 4.12. To test whether the sample is indeed a single layer of graphene, the longitudinal and Hall conductivities are found from the resistivities in Fig. 4.12, as shown in Fig. 4.13. The anomalous QHE is clearly seen – there is a peak in σ_{xx} due to the presence of a zero-energy LL. The conductivities are plotted in units of $4e^2/h$ to emphasise the fact that the quantised σ_{xy} plateaux correspond to half-integer filling factors. Note that the peaks in σ_{xx} are spaced periodically in V_G, despite the energy-spacing of LLs decreasing with increasing LL index (Fig. 4.6). This seemingly contradictory result is easily resolved by recalling that in graphene the degeneracy of a LL (per spin, per valley) is the same as in massive systems, i.e., eB/h, and that it is the concentration which is linearly dependent on V_G, rather than E_F.

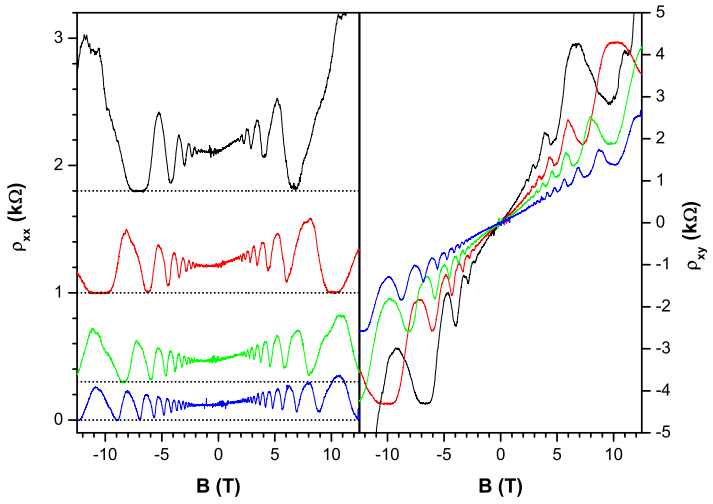

Figure 4.12: The longitudinal resistivity and Hall resistivity as a function of magnetic field for different electron concentrations: n = 1(black), 1.5(red), 2(green), 3(blue) $\times 10^{12}\,\mathrm{cm}^{-2}$; T = 5.6 K.

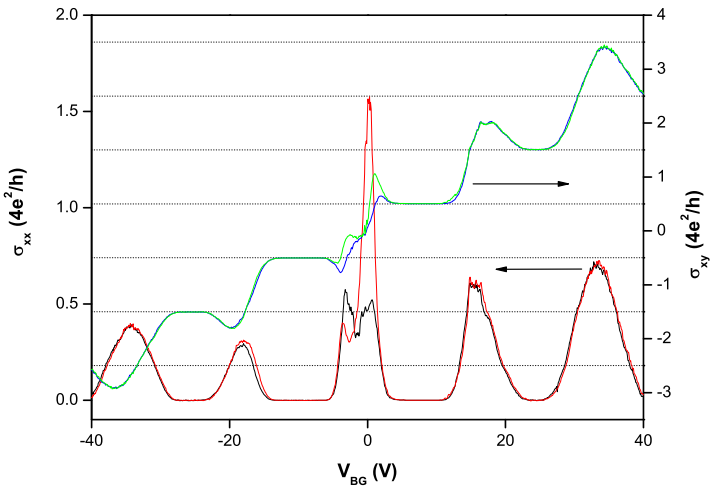

Figure 4.13: The longitudinal (black and red) and Hall (green and blue) conductivities as a function of gate voltage, measured at 5.6 K with $B = 12.5$ T. The presence of a LL at zero energy is clear from the peak in σ_{xx} at zero gate voltage and the half-integer filling factor is apparent from the quantised values of σ_{xy}.

4.8 Quantum lifetime in graphene

In graphene there is an ongoing debate as to the nature of scatterers. There are several possible sources of scattering in graphene, both "external", such as surface roughness of the SiO_2 substrate and charged impurities near the graphene sheet (in SiO_2 and on the graphene surface) [70], and "internal", such as defects in the graphene lattice [70] and ripples in the graphene sheet [81]. Measurements of the quantum lifetime τ_q provide an important tool for investigating the nature of scattering in graphene. By analysing the concentration dependence of τ_q and τ_p information about the nature of the disorder in graphene can be gained. Furthermore, the ratio τ_p/τ_q reflects whether the scattering comes from long-range ($\tau_p/\tau_q \gg 1$) or short-range disorder ($\tau_p/\tau_q \approx 1$).

Values for the quantum lifetime were found from the oscillating part of the magnetoresistivity $\Delta\rho_{xx}(B)$ using Eq. 4.10. This oscillating part of the resistivity was obtained from the measured magnetoresistance by subtracting a polynomial fit so as to remove the monotonic part of the magnetoresistance, as demonstrated in Fig. 4.14. The carrier concentration can be found from the period of the SdH oscillations in ρ_{xx} when plotted in inverse magnetic field, and these values for the concentration agree well with the values found from the capacitance of the gate-oxide (Eq. 4.1), with an error of less than 1%.

To find τ_q it is the shape of the exponential envelope of the SdH oscillations that must be analysed. To extract this envelope from the measured oscillations the logarithm of the peak amplitudes (marked by red circles in the left panel of Fig. 4.14) is plotted against the inverse magnetic field $1/B$, as shown in the right panel of Fig. 4.14. The gradient of this dependence is $\pi|E_F|/v_F^2 e\tau_q$ (Eq. 4.10, using $\Gamma = \hbar/2\tau_q$), and its value allows one to extract the values of τ_q.

The concentration dependence of τ_q found from the gradient is plotted in Fig. 4.15 for different temperatures in the range $T = 0.05$ – 5.5 K. We see that τ_q varies roughly as $n^{0.5}$ for both holes and electrons ($\tau_q \propto n^{0.47}$ for holes, and $\tau_q \propto n^{0.65}$ for electrons). This is in good agreement with the concentration dependence of τ_p for the case of charged impurity scattering, as discussed in [82], which predicts an $n^{0.5}$ dependence.

The behaviour of τ_p and τ_q with changing concentration has been studied in

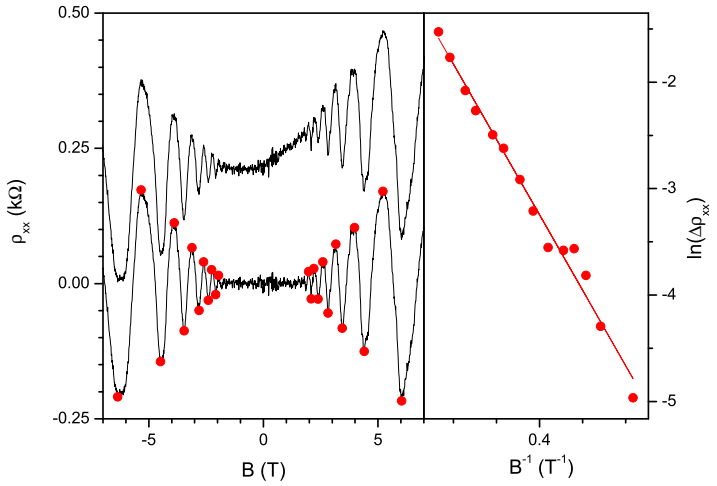

Figure 4.14: Left panel: the longitudinal resistivity ρ_{xx} (upper graph) and its isolated oscillating component $\Delta\rho_{xx}$ (lower graph) as a function of magnetic field; $T = 5.5$ K, $n = 1.5{\times}10^{12}\,\mathrm{cm}^{-2}$. Right panel: the logarithm of the peaks of the SdH oscillations plotted against inverse magnetic field. The solid line is a linear fit, the gradient of which is proportional to $1/\tau_q$.

conventional systems for different sources of disorder [83–85]. Given the SiO_2 substrate used in graphene samples, it is sensible to compare our results to the theories developed for Si MOSFET samples. Three different sources of disorder were generally considered: remote impurities, homogenous background impurities, and surface roughness. Remote impurities could refer to impurities deep within the bulk of the SiO_2, and are screened by mobile electrons in the 2DEG, resulting in a smoothly varying long-range disorder potential. (The case of remote impurities is more relevant to modulation doped GaAs structures, and does not contribute significantly to scattering in Si MOSFETs.) Background impurities refer to impurities that exist in the same location as the 2DEG. Roughness scattering refers to the fluctuations in the surface height of the SiO_2 interface. In [83] the behaviour of the mobility is studied theoretically for the three different sources of scattering, and their results are summarised in Table 4.1. The difference in τ_p and τ_q is dependent upon the dominant source of scattering, and the ratio τ_p/τ_q was studied in [84], the results of which are summarised in Table 4.2.

In our experiment, the change in τ_q with changing temperature is very small – of the same size as the experimental uncertainty in the hole-region densities, and

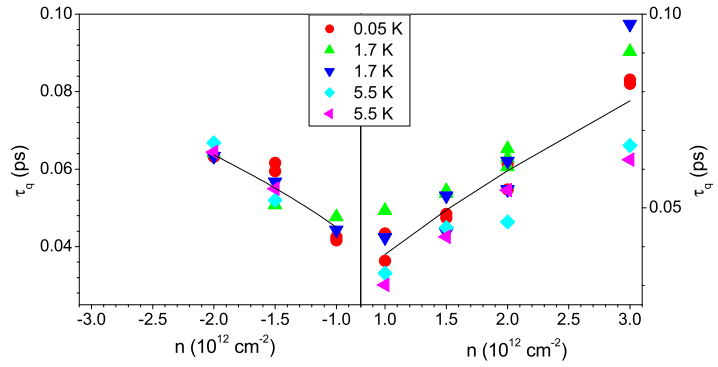

Figure 4.15: Density dependence of τ_q for hole and electron regions for different temperatures. The solid lines are power-law fits: $\tau_q \propto n^{0.47}$ in the hole region, and $\tau_q \propto n^{0.65}$ in the electron region.

	small n	large n
Background impurities	$\tau_p \propto n^{1/2}$	$\tau_p \propto n^{3/2}$
Remote impurities	$\tau_p \propto n^{-1}$	$\tau_p \propto e^{k_F a}/n$
Roughness	$\tau_p \propto n^{-1}$	$\tau_p \propto n^{3/2}$

Table 4.1: Theoretical prediction for the n-dependence of τ_p for different sources of scattering in conventional 2D systems [83]. For the case of remote impurity scattering at high concentrations, a is the quantum well width of the 2DEG.

in the electron-region there is only an increase of $\sim 50\%$ in τ_q over an increase in temperature of two orders of magnitude. This is in agreement with that expected [83] for impurity scattering in degenerate systems ($k_B T \ll E_F$).

In the inset of Fig. 4.11 we show that in our sample the conductivity increases linearly with increasing concentration outside the Dirac region. It has been shown using Boltzmann transport theory that such a linear dependence on concentration can not be accounted for by short-range scatterers, which results in a constant conductivity [86], and that in order to obtain the linear concentration dependence one can instead use a Coulomb scattering potential [82]. Thus, the linear $\sigma(n)$ dependence seen in our sample indicates that the disorder is well described by Coulomb scatterers.

It is interesting to compare these values of τ_q to the transport time τ_p found from the mobility. From Fig. 4.11 our mobility is $\mu = 20,000\text{cm}^2/\text{Vs}$, and $\tau_p = (\sqrt{\pi}\hbar\mu/ev_F)\sqrt{n}$. The resulting values of the transport and quantum lifetimes are plotted together in Fig. 4.16, and for all concentrations measured, $\tau_p/\tau_q \approx 7$. Thus,

	τ_p/τ_q	conditions
Background impurities	$(1+2k_F/q_{TF})^2[(\pi/3)C_2+\ln(4E_F\tau_q)]$	$4E_F\tau_q \gg 1$
Remote impurities	1	$4k_F\|z_i\| \ll 1$
Remote impurities	$(2k_F\|z_i\|)^2$	$4k_F\|z_i\| \gg 1$
Roughness	2/3	$k_F\Lambda \ll 1$
Roughness	$(k_F\Lambda)^2/3$	$k_F\Lambda \gg 1$

Table 4.2: Expected ratio of τ_p to τ_q for different sources of scattering in conventional 2D systems [83]. For the case of background impurities, q_{TF} is the Thomas-Fermi screening wavenumber, and C_2 is a coefficient that depends on the quantum well width, q_{TF} and k_F. (The ratio τ_p/τ_q increases linearly with increasing n for the case of background impurities [83].) For the case of remote impurity scattering, z_i is the distance of the impurities from the 2DEG. For the case of roughness scattering, Λ is the correlation length of the fluctuations in the height of the SiO_2 interface.

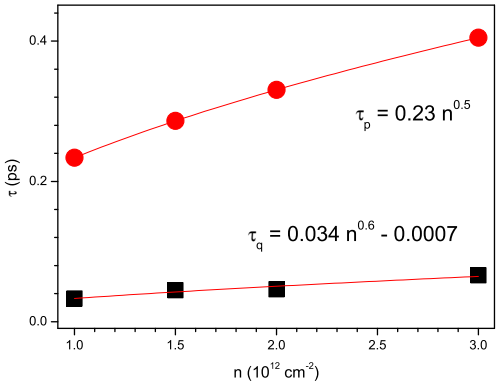

Figure 4.16: Comparison of τ_q (black squares) and τ_p (red circles) as a function of concentration. Solid lines are power-law fits. Measurements done at $T = 5.5$ K.

our measurements of τ_q indicate that the disorder in graphene does have some long-range behaviour. Note also that both scattering times extrapolate to approximately zero in the limit of zero concentration.

Detailed measurements of graphene scattering times have not been reported yet, although some estimates can be made from measurements of the LL broadening made by Zhang *et al.*. In their paper, they showed that the LL broadening could be described by the momentum relaxation time found from the mobility [87]. Given that the LL broadening is $\hbar/\tau_q$, this observation suggests that $\tau_p \approx \tau_q$. However, they state agreement only in the order of magnitude, and so it is possible that their LL broadening actually corresponds to a τ_q that is smaller than their measured τ_p, similar to what we observe in our more detailed measurement of the ratio τ_p/τ_q.

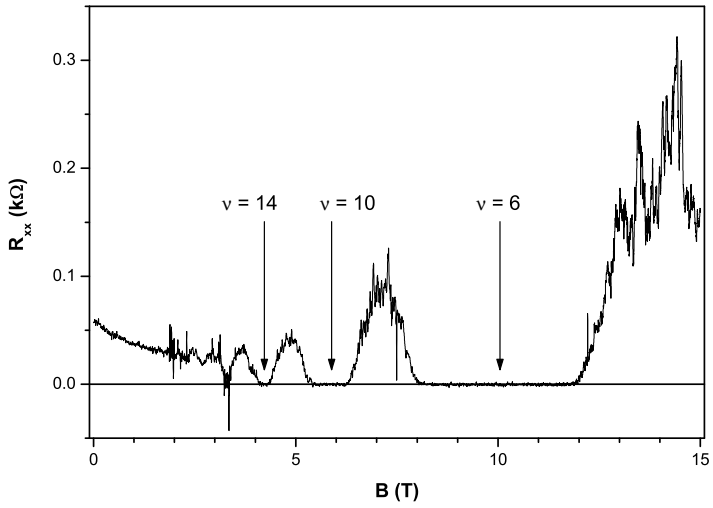

Figure 4.17: R_{xx} as a function of B for $n = 1.5{\times}10^{12}\,\mathrm{cm}^{-2}$; $T = 50$ mK. The filling factor values are found from the position in B of centres of minima in R_{xx}.

4.9 Resistance fluctuations in the IQHE regime

When measuring the fluctuations in the resistance of the studied sample at high fields, the circuit was arranged differently from when the initial characterisation and τ_q described in the previous sections were made. This was necessitated due to the loss of contact C in Fig. 4.1. In the new circuit arrangement, contact A was used a source, contact D as the drain, and the longitudinal resistance was measured between contacts B and E. The peak positions in the longitudinal resistance at $T =$ 50 mK are shown in Figure 4.17 as a function of B-field. At this low temperature fluctuations in R_{xx} are clearly seen.

To study the resistance fluctuations in detail the resistance peak corresponding to the $\nu = 6 \rightarrow 10$ transition is chosen. Figure 4.18 presents measurements of this peak as a function of B-field for $T = 50$ mK, 400 mK, and 1.36 K. The peak is seen to increase in size and move to higher B as the temperature is increased, whilst the fluctuations decrease in amplitude and become broader.

The fluctuations are also measured as a function of gate voltage whilst keeping the magnetic field constant. Figure 4.19 shows repeat sweeps of the gate voltage for a fixed 7.3 T magnetic field. Due to charging effects in our sample which began to occur at this stage of experiments, the position of the resistance peak shifts in gate voltage between repeat sweeps. Given the need for the system to remain stable whilst

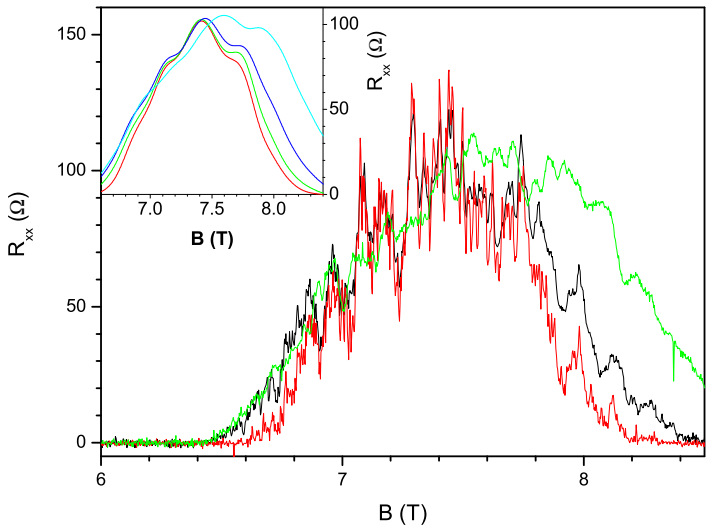

Figure 4.18: R_{xx} as a function of B for different temperatures: $T = 0.05$, 0.4, and 1.36 K; $n = 1.5 \times 10^{12}\,\mathrm{cm}^{-2}$. Inset: the average background $R_{xx}(B)$ with the mesoscopic fluctuations removed by averaging of the data, as described in $S4.10$.

the fluctuations are measured repeatedly for several different temperatures, varying-gate voltage measurements could therefore not be employed for detailed studies of the temperature dependence of fluctuations. Useful information can still be taken from the measurements shown in Fig. 4.19, such as testing the ergodicity of the fluctuations. Furthermore, an advantage of fluctuations as a function of V_G is that the tunnelling resonances that can be the mechanism behind resistance fluctuations in the flanks of the LL would be expected to be periodic in the Fermi-energy (for the case of a single localised edge state determining the inter-edge scattering between edge states), as described in Section 4.6.2. This period in Fermi energy ΔE_F can be compared to the period in magnetic field ΔB, found from the fluctuations of $R_{xx}(B)$ in the flanks of the LL. From this, one can gain information about the disorder in the graphene flake, such as r and E_r (see Section 4.6.2), which describe the amplitude of the fluctuations in the disorder potential, and the typical spatial extent of those fluctuations.

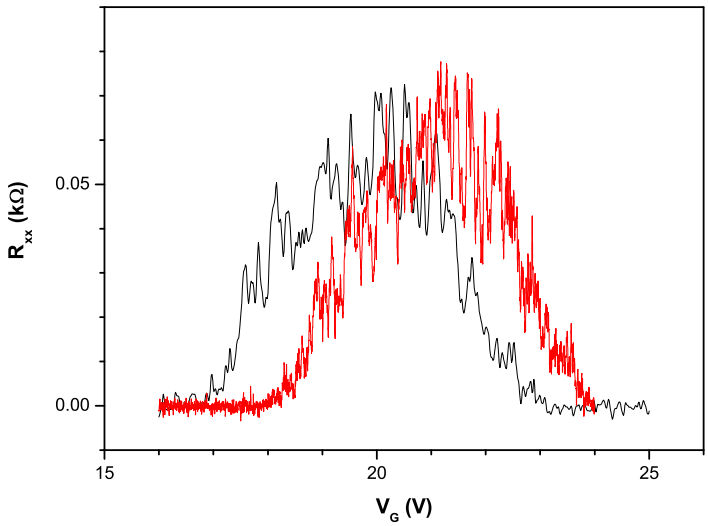

Figure 4.19: R_{xx} as a function of gate voltage at $T = 50$ mK; $B = 7.3$ T, corresponding to the transition $\nu = 6 \rightarrow 10$. The different graphs are for different sweeps in the same direction, reflecting a tendency for charging to occur in the substrate. (Note that the resistance peak as a function of B was stable in Fig. 4.18 for a fixed V_G.)

4.10 Fluctuations in the centre of the Landau level

To analyse only the mesoscopic fluctuations in the resistance the average macroscopic background resistance must be identified and removed. This is done by adjacent-point averaging of the $R_{xx}(B)$ measurements, the results of which are shown in the inset to Fig. 4.18. (In adjacent-point averaging each measurement of $R_{xx}(B)$ is "smoothed" by calculating the average value of $R_{xx}(B)$ over a defined interval $[B - \Delta B, B + \Delta B]$.) A nearly T-independent region in the centre of the resistance peaks can be discerned in the range of magnetic field 7 T$< B <$ 7.5 T, which can be identified as corresponding to the energy-range in which transport is dominated by extended states in the bulk, i.e., the centre of the LL.

The average background resistance is subtracted from the measured R_{xx} in Fig. 4.18 to obtain the mesoscopic fluctuations of the resistance, ΔR_{xx}. We can make a first attempt at describing the fluctuations over the whole extent of the peak using the model of [77]. To do this the resistance peak is divided into 14 overlapping magnetic-field intervals of 330 mT. The interval size is chosen such that at least

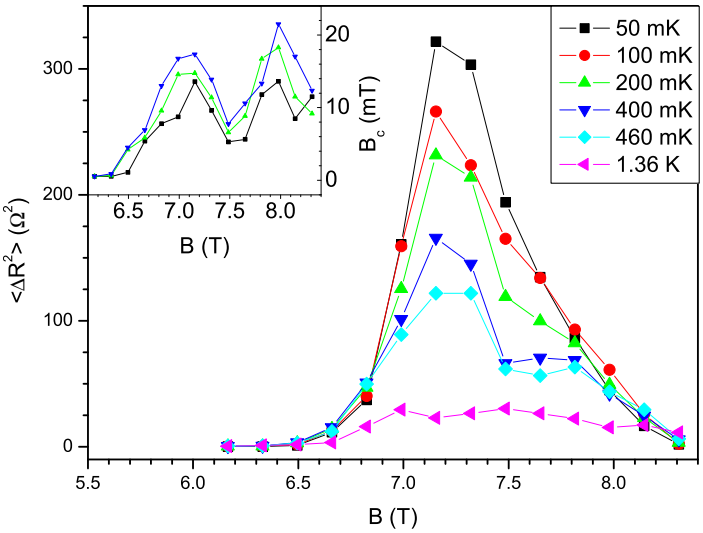

Figure 4.20: The variance of the fluctuations in R_{xx} as a function of B for various T; $n = 1.5 \times 10^{12}\,\mathrm{cm}^{-2}$, corresponding to the centre of the resistance peak in the transition $\nu = 6 \rightarrow 10$. Inset: The correlation magnetic field of the fluctuations in R_{xx} as a function of B for various T.

ten fluctuations are included within an interval. The ACF is then calculated for each interval such that the variance and correlation field can be found as a function of magnetic-field across the resistance peak. Fig. 4.20 shows the dependence of the variance on magnetic field for different temperatures. The limited number of intervals that the peak can be divided into means that observing the resonances predicted in [77] is unlikely. The peak in the variance of the fluctuations does seem to occur in the centre of the LL, as identified by the temperature-independent region of the average resistance, which is in agreement with [77].

The inset to Fig. 4.20 shows how the correlation magnetic field varies across the LL. Whilst no prediction was made in [77] for the behaviour of the quasiperiod of the fluctuations for different regions of the LL, we can refer to Eq. 4.16 where the correlation field is predicted to mirror the behaviour of the resistance peak itself, $B_c \propto \varrho(E_F)\rho_{xx}$. This effect is indeed seen, as there is a peak in B_c at $B \approx 7.2$ T, similar to that seen in both the variance and the average resistance $R_{xx}(B)$. There is also an apparent second peak at $B \approx 8$ T, which we can not account for. It is present regardless of the size of the B-field interval over which the ACF is calculated. This independence of the effect on window-size reduces the likelihood of this being

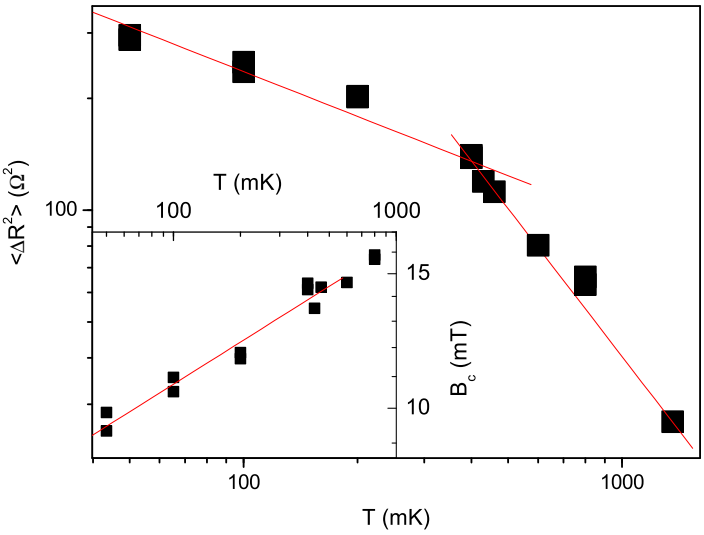

Figure 4.21: The temperature dependence of the variance of the $R_{xx}(B)$ fluctuations near the centre of the resistance maximum; $n = 1.5 \times 10^{12}\,\mathrm{cm}^{-2}$. Inset: temperature dependence of the correlation magnetic field.

due to too few fluctuations being analysed in the high-B flank.

The temperature dependence of the variance of the fluctuations in the centre of the LL is shown in Fig. 4.21. The variance is seen to decrease with increasing temperature, in agreement with the raw results in Fig. 4.18. Interestingly, there appears to be a transition from a weak temperature dependence below $T \approx 400$ mK, to a much stronger one above 400 mK. At low temperatures the variance decreases with temperature as $T^{-0.4}$, whilst at higher temperatures it decreases as $T^{-1.3}$, which is in good agreement with Eq. 4.15, from which we expect a $T^{-1.5}$ dependence. The inset of Fig. 4.21 shows the temperature dependence of the correlation field, $B_c(T)$ (the 1.36 K data-point was not included in the temperature dependence fit, as the number of resolved fluctuations was too few to produce a reliable value of B_c). Here we see that $B_c(T)$ is only weakly temperature dependent for the whole range of temperatures measured, going as $T^{0.2}$. This dependence is much weaker than would be expected from Eq. 4.16, where B_c is predicted to increase linearly in T.

One has to note, however, that in analysing the behaviour of the variance and B_c using the models in [77] and [78] we arrive at a problem: Eqs. 4.15 and 4.16 require that $L_T/(1+\gamma^2)^{1/2}W > 1$. In our system, the diffusion coefficient is $D = E_F\mu/2e = 1400\,\mathrm{cm}^2/\mathrm{Vs}$, which results in a thermal length of $L_T = \hbar D/k_B T =$

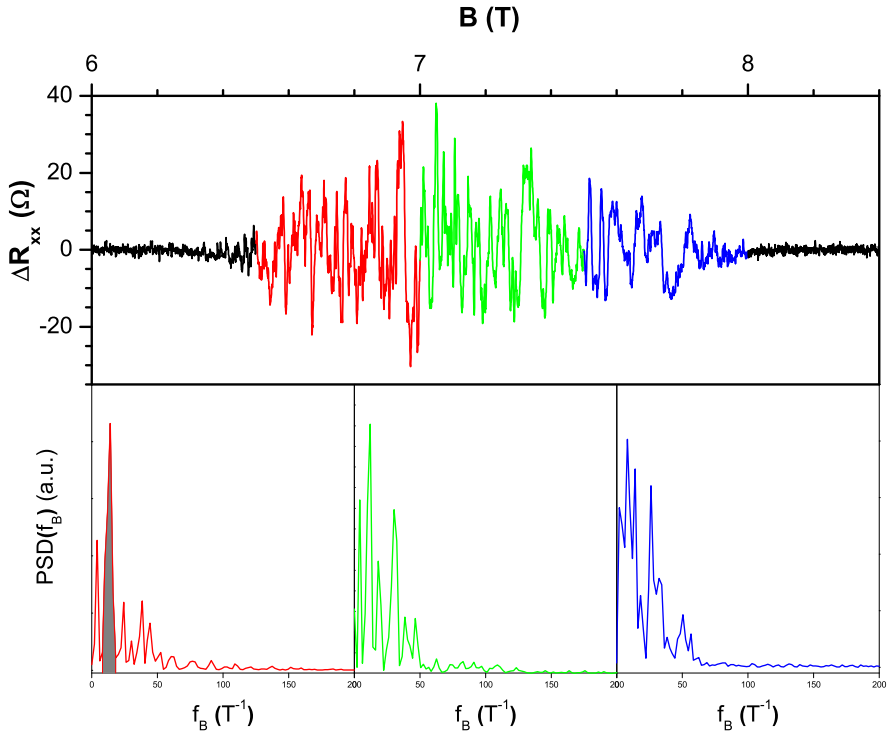

Figure 4.22: Top: colour-coded index of the division of the resistance peak fluctuations into regions prior to calculating the PSD. Bottom 3 panels: The PSD of the fluctuations. There is some suggestion of a dominant frequency (shaded) in the left flank of the LL, indicating a tunnelling process via a single localised edge state. The cental region and right flank have a variety of frequency components.

4.7 μm. The sample width is $W \approx 3$ μm, and $\gamma = (L/W)R_{xy}/R_{xx} \approx 9$, resulting in $L_T/(1+\gamma^2)^{1/2}W = 0.2$, such that the expressions for the variance and correlation field are not strictly valid under our experimental conditions.

4.11 Fluctuations in the flanks of the Landau level

In order to detect the regions of the LL where either tunnelling or UCF is the dominant mechanism, the resistance peak is broken into different regions of magnetic field and the PSD of each region is calculated, as shown in Fig. 4.22. Towards the flanks of the peak tunnelling is expected to be dominant, and the PSD will show a dominant peak at a given magnetic-frequency $f_B = 1/\Delta B$, where ΔB is expected

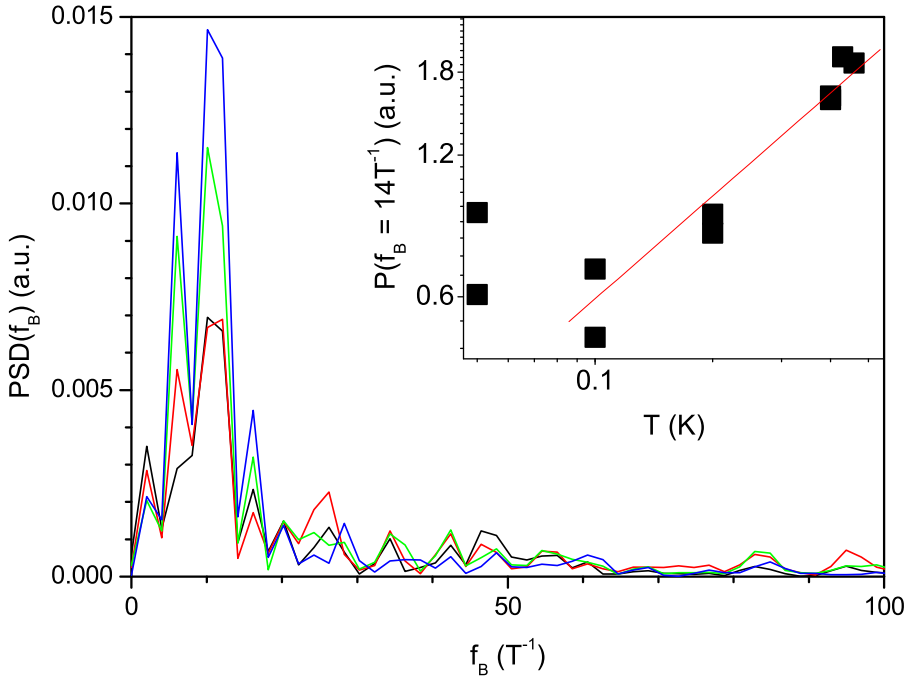

Figure 4.23: The PSD of the fluctuations in the low-field flank of the fluctuations in $R_{xx}(B)$ for different temperatures; $T = 0.05$, 0.1, 0.2, 0.4 K, $n = 1.5 \times 10^{12}\,\mathrm{cm}^{-2}$. Inset: temperature dependence of the peak in the PSD at the dominant magnetic frequency $f_B = 14\,\mathrm{T}^{-1}$.

to be given by Eq. 4.21. Such a peak is indeed seen in the low-B flank of the LL at $f_B = 14\ \mathrm{T}^{-1}$ (red graph of Fig. 4.22). The high B-field flank does not show such a pronounced peak, which can be due to the different degree of screening present in the two flanks. The low-B flank corresponds to an almost fully occupied LL moving up towards the Fermi level, and so screening of disorder is much stronger in the low-B flank than in the high-B flank due to the greater number of electrons. Similar to the high-field flank's fluctuations, the PSD of the fluctuations near the centre of the LL does not show a dominant period in the fluctuations (green graph of Fig. 4.22), as expected for the centre of the LL where fluctuations are expected to be described by a modified UCF theory.

The temperature dependence of the PSD of the resistance fluctuations in the low-field flank of the LL is shown in Fig. 4.23, whilst the temperature dependence of the dominant frequency peak is shown in the inset on a logarithmic scale. The amplitude of the peak increases with increasing temperature as $T^{0.7}$. This is in

disagreement with the expected behaviour in the resonant tunnelling model, Eq. 4.25 predicting the resistance amplitude to decrease linearly with temperature.

To explain this effect, one can recall the mesoscopic fluctuations of the resistance along localised states. In particular, a peak in the resistance can occur when transport between levels with different energy is via hopping. Such hopping peaks increase in amplitude with increasing temperature [88]. Furthermore, almost periodic fluctuations in the resistance as a function of B can also occur in the case of hopping transport between localised states [89].

4.12 Comparison with gate voltage fluctuations

An important property of UCF fluctuations in weak fields is that of ergodicity (Section 2.1.1): that changing the external magnetic field or Fermi level of the system is equivalent to changing the disorder configuration. We can check that the fluctuations in R_{xx} are ergodic at high B-fields near the LL centre by comparing the variance of the fluctuations for varying magnetic field and varying gate voltage. In Fig. 4.24 the ACF of the resistance fluctuations near the LL centre are plotted for varying B (left) and V_G (right). One can see that the variance of the $R_{xx}(B)$ fluctuations is about twice that of the $R_{xx}(V_G)$ fluctuations, indicating that the fluctuations are not ergodic. However, some uncertainty is cast over this conclusion by the difference in the size of the average resistance peak in the two sets of experiments. Referring to Figs. 4.18 and 4.19 we see that the peak in $R_{xx}(B)$ is $100\,\Omega$, whilst it is smaller when measured as a function of gate voltage, $R_{xx}(V_G) = 62\,\Omega$, probably due to recharging of the substrate, which changes the scattering of electrons.

The correlation field of the $R_{xx}(B)$ fluctuations is 5.7 mT, which corresponds to coherence length of $L_\varphi = 0.85$ μm using Eq. 2.7. Using $D(B = 7\,\mathrm{T}) = 4.9\,\mathrm{cm}^2/\mathrm{Vs}$, this corresponds to a coherence time of $\tau_\phi^B = 1.5$ ns. This is in good agreement with values of τ_ϕ found from weak localisation measurements of a graphene flake with a mobility of $\mu = 5100\,\mathrm{cm}^2/\mathrm{Vs}$ and concentration $n = 1.5 \times 10^{12}\,\mathrm{cm}^{-2}$ [90], where they observed $\tau_\phi = 2$ ns. The quasiperiod of the fluctuations in $R_{xx}(V_G)$ is 0.082 meV. This should be compared to the expected correlation energy of $E_c \approx 3k_BT = 0.01$ meV, provided $L_T < L_\varphi$ [32, 91]. The thermal length calculated from the temperature is $L_T(B,T) = (\hbar D(B)/k_BT) = 0.3$ μm using $T = 50$ mK, and

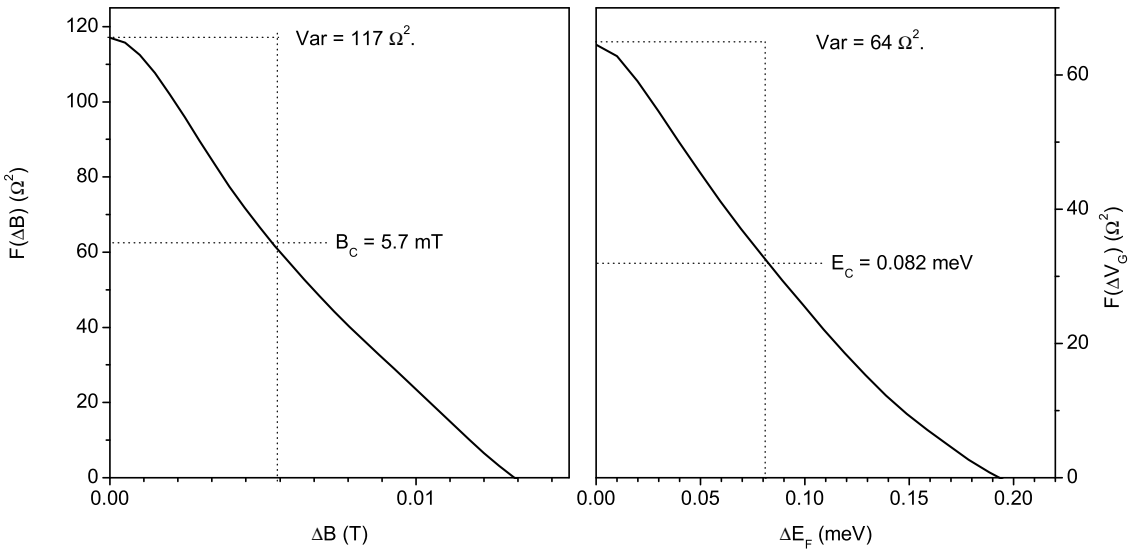

Figure 4.24: The autocorrelation function of the fluctuations of R_{xx} near the centre of the resistance peak, measured by varying B (left) and V_G (right) .

$D(B = 7\,\mathrm{T}) = 4.9\,\mathrm{cm}^2/\mathrm{Vs}$, which is smaller than the coherence length $L_\varphi = 0.85$ μm found from the correlation magnetic field of the fluctuations in $R_{xx}(B)$.

In Fig. 4.25 the resistance fluctuations are plotted as a function of the Fermi energy E_F after the average background resistance has been removed. Similar to the varying B-field measurements, the R_{xx} peak is split into the three regions where different mechanisms behind the fluctuations are expected to be at play. The PSD of the two flank regions both show dominant peaks, with frequencies of $f_E = 0.9\,\mathrm{meV}^{-1}$ and $0.6\,\mathrm{meV}^{-1}$ for the low-V_G and high-V_G flanks, respectively. By comparing the period in magnetic field ΔB found in Section 4.11 to the period in Fermi energy, we can extract information about the disorder potential in graphene (as discussed in Section 4.6.2). The appropriate Fermi energy period to compare with that measured in the low B-field flank is that found from the high energy flank, $E_F = 1/0.6 = 1.7$ meV. Using this value of the period in energy in Eq. 4.24, the ratio of the radial electric field of the potential hill of the localised edge state to the radius of the localised edge state is found to be $E_r/r = (B/\hbar)\Delta E_F = 18\,\mathrm{V}/\mu\mathrm{m}^2$.

In the case that the term in Eq. 4.21 related to the Aharonv-Bohm phase is negligible, i.e., $\frac{4E_F}{eE_r r} \gg 1$, we can describe the period in magnetic field by $\Delta B = \frac{\hbar}{2E_F}\frac{E_r}{r}$ (Eq. 4.22. Thus, combining this with Eq. 4.24 we can obtain an expression for the ratio of the periods in Fermi energy and magnetic field:

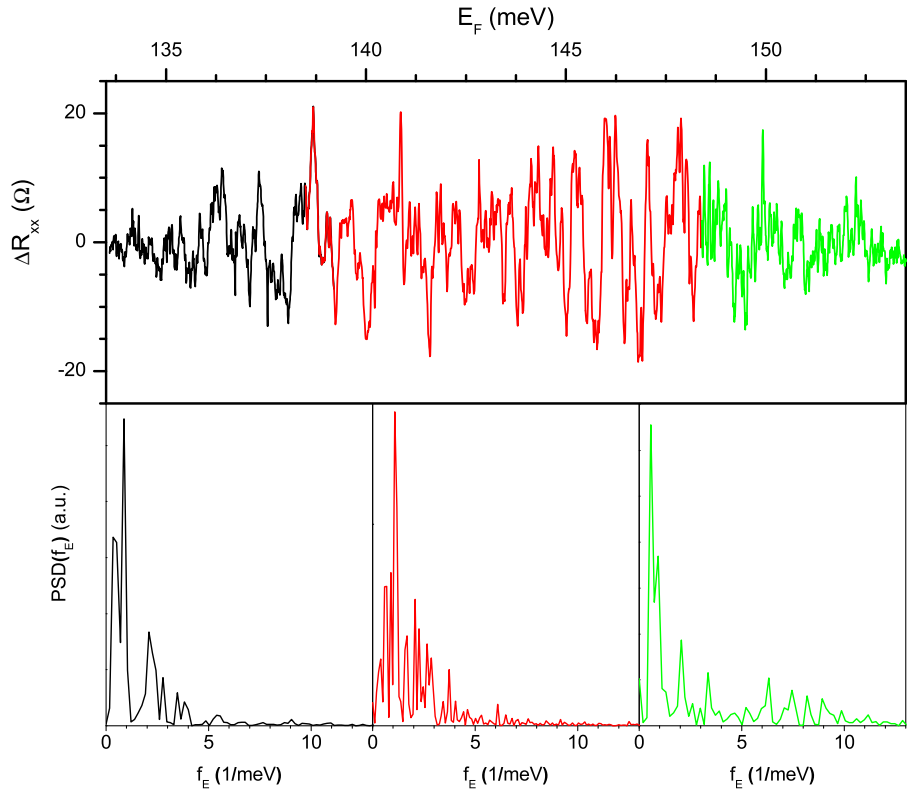

Figure 4.25: Top: The longitudinal resistance as a function of the energy after the average background has been subtracted; $T = 0.05$ K, $B = 7.3$ T. Bottom: the PSD of the fluctuations in different regions of the LL.

$$\frac{\Delta E_F}{\Delta B} = \frac{2E_F}{B}, \tag{4.26}$$

where $E_F = 143$ meV is the constant Fermi energy used when measuring the fluctuations of $R_{xx}(B)$ in the LL flank, and $B = 7.3$ T is the constant magnetic field used when measuring the fluctuations of $R_{xx}(B)$ in the LL flank. This expression gives an expected value for the ratio of 39 meV/T. The measured periods in energy and magnetic field are $1/0.6 = 1.7$ meV and $1/14 = 0.07$ T, respectively, resulting in a ratio of 23 meV/T. Thus, the good agreement in the ratios indicates that it is correct to take the limit of $\frac{4E_F}{eE_r r} \gg 1$ in Eq. 4.22. It is possible to use this condition to estimate a maximum size for the localised edge state:

$$r^2 \ll \frac{4E_F}{e(E_r/r)}. \tag{4.27}$$

Using the ratio $E_r/r = (B/\hbar)\Delta E_F = 18\,\mathrm{V}/\mu\mathrm{m}^2$ found from the period in the Fermi energy, the maximum size of the localised edge state is $r \sim 20$ nm. This is in good agreement with measurements of the size of electron puddles in graphene found by scanning single-electron transistor measurements [92], where they estimated an upper bound for the intrinsic disorder length scale of 30 nm.

This estimate for the length scale of disorder in the graphene corresponds to a value of the radial electric field of the disorder of $E_r \sim 3 \times 10^5\,\mathrm{V/m}$. In previous measurements of fluctuations of the resistance in the LL flanks in a conventional GaAs/AlGaAs heterostructure system, a value of $E_r \sim 3{\times}10^5\,\mathrm{V/m}$ was assumed and found to give consistent values for the length scale of disorder for their system [53], although the disorder in graphene is likely to be very different from that in high-mobility, modulation doped structures.

4.13 Conclusion

We have studied the concentration and temperature dependence of the quantum lifetime in graphene, which has not as yet been published elsewhere. The temperature dependence of τ_q is found to be weak, at least at temperatures below 6 K. From measurements of the amplitude of SdH oscillations for different concentrations, τ_q was found to increase as $n^{0.5}$ with increasing concentration. This behaviour was observed for both electrons and holes. The transport time τ_p was also found to have a similar concentration dependence of $n^{0.5}$, indicating that the mobility is well described by screened Coulomb scatters. The quantum lifetime was much smaller than the transport time for all concentrations measured, with $\tau_p/\tau_q \approx 7$, indicating some degree of long-range disorder in graphene.

It would be interesting to extend the τ_q measurements to higher concentrations to see if whether τ_q continues to increase as $n^{0.5}$ with increasing concentration. It would also be interesting to measure τ_q at higher temperatures. More statistics on different samples, using different substrates and obtained in different fabrication conditions would be important to resolve the existing controversy about the nature of scattering in graphene.

We have also investigated the resistance fluctuations in graphene in the IQHE regime as a function of magnetic field and Fermi energy. The resistance peak corre-

sponding to the $\nu = 6 \rightarrow 10$ transition was measured in different regions of the LL. The fluctuations were then analysed separately using different theoretical models in the LL centre and its flanks. The behaviour of the variance and quasiperiod of the fluctuations near the centre of the Landau levels was found to be in qualitative agreement with existing theories for conventional 2D systems. The variance was seen to decrease with increasing temperature as $T^{-1.3}$ at higher temperatures (T >0.4 K), in good agreement with the $T^{-1.5}$ dependence predicted by existing theories for conventional 2D systems. At lower temperatures the variance increased more slowly with decreasing temperature, going as $T^{-0.4}$, an effect which still requires explanation. The correlation B-field of the fluctuations was seen to decrease with increasing temperature, although it had a weaker temperature dependence of $T^{-0.4}$ compared with the expected T^{-1}.

In the LL flanks periodic fluctuations were detected, suggestive of the resonant tunnelling models discussed for conventional 2D systems. However, we observed an increase in the amplitude of these peaks with increasing temperature, which is in qualitative disagreement with the tunnelling models and suggests that these peaks have an origin in hopping transport. The magnetic field and energy periods of the fluctuations in R_{xx} in the LL flanks was found from the power spectral density of the fluctuations. By comparison of the periods in B and E_F an upper bound on the length scale of disorder in graphene was estimated to be 20 nm, in sensible agreement with observations by other groups [92], and an electric field strength of the disorder of $E_r \sim 3 \times 10^5$ V/m.

There are several promising extensions that can be made to the measurements of resistance fluctuations at high magnetic fields. Whether the behaviour is the same for different resistance peaks (different filling factors) is an interesting question, particular for the LL occurring at the Dirac point, which is unique to graphene. Measurement of the fluctuations there may shed light on the origin of the transport there, and the observed minimum in conductance. Similar studies of the high B-field fluctuations could also be performed on bilayer graphene samples, which also have unusual properties such as an anomalous quantum Hall effect and zero energy band gap, whilst, in contrast to monolayer graphene, the charge carriers are massive.

Chapter 5

Conclusion and suggestions for future work

In this thesis we report the first study of mesoscopic fluctuations of the Coulomb drag resistance. These fluctuations are seen both as a function of concentration and magnetic field, and at low temperatures are seen to exceed the average drag resistance, resulting in the sign of the drag alternating randomly with changing concentration and magnetic field. Compared with theoretical predictions, we observed an unexpected enhancement of the amplitude of drag fluctuations – by four orders of magnitude – as well as an unusual temperature dependence of the variance: T^{-1} at low temperatures, before a transition at $T \approx 200$ mK to a stronger, T^{-4} dependence. These observations prompted further theoretical work, extending the understanding of mesoscopic drag into the ballistic regime of drag where the mean free path is larger than the interlayer separation, $l \gg d$. It was found that our observations could be accounted for by considering the significant role that fluctuations of the local properties of the 2DEGs play in the ballistic regime of drag.

Measurements of the mesoscopic drag fluctuations were extended into the regime of strong magnetic fields at which the lowest Landau level is half occupied and transport is described by composite-fermion quasiparticles. Fluctuations of the drag resistance between composite fermions was observed, both as a function of varying concentration and magnetic field. A large enhancement of the drag was observed, both in the average drag, as reported previously by other groups, and also in the drag fluctuations. Similar to the case of weak magnetic fields, the fluctuations of the drag

between CFs exceed the average drag at low temperatures, resulting in alternating positive and negative drag as a function of concentration and magnetic field. The ratio of the correlation magnetic field to the correlation concentration was found to be $2\phi_0$ ($\phi_0 = h/e$ is the magnetic flux quantum), confirming previous observations and predictions for the fluctuations of resistance in composite fermions. We observed a strong T^{-3} dependence of the variance of the drag resistance fluctuations, whilst the coherence length measured from the correlation magnetic field of the fluctuations was found to be well described by the conventional expression for the dephasing rate in the diffusive regime of e-e interaction. These observations are in contradiction with existing theories describing the mesoscopic fluctuations of drag resistance in CF systems, where the variance of the resistance fluctuations is predicted to decrease with temperature as T^{-1}. We account for the discrepancy between our results and the theoretical model derived for diffusive drag fluctuations by the fact that our system is in the ballistic regime of drag, and the dimensionless conductance of the samples is $g_{cf} \approx 4$, whereas the theoretical predictions assumed $g_{cf} \gg 1$. Interestingly, there is a much smaller disparity between the measured amplitude and temperature dependence of fluctuations and those predicted by the diffusive theory than was the case for the drag fluctuations in weak magnetic fields. This is due to the fact that our system is far into the ballistic regime ($d/l = 0.02$), whilst it is much closer to the diffusive regime ($d/l_{cf} = 1.1$) in strong fields.

Measurements of the amplitude of Shubnikov-de Haas oscillations in graphene were used to find the concentration dependence of the quantum lifetime τ_q. We found τ_q to increase as $n^{0.5}$ with increasing carrier concentration, both for electrons and holes. In our sample the transport time τ_p was found to also vary as $n^{0.5}$, indicating that screened Coulomb scattering is the dominant scattering mechanism in our monolayer graphene sample. The transport time was found to be roughly seven times larger than the quantum lifetime for all concentrations, suggesting that the disorder in graphene does have some long-range component. The concentration dependence of τ_q was measured at several temperatures in the range $T = 0.05$ – 5.5 K, and τ_q was seen to be temperature independent.

Fluctuations of the resistance were measured in quantising magnetic fields in a monolayer graphene flake. The behaviour of the fluctuations as a function of temperature were analysed using existing theories that have been successfully applied

to conventional 2D systems. The fluctuations were well described by UCF theories applied to graphene in the central region of Landau levels where transport is dominated by extended states. The variance decreased with increasing temperature as $T^{-1.3}$, in good agreement with the expected $T^{-1.5}$ dependence. Some discrepancy was found at low temperatures, where the variance had a weaker, $T^{-0.4}$ dependence, which we were unable to account for. There was also some discrepancy in the temperature dependence of the correlation field, which decreased with temperature as $T^{-0.4}$, which is weaker than the expected T^{-1} dependence.

The fluctuations in the LL flanks were mainly periodic, suggesting a resonant tunnelling mechanism between extended edge states via localised edge states in the sample bulk that arise due to disorder induced fluctuations in the LLs. Interestingly, the fluctuation amplitude in the LL flanks increased with increasing temperature, suggesting that the scattering between edge states may be via hopping transport between localised edge states in the bulk, rather than resonant tunnelling via a single localised edge state. Resistance fluctuations in the LL flanks were measured by varying either the Fermi energy or magnetic field. Comparison of the periods in energy and B-field allowed estimates for the length scale of disorder in the graphene to be made: $r \sim 20$ nm, which is in good agreement with estimates made by other groups using different techniques.

Several suggestions for extending the research performed in this area:

- Coulomb drag fluctuations can be measured between 1D wires. This situation has been studied theoretically, and it is anticipated that similar to the case of drag between 2DEGs, the drag fluctuations can exceed the average drag, resulting in sign change of the drag resistance. Furthermore, predictions are made for different degrees of correlation between the disorder potential in each wire. The distribution of fluctuations is expected to be symmetric for the case of uncorrelated disorder, whilst it is expected to be heavily skewed when the disorder is highly correlated. Such correlations in the disorder could be achieved by intentional doping of the barrier separating the wires.

- The measurement of the drag fluctuations between composite fermions can be performed at other fractional filling factors. Fluctuations of the Coulomb drag could also be measured in the integer quantum Hall regime, similar to

the studied fluctuations of the resistance in Chapter 4.

- The amplitude of fluctuations of the Coulomb drag fluctuations at $\nu = 1/2$ is expected to be dependent upon the conductance of each layer (Section 3.3). It would be interesting to test this conductance dependence.

- The samples used in this project have been limited to the ballistic regime of drag, both in weak and strong B-fields. It would be interesting to extend measurements of the Coulomb drag fluctuations to low-density samples where the drag is in the diffusive regime where existing theories (Sections 2.3 and 4) have yet to be tested. Also, at low densities, interesting features in the Coulomb drag have been predicted [20] which can be examined.

- Measurements of τ_q could be performed in graphene samples produced under a variety of different substrates and fabrication conditions, in order to investigate the effect of these procedures on the dominant scattering mechanisms in graphene.

- The measurements of the resistance fluctuations in high B-fields in a monolayer graphene flake should be repeated in bilayer samples, as the latter can have different properties of electron interference.

- High B-field fluctuations could be measured in other resistance peaks in graphene corresponding to different filling factors. Of particular interest would be the LL at the Dirac point in graphene, as this LL does not exist in conventional 2D samples.

- Lastly, it would be interesting to measure the Coulomb drag between parallel graphene sheets, as well as the mesoscopic fluctuations of the drag.

Bibliography

[1] P. T. Coleridge, *Phys. Rev. B* **44**, 3793 (1991).

[2] A. Isihara, L. Smrcka, *Journal of Physics C: Solid State Physics* **19**, 6777 (1986).

[3] P. T. Coleridge, R. Stoner, R. Fletcher, *Phys. Rev. B* **39**, 1120 (1989).

[4] K. v. Klitzing, G. Dorda, M. Pepper, *Phys. Rev. Lett.* **45**, 494 (1980).

[5] K. von Klitzing, *Physica Scripta* **T1**, 16 (1982).

[6] E. Abrahams, S. V. Kravchenko, M. P. Sarachik, *Rev. Mod. Phys.* **73**, 251 (2001).

[7] C. W. J. Beenakker, H. van Houten, *Solid State Physics*, H. Ehrenreich, D. Turnbull, eds. (Academic Press Limited, 1991).

[8] A. Yacoby, U. Sivan, C. P. Umbach, J. M. Hong, *Phys. Rev. Lett.* **66**, 1938 (1991).

[9] M. J. Laubitz, *Phys. Rev. B* **2**, 2252 (1970).

[10] M. B. Pogrebinskii, *Sov. Phys. Semicond.* **11**, 372 (1977).

[11] P. J. Price, *Physica* **117B**, 750 (1983).

[12] A.-P. Jauho, H. Smith, *Phys. Rev. B* **47**, 4420 (1993).

[13] P. M. Solomon, P. J. Price, D. J. Frank, D. C. La Tulipe, *Phys. Rev. Lett.* **63**, 2508 (1989).

[14] T. J. Gramila, J. P. Eisenstein, A. H. MacDonald, L. N. Pfeiffer, K. W. West, *Phys. Rev. Lett.* **66**, 1216 (1991).

[15] U. Sivan, P. M. Solomon, H. Shtrikman, *Phys. Rev. Lett.* **68**, 1196 (1992).

[16] T. J. Gramila, J. P. Eisenstein, A. H. MacDonald, L. N. Pfeiffer, K. W. West, *Phys. Rev. B* **47**, 12957 (1993).

[17] M. C. Bønsager, K. Flensberg, B. Yu-Kuang Hu, A. H. MacDonald, *Phys. Rev. B* **57**, 7085 (1998).

[18] H. C. Tso, P. Vasilopoulos, F. M. Peeters, *Phys. Rev. Lett.* **68**, 2516 (1992).

[19] H. Rubel, *et al.*, *Surface Science* **361**, 134 (1996).

[20] V. M. Apalkov, M. E. Raikh, *Phys. Rev. B* **71**, 245109 (2005).

[21] K. Flensberg, B. Y.-K. Hu, A.-P. Jauho, J. M. Kinaret, *Phys. Rev. B* **52**, 14761 (1995).

[22] N. P. R. Hill, *et al.*, *Phys. Rev. Lett.* **78**, 2204 (1997).

[23] L. Zheng, A. H. MacDonald, *Phys. Rev. B* **48**, 8203 (1993).

[24] E. Shimshoni, *Phys. Rev. B* **56**, 13301 (1997).

[25] M. Kellogg, J. P. Eisenstein, L. N. Pfeiffer, K. W. West, *Solid State Communications* **123**, 515 (2002).

[26] R. Pillarisetty *et al.*, *Phys. Rev. B* **71**, 115307 (2005).

[27] G. D. Allison, Compressibility study of single- and double-layer two-dimensional systems, Ph.D. thesis, University of Exeter (2004).

[28] E. H. Linfield, G. A. C. Jones, D. A. Ritchie, A. R. Hamilton, N. Iredale, *Semiconductor Science and Technology* **8**, 415 (1993).

[29] J. P. Eisenstein, G. S. Boebinger, L. N. Pfeiffer, K. W. West, S. He, *Phys. Rev. Lett.* **68**, 1383 (1992).

[30] R. Pillarisetty, *et al.*, *Phys. Rev. Lett.* **89**, 016805 (2002).

[31] B. N. Narozhny, G. Zala, I. L. Aleiner, *Phys. Rev. B* **65**, 180202 (2002).

[32] P. A. Lee, A. D. Stone, H. Fukuyama, *Phys. Rev. B* **35**, 1039 (1987).

[33] S. Washburn, R. A. Webb, *Advances in Physics* **35**, 375 (1986).

[34] B. L. Al'tshuler, *JETP Lett.* **41**, 648 (1985).

[35] P. A. Lee, A. D. Stone, *Phys. Rev. Lett.* **55**, 1622 (1985).

[36] B. N. Narozhny, I. L. Aleiner, *Phys. Rev. Lett.* **84**, 5383 (2000).

[37] A. S. Price, A. S. Savchenko, B. N. Narozhny, G. Allison, D. A. Ritchie, *Science* **316**, 99 (2007).

[38] I. V. Lerner, *Phys. Lett. A* **133**, 253 (1988).

[39] A. Kamenev, Y. Oreg, *Phys. Rev. B* **52**, 7516 (1995).

[40] S. Xiong, A. D. Stone, *Phys. Rev. Lett.* **68**, 3757 (1992).

[41] N. A. Mortensen, K. Flensberg, A.-P. Jauho, *Phys. Rev. B* **65**, 085317 (2002).

[42] N. A. Mortensen, K. Flensberg, A.-P. Jauho, *Phys. Rev. B* **65**, 085317 (2002).

[43] B. N. Narozhny, I. L. Aleiner, A. Stern, *Phys. Rev. Lett.* **86**, 3610 (2001).

[44] D. C. Tsui, H. L. Stormer, A. C. Gossard, *Phys. Rev. Lett.* **48**, 1559 (1982).

[45] R. Willett, *et al.*, *Phys. Rev. Lett.* **59**, 1776 (1987).

[46] J. K. Jain, *Phys. Rev. Lett.* **63**, 199 (1989).

[47] H. L. Stormer, D. C. Tsui, A. C. Gossard, *Rev. Mod. Phys.* **71**, S298 (1999).

[48] J. K. Jain, *Physics Today* **53**, 39 (2000).

[49] D. R. Leadley, R. J. Nicholas, C. T. Foxon, J. J. Harris, *Phys. Rev. Lett.* **72**, 1906 (1994).

[50] B. I. Halperin, P. A. Lee, N. Read, *Phys. Rev. B* **47**, 7312 (1993).

[51] I. Ussishkin, A. Stern, *Phys. Rev. B* **56**, 4013 (1997).

[52] V. I. Fal'ko, *Phys. Rev. B* **50**, 17406 (1994).

[53] J. A. Simmons, *et al.*, *Phys. Rev. B* **44**, 12933 (1991).

[54] G. M. Gusev, *et al.*, *Solid State Communications* **97**, 83 (1996).

[55] Z. D. Kvon, E. B. Olshanetsky, G. M. Gusev, J. C. Portal, D. K. Maude, *Phys. Rev. B* **56**, 12112 (1997).

[56] M. C. Bønsager, K. Flensberg, B. Y.-K. Hu, A.-P. Jauho, *Phys. Rev. Lett.* **77**, 1366 (1996).

[57] H. Rubel, A. Fischer, W. Dietsche, K. von Klitzing, K. Eberl, *Phys. Rev. Lett.* **78**, 1763 (1997).

[58] Y. B. Kim, A. J. Millis, *preprint cond-mat/9611125v1* (1996).

[59] S. Sakhi, *Phys. Rev. B* **56**, 4098 (1997).

[60] I. Ussishkin, A. Stern, *Phys. Rev. Lett.* **81**, 3932 (1998).

[61] M. P. Lilly, J. P. Eisenstein, L. N. Pfeiffer, K. W. West, *Phys. Rev. Lett.* **80**, 1714 (1998).

[62] W. Kang, *et al.*, *Phys. Rev. Lett.* **75**, 4106 (1995).

[63] K. S. Novoselov, *et al.*, *Science* **306**, 666 (2004).

[64] A. H. C. Neto, F. Guinea, N. M. R. Peres, K. S. Novoselov, A. K. Geim, The electronic properties of graphene (2007).

[65] P. R. Wallace, *Phys. Rev.* **71**, 622 (1947).

[66] Y. Zhang, Y.-W. Tan, H. L. Stormer, P. Kim, *Nature* **438**, 201 (2005).

[67] V. M. Galitski, S. Adam, S. D. Sarma, *Phys. Rev. B* **76**, 245405 (2007).

[68] K. S. Novoselov, *et al.*, *Nature* **438**, 197 (2005).

[69] V. P. Gusynin, S. G. Sharapov, *Phys. Rev. Lett.* **95**, 146801 (2005).

[70] N. M. R. Peres, F. Guinea, A. H. C. Neto, *Phys. Rev. B* **73**, 125411 (2006).

[71] V. P. Gusynin, S. G. Sharapov, *Phys. Rev. B* **71**, 125124 (2005).

[72] M. I. Katsnelson, *Materials Today* **10**, 20 (2007).

[73] T. Ando, Y. Uemura, *J. Phys. Soc. Jpn.* **36**, 959 (1974).

[74] G. Timp, *et al.*, *Phys. Rev. Lett.* **59**, 732 (1987).

[75] A. K. Geim, *et al.*, *Phys. Rev. Lett.* **69**, 1248 (1992).

[76] J. P. Bird, *et al.*, *Phys. Rev. B* **52**, 1793 (1995).

[77] D. L. Maslov, D. Loss, *Phys. Rev. Lett.* **71**, 4222 (1993).

[78] D. E. Khmelnitskii, M. Yosefin, *Surface Science* **305**, 507 (1994).

[79] A. Morgan, *et al.*, *Phys. Rev. B* **50**, 12187 (1994).

[80] J. K. Jain, S. A. Kivelson, *Phys. Rev. Lett.* **60**, 1542 (1988).

[81] S. V. Morozov, *et al.*, *Phys. Rev. Lett.* **100**, 016602 (2008).

[82] K. Nomura, A. H. MacDonald, *Phys. Rev. Lett.* **98**, 076602 (2007).

[83] A. Gold, *Phys. Rev. B* **35**, 723 (1987).

[84] A. Gold, *Phys. Rev. B* **38**, 10798 (1988).

[85] T. Ando, A. B. Fowler, F. Stern, *Rev. Mod. Phys.* **54**, 437 (1982).

[86] N. H. Shon, T. Ando, *J. Phys. Soc. Jpn.* **67**, 2421 (1998).

[87] Y. Zhang, *et al.*, *Phys. Rev. Lett.* **96**, 136806 (2006).

[88] A. K. Savchenko, *et al.*, *Phys. Rev. B* **52**, R17021 (1995).

[89] E. I. Laiko, A. O. Orlov, A. K. Savchenko, *JETP* **66**, 1258 (1987).

[90] F. V. Tikhonenko, D. W. Horsell, R. V. Gorbachev, A. K. Savchenko, *Phys. Rev. Lett.* **100**, 056802 (2008).

[91] K. Kechedzhi, *et al.*, *preprint arXiv:0808.3211v1* (2008).

[92] J. Martin, *et al.*, *Nature Physics* **4**, 144 (2008).

Appendix A

Appendix

A.1 Joule Heating - temperature of active and passive layers

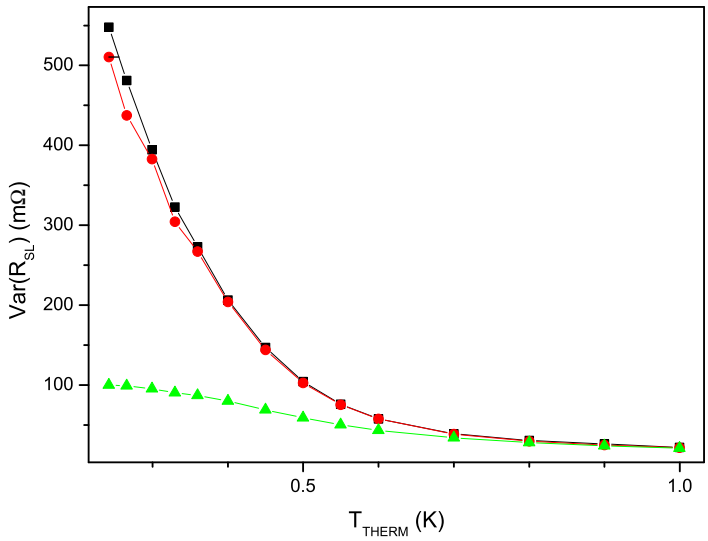

Figure A.1: Variance of the SdH oscillations as a function of the temperature of the fridge thermometer for three different currents: $I = 1$ nA (black), 10 nA (red), and 100 nA (green); $T = 240$ mK, $n_{1,2} = 6 \times 10^{10}\,\mathrm{cm}^{-2}$.

Although there is a large enhancement of the amplitude of fluctuations of the Coulomb drag resistance relative to that expected theoretically, the absolute size of the resistance fluctuations is still very small – typically a few tens of mΩ. Rigorous precautions are taken to minimise the noise in our measurement circuit, as described

in §1.6.3, such that we are able to measure voltage signals as small as 0.5 nV, with a signal-to-noise ratio of about 5. However, in order to measure the drag voltage signal resulting from fluctuations in the drag resistance of $R_D \sim 10$ mΩ, it is necessary to use a current of $I \approx 100$ nA. The resistance of the active layer is 500 Ω in our measurements of the drag resistance fluctuations in weak magnetic fields, and so the power dissipated in the sample is $P = I^2R = 5$ pW, which can cause overheating of the 2DEG at low temperatures ($T \sim 0.1$ K).

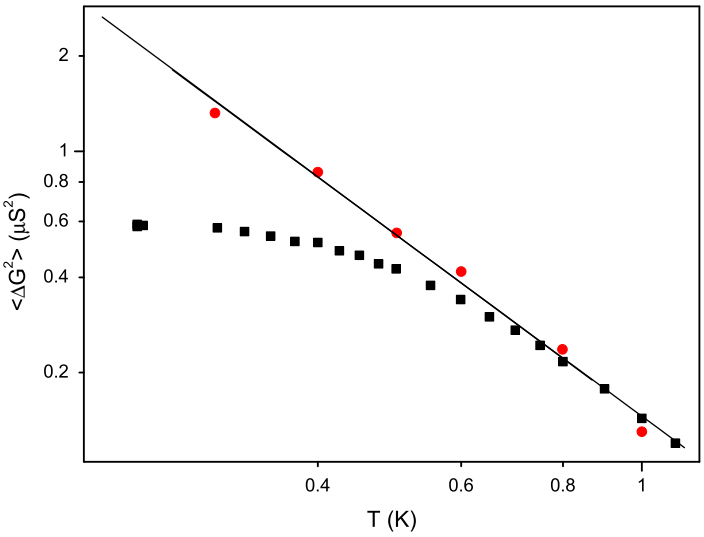

Figure A.2: The variance single-layer conductance as a function of temperature for two different currents: $I = 100$ nA (black) and 10 nA (red); $n_{1,2} = 6 \times 10^{10}\,\mathrm{cm}^{-2}$.

In order to test for the presence of overheating of the active layer and passive layers, three different methods were used: measurement of the temperature dependence of the SdH oscillations, measurement of the temperature dependence of the UCF, and measurement of the drag fluctuations for different currents.

When measuring the temperature of the 2DEG using the SdH oscillations, the resistance is measured as a function of magnetic field over a range of B that incorporates several SdH oscillation periods. The measured resistance has an average background resistance subtracted such that the oscillating part of the resistance is isolated. The size of oscillations are then quantified by calculating the variance of the oscillations. This measurement is repeated at a fixed temperature for three different currents: $I = 1$ nA, 10 nA, and 100 nA. This procedure is then repeated

for several different temperatures and the variance is then plotted as a function of temperature, as shown in Fig. A.1. The variance is essentially the same for all temperatures when measurements are made using 1 and 10 nA, indicating that no overheating of the 2DEG occurs for 10 nA. When 100 nA is used the oscillations are strongly damped, as can be seen from the temperature dependence of the variance for 100 nA in Fig. A.1. The 2DEG temperature can be found as a function of the thermometer temperature for a measurement current of 100 nA by comparing the 100 nA curve in Fig. A.1 with the 10 nA curve.

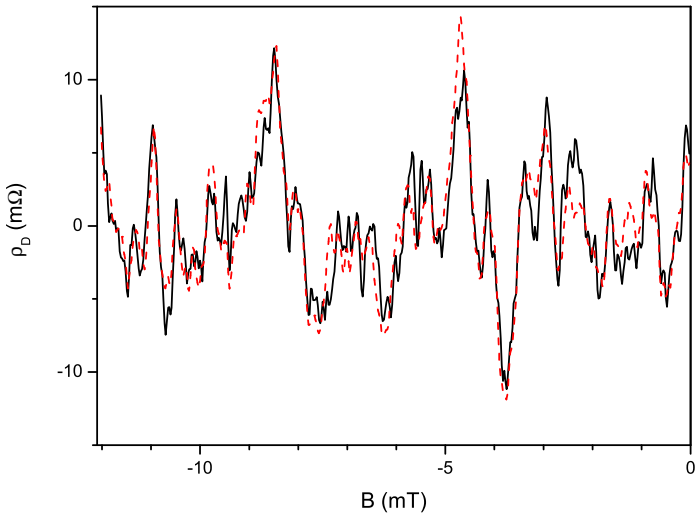

Figure A.3: Drag resistivity fluctuations (after an average background drag resistivity has been subtracted) as a function of magnetic field measured using two different currents: $I = 300$ nA (black) and 700 nA (red); $T = 240$ mK, $n_{1,2} = 6.8 \times 10^{10}$ cm^{-2}.

Figure A.2 shows the variance of the single-layer UCF plotted as a function of temperature for two different currents: $I = 10$ nA and 100 nA. The SdH measurements proved that there was no heating when the current is 10 nA, and that is also seen in Fig. A.2 from the constant power-law dependence of the variance. The 100 nA measurements demonstrate some deviation from this power-law dependence below $T = 800mK$, indicating that below this temperature the 2DEG is overheated. The resistance of the active layer is 500 Ω in these measurements, such that the power dissipated in the active-layer is $P = 5$ pW.

It is clear from the SdH and UCF measurements in the single-layer that heating is present when using a current of 100 nA. However, despite this fact the drag

resistance fluctuations are seen to show no non-linearity even when changing the current from 300 nA to 700 nA, as shown in Fig. A.3. The resistance of the active layer is 200 Ω in Fig. A.3, such that for a 300 nA current the power dissipated is 45 pW, which is sufficient to cause significant heating of the 2DEG. The absence of nonlinearity in the drag resistance is surprising given the fact that the active-layer is being overheated. Overheating of the active-layer can be expected to have less effect on the drag measurement than on the single-layer measurement, as the drag is determined by the temperature of both the active and passive layers, and the passive layer is not heated due to the absence of current flow in the passive layer. It is also interesting to note that this linearity of the drag in a weak magnetic field is in strong contrast to the observed nonlinearity of the drag resistance fluctuations in strong magnetic fields (Section 3.5).